Multiscale numerical investigation on step dynamics during solution growth of 4H-SiC

NAGOYA
UNIVERSITY

Xinbo Liu

Supervisor: Prof. Toru Ujihara

Department of Materials Process Engineering
Nagoya University

This dissertation is submitted for the degree of
Doctor of Engineering

Graduate School of Engineering January 2022

At the entrance to science, as at the entrance to hell,
the demand must be made:
"Qui si convien lasciare ogni sospetto
Ogni viltà convien che qui sia morta"

Karl Marx

Declaration

I hereby declare that except where specific reference is made to the work of others, the contents of this dissertation are original and have not been submitted in whole or in part for consideration for any other degree or qualification in this, or any other university. This dissertation is my own work and contains nothing which is the outcome of work done in collaboration with others, except as specified in the text and Acknowledgements. This dissertation contains 25,446 words including appendices, bibliography, footnotes, tables and equations and has 43 figures.

Xinbo Liu
January 2022

Acknowledgements

Throughout the writing of this thesis, I have received a great deal of support and assistance.

Firstly, I would like to express my deepest appreciation for professor Toru Ujihara, my Ph.D. supervisor, whose expertise was invaluable in formulating the research questions and methodology. Your enthusiasm for research and insightful feedback pushed me to sharpen my thinking and brought my work to a higher level. The completion of my thesis would not have been possible without your encouragement and patience.

I would also like to extend my deepest gratitude to associate professor Shunta Harada. Your rigorous guidance and honest critique were instrumental for me in reflecting on my findings.

I am extremely grateful to professor Toshiyoki Koyama, Hajime Kimizuka, Masahide Sato, and Kazuya Takeda for being on my review committee, providing valuable advice to this study.

I would like to acknowledge my colleagues for their outstanding collaboration. I would particularly like to single out the specially appointed assistant professor Can Zhu for your in-depth discussion on the philosophy and skills of crystal growth and the excellent assistance in experiments. You also played a decisive role in my research topic determination. Particularly helpful to me during this time was Ph.D. candidate Yifan Dang. Your valuable discussions on numerical simulation application in crystal growth investigations can not be overestimated.

Many thanks to professor Elias Vlieg, Herma Cuppen, Dr. W.J.P van Enckevort, and Dr. Hugo Meekes for accepting me as a visiting scholar to Nijmegen University. The daily discussions with you significantly enriched my understanding of crystal growth and gave me indispensable guidance in constructing the kinetic Monte Carlo model.

I would like to thank the Graduate Program for Real-World Data Circulation Leaders for nurturing and financial support. I gratefully acknowledge professor Koichi Takeda, Yoshiharu Ishikawa, and Yasuhisa Hasegawa for reviewing and providing valuable advice to chapter 5 of this thesis. Special thanks to associate professor Naoki Nishida for helping me to coordinate the degree acquisition with the completion of the program.

I also had great pleasure of working with my colleagues, Dr. Fumihiro Fujie, Ph.D. candidate Hayato Sumi, and Goki Hatasa. You never wavered in your support during my doctor course.

Abstract

4H-SiC (silicon carbide) is a promising material for next-generation power devices due to its excellent physical properties. The top-seeded solution growth (TSSG) method is suitable for obtaining high-quality, large SiC bulk crystals. By applying the dislocation-conversion phenomenon in the TSSG method, SiC crystal with few dislocations can be obtained. High and steep macrosteps have been proven to be critical for converting dislocations. However, over-developed macrosteps also induce macroscopic defects. Step bunching is an essential process in macrostep formation. A systematic understanding of the mechanisms of step bunching is significant for controlling macrosteps structure. However, such an understanding is difficult to be obtained only through experimental studies due to the complex factors coupling mass transport and surface kinetics varying over different scales and the extreme ambiance required for SiC crystal to grow. Therefore, this thesis intends to utilize a multiscale numerical investigation to discuss factors affecting step bunching during the solution growth of SiC crystal.

First, a growth experiment was carried out on a 2-inch 4H-SiC crystal was grown on the C face of a 1°off-axis seed crystal using the TSSG method. Step-flow growth towards the $[11\bar{2}0]$ direction occurred over the entire growth surface. Inhomogeneity in the surface morphology was observed. The step height increased monotonically along the step-flow direction. The non-uniform step height resulted in the spatial distribution of threading screw dislocation (TSD) conversion. No conversion of TSD took place in the upstream area of step flow due to small step height. In contrast, TSD conversion frequently happened in the center of the crystal and the downstream area, with a conversion ratio as high as 80% in these areas. A macroscale numerical simulation was carried out over the bulk solution to investigate the reason for the step-bunching distribution. An outward solution flow occurs under the growth surface. Therefore, the solution forms an anti-parallel and a parallel flow against the step flow in the upstream and downstream areas. Thereby the opposite affects the step bunching behaviors, respectively. This study revealed a step bunching

phenomenon that occurs only in large-sized crystals' growth and pointed out that the solution flow direction is a critical controlling parameter for uniform growth.

In order to study the development of step bunching in quantity, a numerical model coupling mass transport and step kinetics in the mesoscale was constructed. The macroscale numerical study results were utilized as boundary conditions in the mesoscale model. Surface roughness due to step bunching was studied under different solution flow velocities. The step bunching development with solution flow present is consistent with the experimental results. However, there was disagreement between the simulation and experimental results without solution flow. Since solute's incorporation into steps and transport together determines step bunching progress. Next, numerical investigations around the development of step bunching induced by solvent physical properties representing mass transport and step kinetics were carried out. It is found that step bunching occurs due to the depletion of solute in the region with high step density, caused by a high step kinetic coefficient. On the other hand, by promoting the transport of the solute in the solution, the step speed becomes uniform, thereby the step bunching can be prevented. Furthermore, we proposed a non-dimensional Damköhler number for crystal growth in step-flow mode. It correlates incorporation rates with bulk diffusion rates and can build a phase map of growth rates and step bunching stability. Several solvents are located according to reported experimental results in the phase map, demonstrating the possible usage of the phase map as a pointer for solvent designing.

In order to evaluate a solvent for its tendency towards step bunching, knowledge of both diffusion coefficient and step kinetic coefficient is required. The latter, however, is difficult to be measured through general experiments. The Kinetic Monte Carlo method was applied to conduct a microscale numerical investigation on step kinetics at crystal-solution interfaces. Step kinetic coefficients are calculated from kink density and crystallization rates at step edges of steps on vicinal {0001} facets. The vicinal interfaces contain periodic arrays of bilayer steps. Kinetic coefficients for both <$1\bar{1}00$> and <$11\bar{2}0$> oriented steps are determined under different temperatures, supersaturations, and the presence of impurity species. There are three types of steps on each polarity {0001} face, and the values of step kinetic coefficients are shown to be highly anisotropic. The kinetic coefficient of S_N steps increases exponentially with temperature. In contrast, the values of S_D and S_M steps remain constant until the temperature rises over 2000 K, under which a thermal roughening occurs on the {0001} facets. At low temperatures, the kinetic coefficient of the S_N step is about $3.8 \times 10^5 \mu m/s$, two orders smaller than the steps of S_D and S_M types, which is

5.9×10^7 and $4.6 \times 10^7 \mu\mathrm{m/s}$, respectively. At low supersaturations, the movement of S_N steps is observed through one-dimensional nucleation on the step edges. At the initial stages of step-flow growth, the S_D steps bunch into S_N steps due to the different growth rates, while the poor mobility of S_N steps is considered as a factor that keeps crystal growth away from further step bunching. An aluminum-like impurity species is introduced in the simulation, and its influence on step kinetic coefficient and step bunching was investigated. The Al-like impurity behaves on the two polarity faces differently. On the Si face, incorporation occurs both on terraces and at step edges. The Langmuir-style adsorption on the terrace is considered as an origin of an impurity-induced step bunching. On the C face, step incorporation is realized. The suppression of step mobility due to impurity adsorption on step edges is considered a reason that suppresses step bunching on the C face.

Contents

List of Figures

List of Tables

Chapter 1

Why this thesis?

1.1 Why SiC?

Today, most semiconductor devices and integrated circuits are made of silicon. The superior performance and cost advantages give silicon an absolute advantage in integrated circuits. In the last several decades, Si-based technologies, especially large-scale integrated circuits (LSIs), have become the critical components in almost all electrical and electronic systems, leading to innovations and prosperity in modern society.

Nowadays, the concept of a sustainable society is getting well accepted. Cutting energy consumption is a significant issue for maintaining a sustainable society. In the rapid expansion of electricity demand, improving electricity efficiency, in other words, reducing electricity waste, is becoming more and more significant for the development of our sustainable society.

According to [1], about 26% energy consumption is due to the loss during power delivery and conversion. Electric power is regulated and converted to be supplied to the loads in the best form in power electronics. The devices undertaking such conversion, *e.g.*, AC-DC conversion, voltage, and frequency conversion, are called power devices. To improve electricity efficiency, power devices of high performance are necessary.

Silicon and Si-based power device are now the most mature technologies in power electronics. However, even with the numerous efforts to improve the Si-based device, like structure modification, silicon-based devices have gradually reached their physical limits. Meanwhile, silicon carbide (SiC) is a promising material for next-generation power devices due to its outstanding properties.

Table 1.1 Major physical properties of Si and 4H-SiC[2].

Physical property	Si	4H-SiC
Bandgap, E_g (eV)	1.12	3.26
Breakdown field, E_B ($\times 10^6$ V/cm)	0.3	3
Electron saturated drift velocity, v_s ($\times 10^7$ cm/s)	1	2.7
Thermal conductivity (W/cm·K)	1.5	4.9

Table 1.1 shows the major physical properties of Si and 4H-SiC. The latter one is the most promised polytype of SiC for power devices because it owns higher mobility, higher breakdown voltage, and smaller anisotropy than other polytypes, and the largest bandgap.[2]. Compared with Si, the bandgap of 4H-SiC is 3.26 eV, almost three times Si. The large bandgap indicates lower leakage current due to thermo-activation under high working temperature, promising the high-temperature performance of SiC-devices. The breakdown field of 4H-SiC is ten times Si, indicating a ten times higher breakdown voltage. Thus the thickness of the drift layer in SiC-MOSFET (Metal-Oxide-Semiconductor Field-Effect Transistor) can be reduced to 1/10 of that of Si-MOSFET, leading to reduction of on-resistance and a compact design. Also, the electron saturated drift velocity of SiC is 2.7 times that of Si. That also implies an improvement in conversion efficiency during high-frequency switching. With the high thermal conductivity and the advantage of high-temperature reliability, the cooling system can be simplified with the application of SiC-base power devices, which will significantly benefit its application in the transport field. In summary, by applying SiC, power devices of higher efficiency, lower loss, and more compact size are promised.

In 2018, The Model3 model electric car of Tesla Corporation adopted an inverter with 24 SiC-MOSFETs as power modules. It was the first automobile manufacturer to integrate full SiC power devices in the main inverter[3]. Owing to its demonstration effect, at present, more than 20 automobile manufacturers worldwide have used SiC power devices in onboard charging systems. ROHM supplied Full SiC Power Modules to Formula E racing team Venturi and enhanced performance through a significant reduction in size by 43% and weight by 6kg[4]. According to Yole, the global market space for automotive SiC power devices in 2018 was US$ 420 million and will rise to US$ 1.4 billion by 2023, corresponding to a growth rate of 29%[5].

With the fast growth in demand for SiC, the SiC substrate is in a severe lack in the supplement. Compared with silicon-based devices, SiC-based devices are usually several times more expensive due to the high cost of manufacturing SiC wafers. A 6-inch SiC wafer is over US$ 900/piece, much more expensive than the Si wafer, which is only US$ 50/piece. Another issue for SiC applications is that their defects limit the performance. Both of the two issues are closely related to the growth method of SiC crystal.

1.2 Growth methods of SiC single crystal

Under normal pressure, the eutectic liquid phase(stoichiometric ratio, Si:C = 1:1) does not exist. Therefore, traditional methods like the Czochralski (Cz) method cannot grow SiC crystals. Until now, several methods have been suggested to obtain bulk SiC single crystals. According to the material composition in the ambient phase, one can classify the methods into physical vapor transport (PVT) methods, including the modified PVT (M-PVT) method, high-temperature chemical vapor deposition (HTCVD) method, and liquid phase methods. Among these methods, the PVT method is the only method applied for commercially manufacturing SiC wafers, while the HTCVD method and the liquid phase methods have been extensively studied in recent years for industrial application. On the other hand, the chemical vapor deposition (CVD) method and some liquid phase epitaxy (LPE) techniques are widely used in the epitaxial growth of SiC thin films.

1.2.1 PVT method

PVT method is a traditional but standard method for producing bulk SiC crystals. This method is also known as the modified Lely method or the seeded sublimation recrystallization method. Figure1.1 shows the diagrammatic illustration of the PVT method. Under an extremely high temperature (> 2500°C), SiC powder settled at the bottom of the crucible sublimates and decomposites into vapor molecules such as Si, Si_2C and SiC_2. The molecules are transported to the seed crystal at a lower temperature and recrystallized to SiC on the seed crystal. The quality of the obtained crystal is controlled by the temperature distribution and convection in the furnace. Meanwhile, the growth of SiC is susceptible to even a minor change in conditions. Parameters like the C/Si ratio, temperature gradient, growth rate, and gas pressure/convection drastically influence the grown crystal quality, like surface morphology, microscopic defects, and polymorphism.

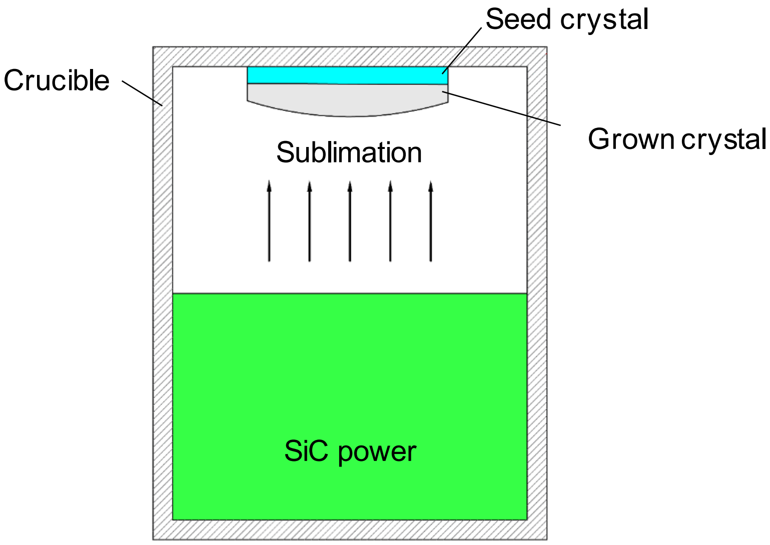

Figure 1.1 Schematic of growing SiC by PVT method.

The PVT method is the only successful method for commercial SiC wafer production. Wafers of 6 inches by PVT method are already available. Nonetheless, it has several disadvantages.

1. Disadvantage in the growth of the p-type crystal. The main commercial SiC product is of n-type and semi-insulated type. One can obtain n-type crystals by introducing nitrogen gas and semi-insulated SiC by removing the nitrogen elements from raw materials. However, making p-type SiC requires doped with the III-group elements, which remains difficult.

2. The defect density of PVT-grown SiC wafer is still at a high level.

3. It is not easy to enlarge wafer size with the PVT method. In the PVT method, the growth of SiC crystal mainly occurs on the {0001} faces, while enlargement of wafer size requires lateral growth on the plasmatic faces such as the $\{11\bar{2}0\}$ and $\{1\bar{1}00\}$ faces. Although Cree, Inc. has realized mass production of 6-inch SiC wafer since 2009, until 2021, the 8-inch wafer is still under development.

1.2.2 HTCVD method

Figure1.2 shows the schematic of growing SiC by HTCVD method. This method is improved based on the chemical vapor deposition (CVD) method. During growth, the source gas, (SiH_2 + C_2H_8 or SiH_4 + C_2H_4), are streamed into the growth chamber

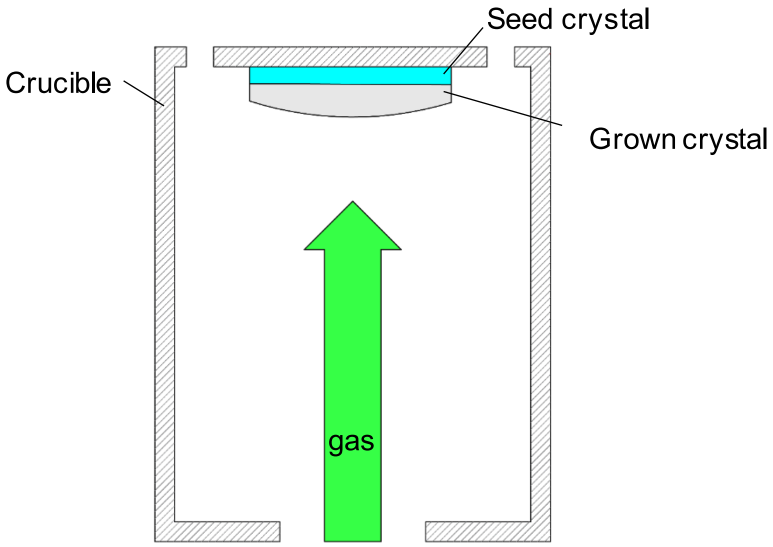

Figure 1.2 Schematic of growing SiC by HTCVD method.

and transported by the carrying gas (usually H_2) to the seed crystal. A chemical reaction happens on the seed crystal, forming SiC crystal, releasing hydrogen gas. The high temperature (1800°C~2300°C) realizes a growth rate of up to 1mm/h, higher than the traditional CVD method, which guarantees its application in bulk crystal growth. Using gas as C and Si sources makes it easy to control some parameters, such as the C/Si ratio and the raw material supply, which is usually a significant factor for suppressing growth instability. On the other hand, the expensive gas source increases the cost of producing SiC wafers from this method.

1.2.3 TSSG method

Liquid phase methods are promising for high-quality crystals because the growth condition of liquid phase methods is near the thermal equilibrium. Nakamura *et al.* reported that micropipes propagated from SiC substrate are healed during liquid phase epitaxy[6]. Since then, the liquid phase method started gathering attention.

Among the liquid phase methods, the top-seeded solution growth (TSSG) method is suitable for long-term growth to obtain large SiC ingots. Figure1.3 shows the schematic of growing SiC from the TSSG method. The equipment is similar to that used in the Cz method. By continually pulling up the seed crystal, one can maintain the crystal/solution interface at a constant state, which is necessary to obtain a uniform crystal property during long-term growth.

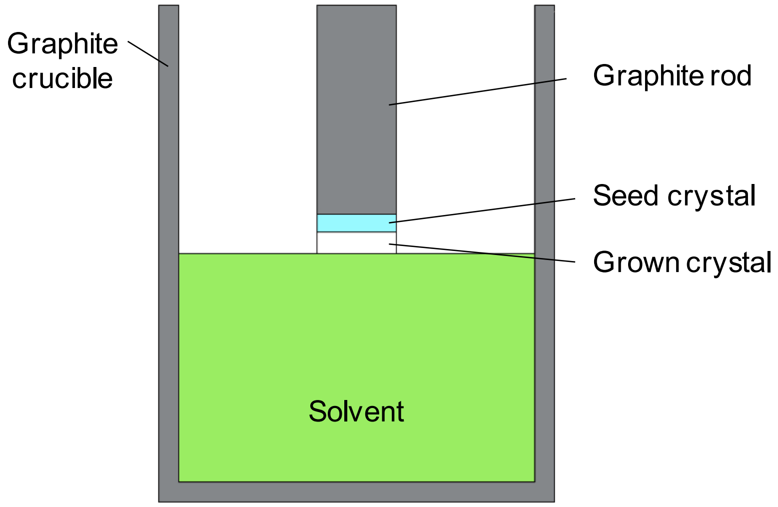

Figure 1.3 Schematic of growing SiC by TSSG method.

Raw materials, usually silicon and metal elements, are first placed at the bottom of a graphite crucible as solvent. During growth, induction coils heat the graphite crucible to a temperature (T_{crucible}) over the melting point of the solvent. The solvent dissolves the crucible wall as a carbon source and transport carbon to the seed crystal by the solution bulk. The carbon concentration in the bulk solution assumed uniform, equals to the carbon solubility at the crucible wall ($C_{T_{\text{crucible}}}$). Since the crucible wall is heated directly while the seed crystal is far away from the heating source, and the seed shaft eliminates heat, the temperature at the seed crystal T_{seed} is lower than at the crucible wall. The carbon solubility at the seed crystal $C_{T_{\text{seed}}}$, proportional to the temperature, is thus lower than that in the bulk solution, forming a supersaturated solution at the seed crystal surface. The supersaturation

$$\Delta C = C_{T_{\text{seed}}} - C_{T_{\text{crucible}}} \tag{1.1}$$

drives carbon to precipitate and deposit on the seed crystal as SiC.

Compared to the PVT method, growing bulk SiC crystals with the TSSG methods show the following advantages.

1. The TSSG method can grow crystals of high quality. Our group revealed ultra-high-quality crystals with an average dislocation density of $\sim 1\text{cm}^2$ and BPD free crystals by the dislocation conversion techniques[7].

2. P-type crystals can be easily realized with aluminum addition. Al is an ideal dopant for high carrier density p-type crystal. In solution growth, adding

Al has been proven helpful for obtaining smooth surface morphology. Thus liquid methods have natural advantages in growing p-type crystals.

3. Enlargement of crystal size can be realized by controlling the seed pulling rate during growth, an analogy to the Czochralski monocrystalline silicon shoulder process.

1.2.4 Issues in TSSG method

Despite the mentioned advantages of the TSSG method, some issues remain. For example, carbon is transported through diffusion and convection, while mass transport is usually much slower than surface kinetics in the liquid phase. Therefore, like all the other transport-limited methods, instability occurs on the growth surface due to insufficient supplement of growth unit. Other problems such as deposition of undesired polytypes, solvent inclusion, and inhomogeneity of dopant distribution are also remaining. On the other hand, although we have been constructing crafts for growing large-size crystals and smooth morphologies over the whole surface have already been realized on 3-inch crystals, technologies for the growth of 6-inch or even larger crystals, which is indispensable in the commercial competition with the PVT method, are still underdeveloped. In this section, some issues that remain to be solved are listed and discussed.

Lowering defects in crystal

Our group has succeeded in lowering the density of threading dislocation, utilizing a dislocation conversion technology, a crystal with a low dislocation density ($\sim 100/\mathrm{cm}^2$) can be obtained stably[7]. Further lowering of dislocation density, especially of the basal plane dislocations (BPDs), and suppressing the generation of macroscopic defects, like solvent inclusion, remain issues.

Polymorphism instability

SiC crystal forms by stacking Si-C bilayers. SiC has over 200 kinds of polytypes with different stacking sequences. The physical properties vary over different polytypes, and the 4H-type is considered the best material for power devices. On the other hand, once two different polytypes are deposited on the substrate simultaneously, grain boundaries between polytype islands become the source of dislocations due to the mismatch of the lattices. Therefore, obtaining the desired polytype and suppressing other polytypes' deposition is significant.

When growth is performed on the {0001} faces, through a two-dimensional (2D) nucleation mechanism, polymorphism stability is significantly related to the growth condition, mainly temperature. During growth on substrates of 4H-SiC, besides the 4H-SiC islands, 6H-SiC islands also commonly appear because the interface energy costs for depositing are very close[8, 9]. Thus in the growth of SiC, polymorphism instability is closely related to the 2D nucleation phenomenon.

In epitaxy, Kimoto *et al.* suggested utilizing the step-flow growth mode to maintain the polytype of the substrates[10]. By manufacturing substrates with an off-angle, elementary bilayer steps are initially supplied. Due to the lower energy, new deposition primarily occurs on the step edges rather than on random positions on the terraces. Therefore the polytypes of the step edges, thus the substrate, are inherited. In bulk growth, the off-angle provided elementary steps only live the beginning stage of growth, while spiral growth centers provide new and sustainable steps during the whole growth period.

However, we found that in the growth with the TSSG method, 2D nucleation thus polymorphism instability can still occur on the terraces between steps even with the step supplement[11, 12]. When the terraces become aboard enough due to step bunching, the accumulated growth units on the terrace cannot diffuse to the step edges. If there is no end of screw dislocation at the terrace surface, the supersaturation of growth units due to accumulation arises over the critical supersaturation, and 2D nucleation occurs. Although it is reported that such 2D nucleations occur on those step-bunching-induced aboard terraces helps relieve the step bunching itself[13, 14], in the case of SiC, an island of another polytype, since it can not merge into the coming steps, can hinder the step advancing and leads to destructive macroscopic defects[15]. In this way, one can conclude that polymorphism instability during the growth of SiC with the TSSG method is a consequence of the instability of step morphology.

Optimization of solvent composition

As explained in the last section, carbon supersaturation drives the growth of SiC; thus, the carbon solubility and its temperature dependence are significant. The phase diagram indicates that the silicon melt can dissolve up to 18% of carbon at 2800 °C[16]. While at a lower temperature, at which one usually performs solution growth, the carbon solubility in pure silicon melt is very low (0.17 at% at 1800°C).

The consequence of low carbon solubility is a low growth rate of < 10 µm/h. Thus the growth utilizing pure silicon solvent is suitable for SiC thin film epitaxy but far from growing bulk crystals. Although solutions such as increasing the extremely high temperature of 2200~2300°C to increase the carbon solubility and enhance carbon supply by enforced convection have been proposed,[17] people preferred the other approach.

Extra elements are added to the solvent to improve carbon solubility. Usually, adding transition metals or rare earth metals to the pure silicon can improve the carbon solubility by several orders of magnitude compared to the pure silicon solvent[18–20]. Among the proposed solvent compositions, the composition $Si_{0.6}Cr_{0.4}$ is widely accepted as a basic solvent for SiC growth due to its high carbon solubility [21–27].

An issue of utilizing the additional elements is incorporating these extra elements into the grown crystal. Since the incorporated atoms probably work as deep energy levels traping carriers, resulting in damage to the device performance such as the conductivity. It is reported that the incorporation of Cr is as low as $10^{17}/cm^3$[21]. For the other elements, there is not enough investigation.

Based on the above viewpoints, a standard solvent-designing approach involves carbon's solubility to the liquid phase and the solid solubility of additional elements to the SiC crystal. In the lack of experimentally acquired phase diagrams, one uses the method of calculation of phase diagrams (CALPHAD) method to obtain the phase diagram instead. Many compositions have been proposed according to the calculated phase diagrams[24, 28].

On the other hand, the growth morphology can be drastically affected by even tiny changes in solvent composition, making it an essential consideration in solvent designing. Since the behavior of steps plays a significant role in growth, extensive works have been carried out on the influence of solvent on step structure to find the best solvent for solution growth[25, 29–33]. A major advance in solvent design is discovering the addition of aluminum suppressing step bunching and thus maintaining a smooth surface[30].

Taking the influence on step morphology is gaining more and more significance in solvent designing. A general and completed understanding of additional elements affecting step behavior is necessary to satisfy this demand.

Craft modification for crystals of large diameter

Growing crystal of small size is relatively simple since the growth condition is uniform overall growth interface. In this case, the most critical parameter might be the maximum temperature difference in the solution, which determines the growth driving force.

However, growing crystals of larger diameters must consider more factors. One of these factors is the temperature distribution over the crystal/solution interface, which gets difficult to maintain uniformity when the crystal diameter is large enough. Daikoku *et al.* showed that the shape of the growth surface could be changed through controlling the temperature distribution in the growth front[34].

Another factor is the solution flow direction under the growth interface. Zhu *et al.* revealed that the flow direction has a major influence on the step bunching behavior in SiC growth[12]. After this study, K. Ariyawong's fine work revealed the solution direction creating different surface patterns by varying effects on step structures in different surface areas[35]. While Daikoku cleverly utilized the concave growth surface and the outward solution flow to create an anti-parallel flow growth mode and obtained crystals of high surface uniformity[34].

As demonstrated in Chapter 2, growth utilizing off-axis substrates is dangerous to keep a constant flow pattern during the whole growth period because of the opposite effects on steps in different areas by flow direction. Furthermore, we found that the flow direction finally became the central issue in large diameter crystal growth.

1.3 Defects in SiC and macrostep

SiC crystal contains defects in different length scales. The microscopic defects include dislocations and stacking faults. They involve the disorder of atomistic lines and faces. Usually, the density of these microscopic defects is an essential criterion in judging the crystal quality because the performance of devices can be significantly lowered for containing these defects [36]. SiC crystals can also contain macroscopic defects of a size that could be directly observed by optical microscopy, like stretches due to mechanical damage during substrate polishing. There could also be solvent inclusion for crystal growth with the solution method. Those macroscopic defects themselves usually cause significant damage to the electrical properties and

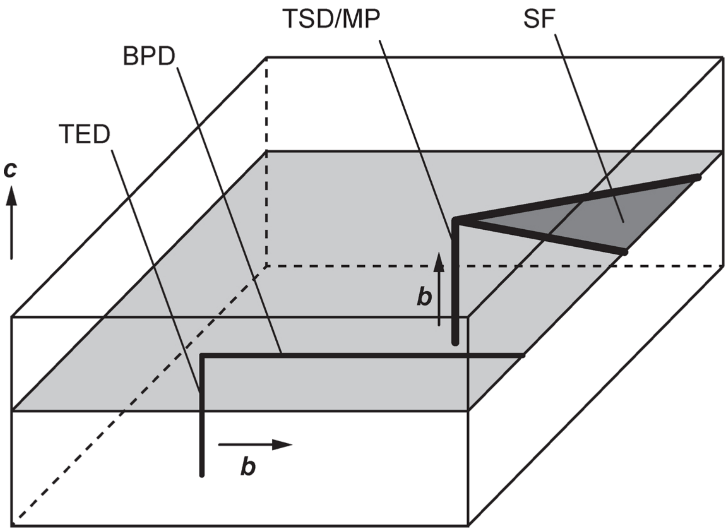

Figure 1.4 Type and propagation direction of defects in SiC crystal.

mechanical properties. Also, the defects initially existing in substrates can become sources of dislocations, spreading harmful effects to epitaxial layers.

1.3.1 Microscopic defects and dislocation conversion

Figure1.4 shows the primary microscopic defects in SiC crystals and their propagation directions. These microscopic defects are classified according to both the Burgers vector $\boldsymbol{b}$ directions and the directions in which they propagate. The threading edge dislocation (TED), threading screw dislocation (TSD), and micropipe (MP) propagate along the c-axis. MP is a hollow pipe of micrometer size with $\boldsymbol{b} > 3\boldsymbol{c}$. While the stacking fault (SF) and basal plane dislocation (BPD) propagate inside the {0001} planes.

Since the growth of SiC crystals is usually performed along the c-axis, the threading dislocations propagate together with the growth processing and will never be eliminated. Fortunately, it has been revealed that microscopic defects of the same $\boldsymbol{b}$ can convert into each other during growth. That indicates TSDs can convert into SFs of frank type, while TEDs can convert into BPDs of the same $\boldsymbol{b}$. Especially, Yamamoto *et al.* uncovered that macrosteps swiping the surface help convert threading dislocations into defects on the basal planes[37]. Figure 1.5(a, b) shows the schematics of the conversion process of threading dislocations during growth. Since the defects on the basal planes will not propagate into the further grown layer, this phenomenon is utilized to reduce the dislocation density[38, 39]. Once all threading dislocations are

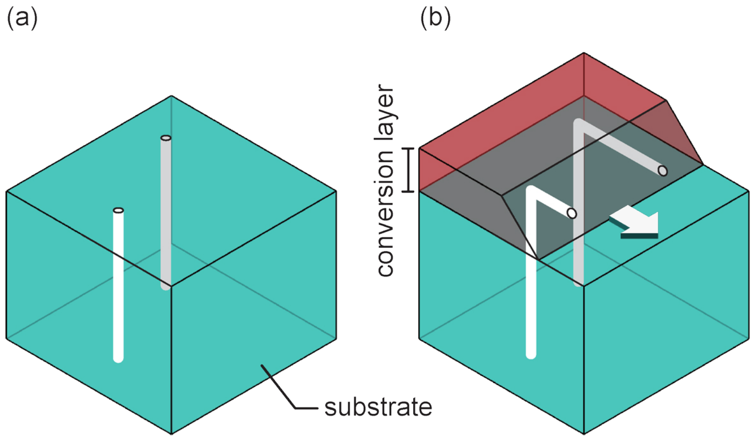

Figure 1.5 Processes of obtaining dislocation-free crystal. (a) A substrate with TDs, (b) TDs are converted with promotion of a macrostep, and (c) the formation of a TD-free layer. The vertical grey lines inside crystals indicate TDs while the lines propagating along the step-advancing direction indicate converted dislocations in basal planes. The array indicates the step-advancing direction.

converted, the further grown layer will be dislocation-free, as shown in figure 1.5(c). This phenomenon has been utilized to realize ultra-high-quality SiC crystals[7].

Conversion of TSDs occurs more difficult than conversion of TEDs and is closely related to the step structure. Around TSDs, growth hillocks form due to the spiral growth mechanism; to conduct the conversion, a step swiping across a TSD must be higher than the hillock around the TSD. On the other hand, Ha *et al.* revealed that the conversion is due to the image force from the step edge; thus, Xiao *et al.* revealed that the slope of a macrostep also affects the conversion behavior[40, 41]. In summary, to eliminate threading dislocations and obtain high-quality SiC crystals, high and steep macrosteps are necessary, at least in the initial stage.

1.3.2 Macroscopic defects induced by macrosteps

Besides the microscopic defects, macroscopic defects are also introduced during growth or wafer manufacturing. The mechanical damage during manufacturing wafers is out of the scope of this thesis. As a transport-limited growth, issues found in the growth of other crystals with solution methods may also happen in the solution growth of SiC. For example, we have observed the instability of the surface and the following issues like growth striation and solvent inclusion.

An essential problem happening during growth is the formation of macrosteps. Figure 1.6 shows a schematic of (a) equally spaced elementary steps and (b) a

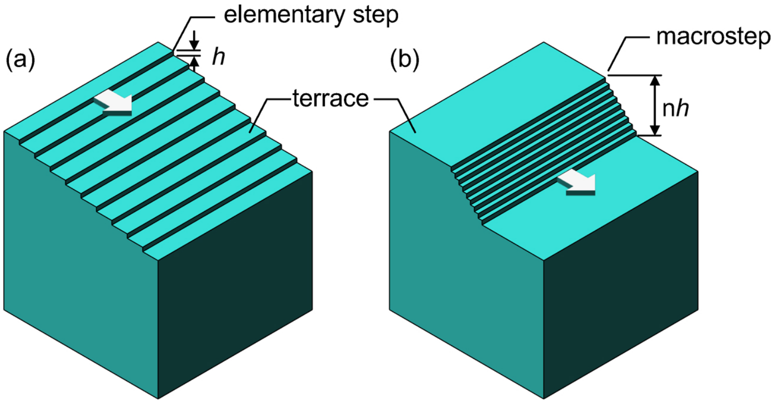

Figure 1.6 A step train (a) equally spaced and (b) bunched to form a macrostep. The white arrays show the advancing directions of steps.

macrostep consisting of a bunch of elementary steps. The details of the step bunching mechanism will be introduced in section 1.4.3. This section intends to introduce the influence of step bunching on crystal quality. Although we revealed that macrosteps of a considerable height and a steep slope are necessary for the conversion phenomenon, which helps to lower dislocation density and increase crystal quality, an over-developed macrostep, on the contrary, is a cause for many macroscopic defects.

Nishinaga and Bauser respectively revealed that growth striation forms with macrosteps during growth with impurity doping. In a grown crystal, moving traces of macrosteps usually can be observed in a different color or transparency, in a cross-section view. That is due to a variation in the impurity-incorporation rate among steps and terraces, leading to the doping concentration in the macrosteps traces being different[42–44]. Such growth striations imply inhomogeneity in the distribution of impurities, which negatively influences the crystal's electrical properties.

Moreover, macrosteps can also result in formation inclusions. Inclusions are heterogeneous substances found contained within the grown crystals. The heterogeneous substance can be solidified solvent and crystalline or non-crystalline particles. In a SiC crystal, inclusions can also be SiC particles of a different polytype. Figure 1.7 shows three types of solvent inclusion caused by macrostep. Figure (a) shows the inclusion involved in a trench-like structure. When a macrostep is present, there must be wide terraces in front and behind it (as shown in figure 1.6 (b)). As we mentioned in section 1.2.4, 2D nucleation takes place on those terraces. Once a growth island forms on the front terrace due to 2D nucleation, it blocks the macrostep from advancing, and grain boundaries form between the growth island and macrostep. In some cases, it generates a trench-like defect between the growth island and the

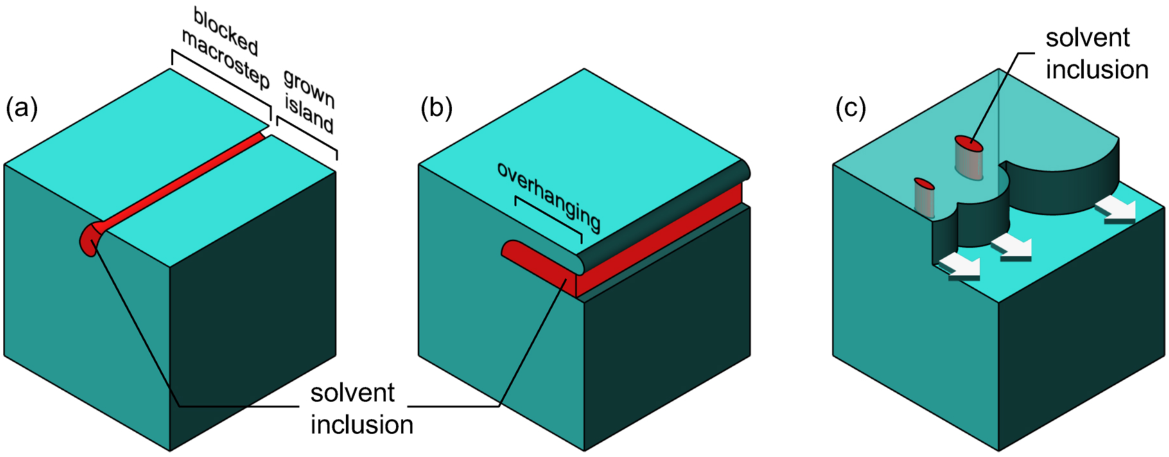

Figure 1.7 Schematics of solvent inclusion in (a) a trench-like structure, (b) a overhanging structure and (c) a cellular structure.

macrostep[12]. Once the trench gets deep enough, convection becomes too weak to transport growth units into the trench so that the trench will no longer be filled up with crystal growth. As shown in figure 1.7, together with the growth, the trench extends extensively and results in solvent inclusion of a large area, damaging the whole crystal[45]. Even without growth island blocking, the elementary steps stacked at the bottom of the macrostep can fall into a dead zone and stop moving, while in most cases, the top elementary steps keep moving, leading to an overhanging layer. That leads in another typical type of inclusion formation, as indicated in figure 1.7 (b). [46]. Figure 1.7 (c) shows inclusions involved in a cellular structure formed on a macrostep. The step edge of an over-developed macrostep may lose its stability and bend into a cellular structure. In the valleys, for some reason, *e.g.*, an insufficient supply of growth unit, the growth stops. The fingers between valleys keep growing, and once two fingers grow to closure, the solvent in the valleys between the two fingers is trapped to be inclusion[46].

In summary, macrosteps are found necessary in the beginning stage for dislocation conversion, while they must be eliminated during the later bulk growth to avoid inducing other defects. That indicates crafts to enhance macrosteps and to dissipate them are both necessary. Understanding the factors influencing step structure and the dynamics of step bunching is urgent.

1.4 Step bunching mechanisms

The last section revealed the significance of controlling the height and the slope of macrosteps. Step bunching is an essential process in the formation of macrosteps, which is also indicated as a hill-and-valley structure [47] or a nano facet [48]. Knowledge about step bunching is significant for controlling the macrostep structure. This section intends to make a review of the mechanisms of step bunching.

1.4.1 Step bunching at the beginning stage of SiC growth

Kimoto *et al.* discovered that during CVD epitaxy of 4H- and 6H-SiC on <$1\bar{1}00$> oriented off-axis substrates, an unusual behavior that those <$1\bar{1}00$> directed steps bunch into half-unit-cell height and then into full-unit-cell height[47]. Take the 6H-SiC as an instance. Due to the different energy gains for depositing on different terraces[49], the deposition rate on each terrace, thus the growth rate of each step, varies in a three-fold period. That is why step bunching of half-unit-cell height forms. On the surface, there are two types of half-unit-cell bunches terminating with different configurations, alternating their sequences. For the two types of terminating configuration, one wants to refer to the cross-sections in figure 4.1. The bunches with two unsaturated dangling bonds grow faster than those with only one dangling bond, finally leading to the full-unit-cell bunching. However, there remain some puzzles in this explanation. The ratio On grown crystals, Kimoto showed the ratio of full-unit-cell bunchings is 66% on 4H-SiC while is only 7% on 6H-SiC, while the reason for this distinction remains unexplained. Later Borovikov reproduced this phenomenon with a computer simulation[50]. There are as well other studies that take this mechanism to explain the same step bunching behavior in SiC etching with H_2 and the shape of spiral growth hillock[48, 51].

Although this mechanism involves only steps oriented in the <$1\bar{1}00$> direction, the steps in the <$11\bar{2}0$> directions break into alternating segments of <$1\bar{1}00$> steps due to energetic reasons. Therefore, a perfectly <$11\bar{2}0$> oriented step train bunches into half-unit-cells but is supposed not to have further bunching[52].

This is a special step bunching mechanism shown in crystal with an alternating stacking order, *e.g.*, hexagonal polytypes of SiC, GaN[53, 54], ice[55]. It is also found in some layered metal dichalcogenide materials[56]. It is, however, of little concern in studies of the formation macrosteps in our research. The macrosteps, though depending on the topic one wants to discuss, are defined as steps bunching of hundreds or even more steps. Therefore, one can consider the half-and full-unit-cell steps as elementary steps then study the further step bunching behaviors. The following section will introduce the energetic viewpoint on step bunching.

1.4.2 Step interactions

Elementary steps can bunch into macrosteps to lower the total surface energy[48, 57]. For a vicinal surface varies from the facet with a small angle θ, The surface energy can be written as

$$f_{\text{surf.}}(p) = \alpha(0) - \frac{\beta}{a}p - \frac{\phi}{a^3}p^3 + ..., \tag{1.2}$$

where $p = \tan\theta = a/r$ the slope of the vicinal surface, a is the step height and r is the step distance. The first and the second terms on the rightside represent the surface energy of the facet and the edge energy of steps, respectively. The third term describes the effect of step interactions. The surface energy, therefore, depends on step distance.

There are two opposite step interactions, the attractive interaction and the repulsive interaction[58]. The attractive interaction originates from the attractive interaction among atoms. Thus the attractive potential is proportional $1/r^3$. In the case of heteroepitaxial growth, another attractive long-range interaction, whose potential is proportional to $\ln(r)$, exists, while this interaction can be neglected in the case of homoepitaxial growth. Tersoff first introduced the idea of attractive step interaction in the analysis of step bunching instability with the linear analysis method[59].

On the other hand, repulsive interaction originates from 1) elastic deformation caused by steps or 2) an entropy effect at high temperatures. The repulsive potential originates from 1) can be written as

$$U(r) = \frac{2(1-\sigma^2)}{\pi E}(\tilde{\beta}a)^2\frac{1}{r^2} \tag{1.3}$$

where σ, E are the Poisson's ratio and Young's modulus, respectively. $\tilde{\beta}$ is the step stiffness and a the step height[60, 58]. The force works on a steps, $F = \partial U/\partial r$, is exactly the third term in the equation 1.2. Since the attractive interaction attenuates quickly with r increasing and thus can be neglected, in most cases, the repulsive interaction dominates. Strong repulsive interaction resists step bunching, the resistance can be represented by the so-called surface stiffness $\tilde{\alpha}_{\parallel} = 6\phi/(a^2r)$, where the subscript $\parallel$ means the transformation of surface is parallel to step lines. A numerical study on the influence of the repulsive force on step bunching can be found in[61].

Furthermore, some researches indicate that a vicinal surface could lower the surface energy by forming faceted macrosteps[62, 63]. That is, despite the high energy barrier for steps to get close to each other due to the repulsive interaction, once they cross the critical distance, the repulsive force quickly falls to zero[58].

Factor modifying surface energy and surface stiffness thereby can change the step bunching behavior of a vicinal surface. For example, impurities can adsorb to the terraces between steps and decrease the density of unsaturated bonds. With this theory, Ohtani *et al.* succeeded in explaining the change of step bunching behavior caused by nitrogen addition in the growth of 6H-SiC[62]. Lately, this theory is also applied to explain the effect of chromium and other elements and yield a qualitative consistency to the experimental results[30, 31]. One other reason is surface reconstruction. It also decreases unsaturated bonds and releases surface tension.

1.4.3 Step bunching as a surface instability

Nonetheless, this surface energy explanation is far from complete. First, one applies this theory to explain the observed step bunching phenomenon rarely shows how the surface energy is influenced, making the explanation unconvincing. Also, the exact value of surface energy is difficult to measure, especially when the surface is in contact with the liquid phase. Moreover, it fails in predicting the surface instability that occurs in transport-limited growth.

Instability occurs on a growing surface to form destructive morphologies such as dendrites and cellular structures. Usually, the instability occurs during solution growth or melt growth, known as transport-limited growth. The transport process of mass (growth units) or energy (latent heat released in crystallization) is several orders slower than the kinetic process of growth units being incorporated into the crystal. The classical constitutional supercooling theory and the dynamics model by Mullins-Sekerka succeeded in modeling this type of instability. The idea of Mullins and Sekerka is that the perturbation that occurred on a flat surface would induce a change in the uniform ambient phase. The inhomogeneity in the ambient phase reversely suppresses/enhances the perturbation, and thus the perturbation is strangled at birth/grows to instability. Furthermore, as Mullins's formula indicates, though the surface energy provides a constraint force that resists the surface from instability, it only works on a small length scale.

Step bunching is a surface instability if one considers the elementary process of step bunching, say, the paring of two neighboring steps. With an equally-spaced

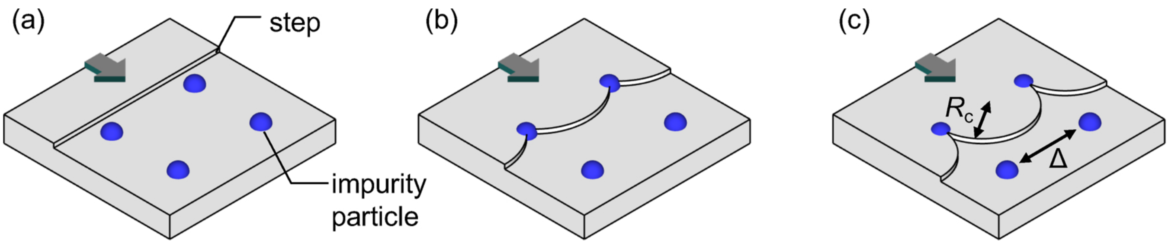

Figure 1.8 A schematic illustration of the step pinning process. The black arrays show the direction of the step advancing. (a) shows a step not yet influenced by impurity. (b) shows a step cutting through impurity particles. The step stops at impurity sites (pinning effect) while the segments between pinning sites bend forward. (c) shows a step completely stopped due to the pinning effect.

step train moving on the surface, select a step and put a perturbation on its position, say, by advancing a small displacement, the step velocity would be affected by the change in its front/behind terrace widths. If the step is decelerated, it will return to its initial position. Else, however, if the step is accelerated, it would continue to deviate from the initial position and finally catch the front step and form a step-pairing. With more and more steps pair with each other, step bunching occurs. The following subsections will introduce several common factors that cause step-pairing.

Impurity

Since Cabrera and Vermilyea (CV) have established the model for impurity pinning steps, the influence of impurities on step motion has been extensively investigated [64]. This model describes impurities adsorb on the surface, and when a flat step meets a row of impurities, the step stops at the points where the impurities are located, while the rest portion keeps advancing. Thereby the flat step breaks into a sequence of curved segments, as indicated in figure 1.8. Due to the well known Gibbs-Thomson effect, the effective driving force is decreased by the bending; thus, the step advancing rate decreases in

$$v_{\mathrm{st}} = v_{\mathrm{st}}^{0}(1 - 2R_{\mathrm{c}}/\Delta)^{1/2}, \tag{1.4}$$

where v_{st}^{0} is the step velocity when impurities are absent, Δ is the typical distance between impurities, and R_{c} is the critical radius for the 2D nucleation. An increasing in impurity concentration in the ambience phase could significantly decrease step velocities.

The fundamental consideration of impurity-induced step bunching is that the longer the exposure to the environment, the greater the impurity concentration on the surface. Therefore, if a step slows down, causing the front terrace to grow wider and the back terrace to shrink, the impurity density for this step becomes higher while for step behind becomes lower. Therefore, a variance among the step speeds occurs and leads to a step bunching[65].

In recent years, new results have started questioning this classical theory. Rile I. Ristic *et al.* realized that this mechanism works only for the fast-moving steps, while for the steps moving slow enough, no matter how broad the terraces are, the adsorption of impurities is saturated. Thus the variance among terrace widths will never change step velocities[66]. J. Lutsko *et al.* revisited the CV model through a kinetic Monte Carlo method and pointed out that the CV model only applies in the case of effectively large impurity clusters with long surface-residency times. At the same time, minor obstacles require much higher impurity concentrations to induce step pinning relative to the CV model's prediction because thermal fluctuations would drive the steps past the impurity fence[67]. In solution growth, J. J. De Yoreo *et al.* indicated that only high-soluble crystals obey this rule. Since the high solubility implies a minor kink-creation work, the high-soluble crystals allow strong step fluctuations and bending when meeting obstacles. For crystals of poor solubility, the steps show minor fluctuations. Thus the curvature required in equation 1.4 is absent. In this case, it is the kink poison mechanism that hinders the step motion instead of the CV mechanism[68]. That implies that the impurity-induced step bunching, based on the step-pinning mechanism, may not be valid for the low-soluble crystals.

Schwoebel effect

Step bunching due to the Schwoebel effect (also known as the ES effect) usually occurs in a growth system modeled by the BCF theory, The route for the growth unit is ambient phase → surface → steps. This route usually occurs in growth from an ambiance of the vapor phase. Atoms adsorb on the terrace, diffuse, and finally desorb or be incorporated into steps. The incorporation process happens on both the downside and the upside of a step. However, Schwoebel indicated that the incorporation rates on the two sides are usually different due to the different energy barriers for the atom must cross over[69]. Consider the case the incorporation from upside terrace is faster and thus the significant process. When a step moves faster than the neighbor ones, it finds the terrace width behind itself becomes wider, and the coming flux of adsorption atoms on the upside terrace increases, thus its motion is further accelerated, and finally, it will collide into the neighboring step in the front[70].

Note that the asymmetric incorporation rate of growth units on the two sides of a step can also originate in external reasons, *e.g.*, the drift of adsorbed growth units due to an external electric field. Therefore an electric field that drives growth unit drifting in an up-step direction results in step bunching during crystal growth, while an electric field placed in the opposite direction stabilizes the step train[71, 72].

Solution convection

A. A. Chernov first studied the effect on step bunching of solution convection near the growing surface[73–75]. During growth, a flow direction is the same as the step motion direction, say, the down-step direction, enhancing the step bunching and *vice versa*. Although the mathematical derivations are sometimes complicated, one can conclude that the solute concentration in the solution above a bunch of steps decreases due to immediate consumption. A down-step flow drives the depleted solution towards the front of the step bunch. That results in the head of the step bunch moving even slower, and thus the bunch gets more and more developed. Later Zhu *et al.* revealed the same phenomenon in solution growth of SiC crystal with the TSSG method. He observed that keeping an anti-parallel flow (the up-step flow) during growth leads to smooth surface morphology and can even flatten a rough surface by dissipating step bunching[12].

Flow controlling has become a primary issue for developing crafts for solution growth of large-sized SiC. However, it is difficult to maintain an anti-parallel flow over the growth surface. Chernov concluded a criterion that the surface stays stable under a parallel flow. That is

$$\frac{2\pi u \delta_c}{\mathcal{D} k} < \frac{2\pi^2}{\bar{p}}, \tag{1.5}$$

where u is the flow velocity at the upper boundary of the stagnant layer, δ_c the so-called characteristic length, $\mathcal{D}$ the diffusion coefficient, k the wavenumber of surface fluctuation, and $\bar{p}$ the average slope of the surface. The left side of the inequality is a non-dimensional Peclet number. This criterion may help design growth crafts. The linear analysis treats step bunchings as a superposition of waves on the surface profile and tells which wave would grow up (indicating instability) and remain stable or disappear. However, the linear analysis gives no information about how the instability develops. Nonetheless, the development of surface instability, especially its time dependence, is of great significance in real crystal growth.

1.4.4 Supersaturation gradient induced step bunching

A supersaturation gradient on the growing surface in the step motion direction can cause step bunching, mainly when growing crystals of considerable size. Such supersaturation gradient could be induced by the surface temperature distribution, step bunches formed earlier[76] or turbulence[77].

1.5 Multiscale modeling of crystal growth in a solution ambiance

The processes involved in crystallization can be generally divided into 1) the transport of mass and heat to the crystal surface and 2) the incorporation of growth units at the surface, called surface kinetics. The transport of mass and heat involves convection and diffusion in the ambiance, which is usually a fluid (vapor or liquid). The surface kinetics is greatly influenced by the surface structure and the properties of the crystal itself. Chernov invented the kinetic coefficient, $\mathcal{K}$, to characterize the surface kinetic. It is defined by the speed growth units near the surface that can be incorporated.

Both processes influence the growth morphology, thereby the quality of the grown crystal. However, only in a few cases, the two processes can be observed directly. Unfortunately, due to the extreme conditions required for the growth, the solution growth of SiC does not fall in this scope. This inconvenience significantly hinders us from effectively controlling the growth processes and obtaining high-quality crystals. In order to overcome this difficulty, numerical investigations are widely utilized in researches of crystal growth. Particularly, the step bunching behavior, which is in great concern of this thesis, as introduced in the last sections, is affected by many factors coupling mass transport and surface kinetics in different length scales. Therefore, a multiscale numerical investigation is required of how the two processes affect the step bunching behavior.

Figure 1.9 shows the schematic of models that describe crystal growth in different scales. The schematic of the macroscale model (figure 1.9 (a)) reflects the configuration of the TSSG method. One usually utilizes the macroscale model to obtain the information about mass-and-heat transport in the ambiance phase, *e.g.* the temperature distribution and flow velocity inside the fluid. However, when the macroscale model handles the interface kinetics as mass and heat flux at boundaries, an approximation is usually applied, assuming the surface kinetics completed in an instant and the anisotropy is usually neglected. However, as one will see in chapter 3, coupling the surface kinetics with mass transport is particularly important when discussing the step bunching problem. Therefore, a mesoscale model coupling surface kinetics with mass transport is necessary. Figure 1.9 (b) shows a schematic of an mesoscale model. The atomistic (microscale) model directly considers the movement of growth units and intends to gain more detailed information such as the shape of steps and impurities of impurities. Figure 1.9 (c) shows a schematic of an atomistic model.

The following sections introduce theories of crystal growth and corresponding models in each scale.

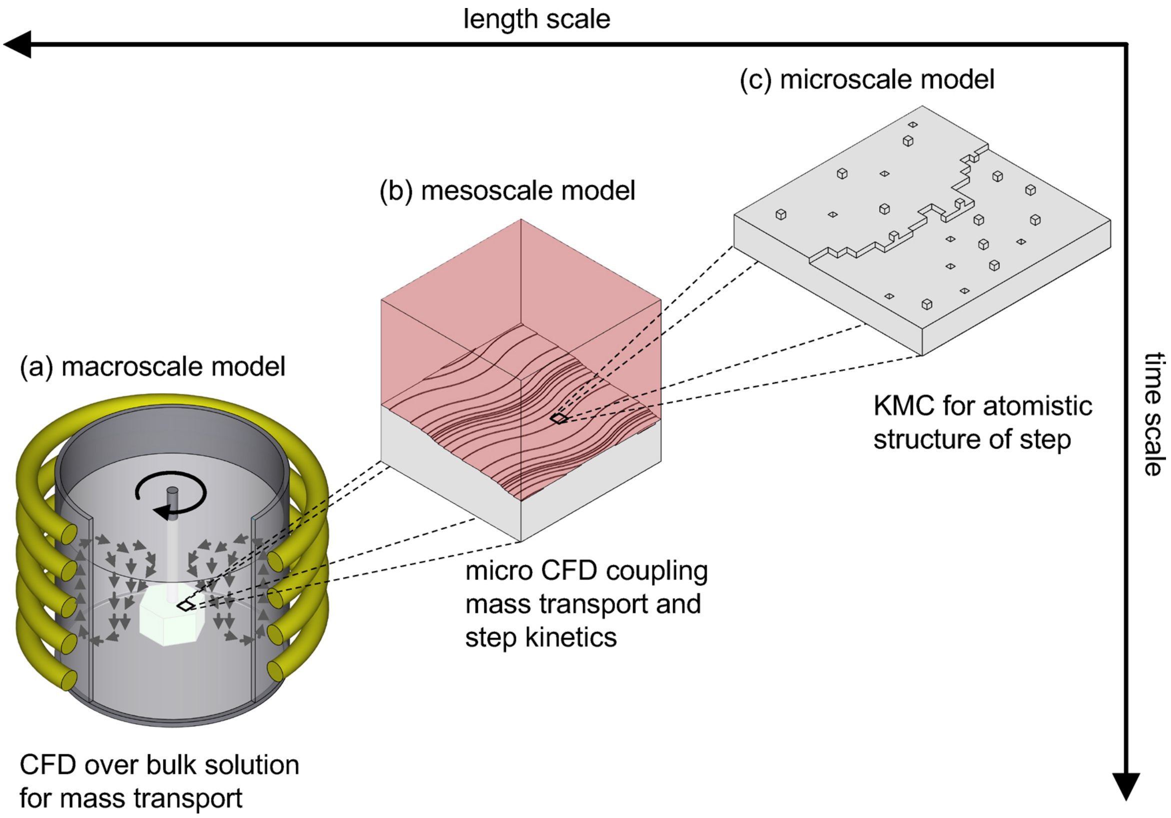

Figure 1.9 Modeling and the corresponding methods of a crystal growth process in different scales.

1.5.1 Continuum modeling of mass transport

Crystal growth usually involves mass and heat (energy) transport in the ambient phase. Mass transport includes convection and diffusion, while heat transport includes heat convection, conduction, and radiation. In most cases, the ambient phase is a fluid, *i.e.*, a melt, solution, or vapor. Therefore, the mass and heat transport problem can be dealt with by an application of fluid mechanics. Governing equations obtained from the conservation laws of momentum, mass, energy, and species describe fluid motion. The governing equations for the four conservations can be written in a general form,

$$\frac{\partial \rho\phi}{\partial t} + \nabla \cdot (\rho \boldsymbol{u} \phi) = \nabla \cdot (\Gamma \nabla \phi) + S, \tag{1.6}$$

where ϕ is the variable for solving, Γ is the general diffusion coefficient, and S is the general source item. Table 1.2 listed up the specialized forms of symbols in the governing equation corresponding to the particular equations, the meaning of each symbol is listed in table 1.3. By solving and analyzing the governing equations, the distribution and change of physical quantities corresponding to ϕ can be obtained.

Table 1.2 The specilization of the symbols in the general governing equation.

Equation	ϕ	Γ	S
Continuity equation	1	0	0
Momentum equation	u_i	μ	$-\partial p/\partial x_\mathrm{i} + S_\mathrm{i}$
Energy equation	T	k/c	S_T
Species equation	c_s	$\mathcal{D}_\mathrm{s}\rho$	S_s

Table 1.3 Meaning of the symbols in the specilized governing equation.

u_i	component of fluid velocity vector
μ	dynamic viscosity
p	pressure
S_i	body force
T	temperature
k	heat transfer coefficient
c	specific heat capacity
S_T	heat source
c_s	concentration of species s
$\mathcal{D}_\mathrm{s}$	diffusion coefficient
ρ	density
S_s	source of species s

It is worth noting that the release and absorption of the species due to any in-solution chemical reaction or phase transition can be included in the source item of the species conservation equation. While those that occur at the interfaces are defined use boundary conditions. Particularly, the solute flux towards crystal surface due to diffusion, and the incorporation flux should be balanced,

$$\mathcal{D}\nabla c_{\mathrm{s}} = \mathcal{K}(\boldsymbol{n})(c_{\mathrm{s}} - c_{\mathrm{eq}}), \tag{1.7}$$

where $\mathcal{K}(\boldsymbol{n})$ is defined as the growth kinetic coefficient, $\boldsymbol{n}$ in the normal vector of the surface, and c with the subscipts "s" and "eq" respectively represent the real and equilibrium solute concentration at the crystal surface. With the flux, the growth rate of the surface $\boldsymbol{n}$ can be obtained as

$$R(\boldsymbol{n}) \propto \mathcal{K}(\boldsymbol{n})(c_{\mathrm{s}} - c_{\mathrm{eq}}). \tag{1.8}$$

In application, the mass and heat transport problems are simulated, analyzed, and solved using computer-based numerical analysis and algorithms known as computational fluid dynamics (CFD). As the most extensively applied modeling gathering most engineering concern, plenty of commercial CFD simulation software is available for modeling all kinds of crystallization processes, including those using the TSSG method.

1.5.2 Mesoscale modeling of vicinal surface

With the macroscale model, one gains insight into mass and heat transport in the entire ambient phase. Macroscopic quantities, such as crystal growth and crucible dissolving rates, can be obtained in length and time scales of centimeters and hours. By carefully setting growth kinetic coefficients $\mathcal{K}(\boldsymbol{n})$ for different growth directions, one can even predict the crystalline phase. However, the model in this scale is not compatible in acquiring information on scales smaller than the grid size.

On the other hand, crystal growth is governed by mass transport and surface kinetics. In contrast to the mass transport process, the mass exchange between the ambient and crystal depends on the surface structure and shows significant anisotropy.

Four main growth mechanisms can occur on the surface. Figure 1.10 gives a schematic representation of the four mechanisms. The normal growth occurs only on rough surfaces, which is usually valid in the cases like metals growing from their melts because the temperature of solidification is usually higher than the roughening transition temperature. In the case of SiC solution growth, however, growth occurs

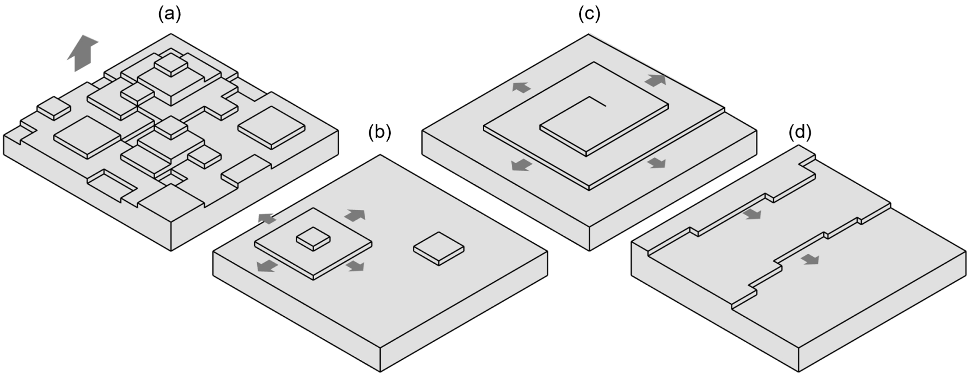

Figure 1.10 Schematics of (a) the normal growth, (b) the 2D nucleation growth, (c) the spiral growth, and (d) the step-flow growth. The grey array in (a) indicates the growth direction of the rough face, while the grey arrays in (b-d) indicate the growth direction of steps.

on flat surfaces such as the {0001} facets or vicinal faces deviate from the {0001} facets for small off-angles.

The rest three mechanisms describe the growth on flat surfaces. On facets, growth occurs through either the 2D nucleation growth mechanism (figure 1.10 (b)) or the spiral growth mechanism (Figure 1.10 (c)). 2D nucleation can form on the surface when a critical driving force is reached. The edges of nucleations are steps providing preferential incorporation sites for growth units to bond. The edges of 2D islands spread over the surface so that the crystal grows layer by layer. If the screw dislocation intersects the crystal surface, the discontinuity on the surface provides nonvanishing steps on the crystal surface. In this mechanism, 2D nucleation is not necessary, and crystals can grow at a low driving force.

On vicinal faces, the step flow mechanism dominates, figure 1.10 (d). Steps provided by either 2D nucleations or spiral centers are minorly influenced by their sources when they spread far away enough. In that case, the step flow mechanism also applies to the growth of these steps. From a mesoscale viewpoint, the steps act as linear sinks for the growth units in solution growth. The growth rate of a step is

$$v_{\mathrm{st}} = \mathcal{K}_{\mathrm{st}}(c_{\mathrm{st}} - c_{\mathrm{eq}})v_{\mathrm{c}}, \tag{1.9}$$

where $\mathcal{K}_{\mathrm{st}}$ is the step kinetic coefficient and v_{c} is the volume of a growth unit. The concentration of growth unit near the step, c_{st}, is determined by a balance between the mass transport and consumption of the step as indicated by equation 1.7. That implies that one can apply the same methods in the continuum model to obtain the values of c_{st} to calculate step velocities, thus the evolution of step positions. For each elementary step, $\mathcal{K}_{\rm st}$ characterizes the rate of incorporating growth units. With this $\mathcal{K}_{\rm st}$, the motion of each step can be separately simulated, which is necessary for simulating step bunching. However, directly involving these delicate processes would be very computationally expensive in the macroscale models. Therefore, a mesoscale model, coupling the step kinetics and the mass transport near the steps, is necessary to investigate step bunching behaviors. Some mesoscale models for step motion have been reported in previous studies[76, 78, 79].

1.5.3 Atomistic modeling of surface process

The mesoscale and continuum models are half-empirical. To apply these models, one has to assign some of the physical properties empirically. While some of the physical properties, *e.g.*, the step kinetic coefficient, are not easy to be experimentally determined. Crystal growth by the step flow mechanism involves incorporating growth units into the steps. While the kink sites play an essential role in the growth. The step kinetic coefficient $\mathcal{K}_{\rm st}$ is a function of the kink density, a/δ_0,

$$\mathcal{K}_{\rm st} = a\nu\frac{a}{\delta_0}\exp(-\frac{\Delta U}{k_{\rm B}T}), \tag{1.10}$$

where ν is the attempt frequency, a the length of a growth unit, δ_0 the average distance between kink sites, and ΔU the energy barrier for growth unit to crossover for a growth unit to incorporate into the crystal. In this viewpoint, the step kinetic coefficient is a function of the atom arrangement at the step edge. Therefore, for a better understanding of the crystal growth, starting from atomic behavior to investigate crystal growth, thus the modeling in-depth into an atomic scale is found necessary.

Figure 1.11 gives a schematic of a {001} Kossel surface with a step on it. Kossel model is a model using connected blocks to represent molecules or atoms. Due to either a thermal fluctuation or depositing/removing growth units, the step can deviate from its "perfect" position, which is supposed to be straight. With that deviation, kink sites form at the corners where the step line changes direction. Under some extreme conditions, adatoms/vacancies can also form on the surface. For a Kossel crystal, the kink density is $(1 + 1/2\exp(\omega/kT))^{-1}$, where ω is the kink creation work. The step kinetic coefficient can be easily estimated using ω and ΔU data. However, it is not easy to determine the kink density for more complicated crystals. While through atomistic simulations of the crystal surface containing steps, one can obtain the step structure at certain conditions, thereby obtaining the step

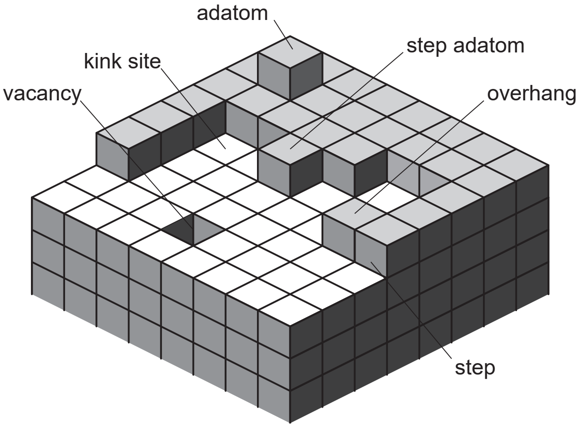

Figure 1.11 A atomistic structure of a Kossel crystal's {001} surface, indicating differet configurations.

kinetic coefficient information, or calculate it as a ratio between step velocity and driving force, as indicated in equation 1.9. Furthermore, an atomistic model also helps investigate other microscopic mechanisms like how impurities influence step motion.

For the length scale of steps on the crystal surface, molecular dynamics and the Monte Carlo method are suitable. For SiC crystal, these methods as well have been widely utilized in solving problems of step reconstruction and step bunching[80–82]. This thesis applied a kinetic Monte Carlo (KMC) method to investigate step kinetics on an atomistic scale. The following sections introduce the basic ideas of KMC.

kinetic Monte Carlo method

In the atomic simulation, molecular dynamics (MD) is excellent. It can describe the evolutionary trajectory of a system very accurately. In general, time steps in MD are on the order of femtoseconds (10^{-15}s), which is sufficient to track specific changes in atomic vibrations. However, this advantage also limits the application of MD to simulations on large time scales. Although nowadays computers can support MDs of up to tens ns with well-designed algorithms, the dynamic processes in our interests have periods of more than seconds, far beyond MD's applicability. The kinetic Monte Carlo (KMC) methods were proposed to satisfy the needs of studies on complex systems and complex processes. Until now, KMC has been widely utilized in investigations on crystal growth such as spiral growth [83], thermal roughening [84, 85], formation of polytype [82] and step bunching [50, 86]. We constructed a

KMC model to investigate the step structure and the mechanisms of impurities affecting step motion. The following part briefly introduces the principle of KMC.

When the system is in a steady-state, we can describe it as being at a local minimum (bottom trap) of the potential energy function surface. At finite temperature, although the atoms in the system are in constant thermal motion, they spend most of their time vibrating near the bottom of the potential energy trap. Occasionally the system crosses the potential barrier between the different potential traps and completes an "evolution", and it is this small probability determines the evolution of the system. Therefore, if we upgrade the focus from "atoms" to "systems" and coarsen the "atomic trajectories" to "system state leaps" then the time scale of the simulation will be increased from the scale of atomic vibrations to the scale of system state leaps.

A leap pathway $i \rightarrow j$ describing the system going scaping from state i to state j can be characterized by rate k_{ij}, which depends only on the current system state i. By constructing a stochastic process that makes the system evolve according to the event rates, in which the probability of each evolutionary trajectory is the same as in the MD simulation, we can study the evolution of a system.

The rate constant and time evoluation Because the time interval between the leaps (the KMC events) is very long, two subsequent evolutions can be considered independent, *i.e.* follow the Poisson distribution. That gives the probabibility for the system NOT escaping from state i after time t passed by

$$P_{\text{stay}}(t) = \exp(-k_{\text{tot}}t), \tag{1.11}$$

where k_{tot} is the sum of the rates k_{ij} of all possible leap paths when the system is in state i,

$$k_{\text{tot}} = \sum_j k_{ij}. \tag{1.12}$$

The escape probability of the system then accumulates with time, so $P_{\text{escape}}(t)$ integrated over time to a certain moment t' must be equal to $1 - P_{\text{stay}}(t')$. That gives the probability distribution function of the escaption.

$$p(t) = \frac{\partial P_{\text{escape}}(t)}{\partial t} = k_{\text{tot}} \exp(-k_{\text{tot}}t). \tag{1.13}$$

For each specific leap path k_{ij}, the above discussion holds. Therefore, we can define the probability distribution function $p_{ij}(t)$ of the system making a jump $i \rightarrow j$ per unit time as

$$p_{ij}(t) = k_{ij} \exp(-k_{ij}t) \tag{1.14}$$

The time step δt of KMC, representing the time for escaping from state, i, should follow the geometric distribution. This can be obtained by drawing a random number r on the interval (0,1], and forming

$$\delta t = -\frac{1}{k_{\text{tot}}} \ln r. \tag{1.15}$$

Procedure of KMC KMC has several implementations. Here we introduce the direct method which was used in the study. The direct method is one of the most commonly used KMC algorithms and is very efficient. Each step only requires the generation of two random numbers, r_1 and r_2, equally distributed in $(0, 1]$, where r_1 is used to select the leap paths and r_2 determines the forward time of the simulation. Let the system be in state i, and imagine each leap path j as a line segment whose length is proportional to the leap rate k_{ij}. Connect these line segments at the beginning and end to a line whose total length is proportional to $k_{\text{tot}} = \Sigma_j k_{ij}$. If $r_1 k_{\text{tot}}$ falls within a line segment q, the leap path $i \to q$ represented by that line segment is selected, and the system moves to the state q while the system time advances according to equation 1.15. To summarize its algorithm as follows

1. calculate the total leap rate when the system is in state i according to equation 1.12.
2. generate a random number r_1;
3. find the path $i \to q$ that satisfies $\Sigma_{j=1}^{q-1} k_{ij} \leqslant r_1 k_{\text{tot}} \leqslant \Sigma_{j=1}^{q} k_{ij}$;
4. move the system to the state q while simulating the time advance according to equation 1.15;
5. repeat the above process.

The lattice assumption Applications of KMC in solid-state physics often involve mapping atoms to a specific lattice. Thus, the events are viewed as atomic lattice point relationships changes. Although this method is not precisely consistent with the actual situation, it simplifies the modeling effort in many cases and is a reasonable approximation according to previous results. (In many cases, the atoms in the system all deviate to some extent from the ideal lattice point, but not too much

(~$0.01a$), so this atomic point mapping is valid.) Another advantage of this approach is that the events can be localized. Each event is only relevant to its immediate system environment, significantly reducing the number of leap pathways and thus simplifying the calculation[87]. It is important to note that this mapping is unnecessary for KMC simulations. For example, in a molecular chemical reaction or the growth of biomolecules, the lattice does not exist.

Rate determination With knowledge about the leap pathway, one can calculate the rate constant with the transition state theory, in which the pathway is characterized by a saddle point on the potential energy surface, as shown in figure 1.12. Leaving out the derivation processes, a very simplified form of rate constant can be written as

$$k = \nu_0 \exp(-\Delta E / k_B T), \tag{1.16}$$

where the prefactor is often in the range of 10^{12} s^{-1} - 10^{13} s^{-1}, a common approximation is to choose a fixed value in this range to save the computational source[87]. The $\Delta E = E_{\text{saddle}} - E_{\text{minimum}}$ is the energy difference between the saddle point and the minimum. With the lattice assumption, a reasonable assumption is that additive interactions can approximate the barrier height. That is,

$$E = \Sigma \phi. \tag{1.17}$$

Here ϕ is the energy of the additive interactions, which can be specified according to the results of experiments or other simulations. Particularly, for KMC used in crystal growth, we can specify the barrier height for a growth unit to deposite at and be removed from the half-crystal position (kink site) as

$$\begin{aligned} \Delta E_{\text{dep}} &= \Delta U, \\ \Delta E_{\text{rem}} &= \Delta U + \Delta h. \end{aligned} \tag{1.18}$$

Here Δh is the enthalpy of the transition (sublimation, dissolution, or fusion) corresponding to the crystallization process. ΔU is the kinetic barrier for the incorporation of the growth units into the half-crystal position connected with proceeding chemical reactions, desolvation in solution growth, or viscous flow in growth in melt growth[57]. The enthalpy can be written as summation of "effective bonding energy", φ

$$\Delta h = z\varphi, \tag{1.19}$$

where z is the number of direct neighbors of each growth unit in the solid-state, usually the coordination number.

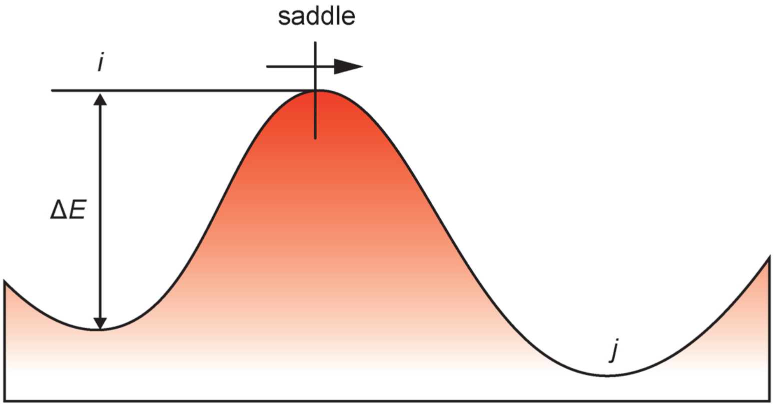

Figure 1.12 Illustration of the transition state theory rate constant. The red array shows the transition pathway, $i \rightarrow j$, across the saddle point.

For more information about KMC, one might want to refer to the references for rate determining[87], for quick searching algorithm[88, 89] and for lattice constructing [82].

1.6 Relation to Real-World Data Circulation

The relation of this thesis to Real-World Data Circulation (RWDC) is discussed. First, the concept of RWDC can be briefly explained as follows.

1. Data acquisition. Data is acquired by an investigation into natural phenomena or human activities. In some fields, data can also be acquired by experiments.

2. Data analysis. The acquired data is analyzed to extract useful information and form general principles that help humans understand natural phenomena or society. In some cases, the understanding of the system is reflected in computer modeling.

3. Data implementation. The knowledge is utilized to improve the behaviors of the systems where the data is acquired, completing the data circulation. The implementation usually involves predicting and controlling natural phenomena, improving industrial products or services, or decision-making in social affairs.

This thesis focus on the growth processes of 4H-SiC crystal from a liquid phase ambiance, which requires a multiscale understanding of the whole system's behavior, including mass and energy transport in the macroscale, the surface kinetics in the mesoscale, and the atomistic interaction in the microscale.

Conventionally, it is not easy to directly relate the obtained crystals to the conditions of the experiments. Although both are macroscopic objects, the latter determines the former through complicated mechanisms hiding in the more minor scales, hardly observed with experimental approaches. This difficulty hinders researchers from improving the growth conditions through the previously obtained crystals.

The research of this thesis provides a systematic understanding of the step bunching phenomenon, building a bridge linking the input and output during crystal growth. Moreover, the insights gained by this thesis can be implemented to create an emulator, which reproduces the crystal growth processes in a computer model. Utilizing this emulator, researchers can explore the parameter space for the optimized controlling conditions for crystal growth but significantly save time and cost.

1.7 Objective and contents of this thesis

As described above, the demand for high-quality SiC bulk crystals is becoming more urgent and higher with the development of power devices used under high power, high frequency, and high temperature. The quality of grown crystals has been dramatically improved due to the effort for several decades. However, dislocations such as macropipes or TSDs still hamper the realization of high-quality SiC crystals. Solution growth is considered a promising method for high-quality SiC crystal growth not only the growth conducted under the condition close to thermal equilibrium and the threading dislocation could convert to defects on the basal plane. Macro steps have been found critical for dislocation conversion, while over-developed macrosteps induce other defects. Controlling the structure of macrosteps according to different purposes is critical for high-quality SiC crystals. As an essential process in macrostep formation, knowledge about step bunching is necessary to control the formation and dissipation of macrosteps. Thus, investigation on step bunching remains crucial.

In this thesis, a multiscale numerical investigation is utilized to reveal the mechanism of step bunching in solution growth. The effects of solute transport in fluid and step kinetics on step bunching were extensively studied.

Our objective is to realize a smooth grown surface by solution growth.

This thesis is divided into six parts. The specific structure and contents are as follow:

1. In chapter 1, this thesis's background and objective are introduced.
2. In chapter 2, the result of the growth of large diameter SiC crystal is described. The phenomena of step height and TSD conversion ratio distribution are described and explained with a macroscale CFD simulation.
3. In chapter 3, a mesoscale CFD model coupling step kinetics and mass transport near crystal surface is constructed. The effect of fluid flow on step bunching size is quantitatively studied. Then, the effect of solvent properties on step bunching behavior is investigated.
4. In chapter 4, a KMC simulation model of 4H-SiC surface is constructed. The step kinetic coefficient is calculated over different temperatures and supersaturation. Then, an aluminum-like impurity is introduced in the simulation. The impurity's effects on step kinetics and step bunching behavior are studied.
5. In chapter 5, the relationship of this thesis with the Real-World Data Circulation was discussed.
6. In chapter 6, the conclusion of this thesis is described.

References

[1] J. Conti, P. Holtberg, J. Diefenderfer, A. LaRose, J. T. Turnure, and L. Westfall, 10.2172/1296780.

[2] T. Kimoto and J. Cooper, *Fundamentals of Silicon Carbide Technology: Growth, Characterization, Devices and Applications* (Wiley, 2014).

[3] L. Gear, “Tesla’s Innovative Power Electronics: The Silicon Carbide Inverter,” Tech. Rep. (2021).

[4] “ROHM supplies Full SiC Power Modules to Formula E racing team Venturi, Enhancing performance through significant reduction of size and weight,” https://www.rohm.com/news-detail?news-title=rohm-supplies-full-sic-power-modules-to-formula-e-racing-team-venturi&defaultGroupId=false (2018).

[5] H. Lin and A. Villamor, “POWER SIC 2018: MATERIALS, DEVICES AND APPLICATIONS, Automotive is putting SiC on the road. Is the supply chain ready?” Market & Technology Report (Yole Developpment, 2018).

[6] D. Nakamura, I. Gunjishima, S. Yamaguchi, T. Ito, A. Okamoto, H. Kondo, S. Onda, and K. Takatori, Nature **430**, 1009 (2004).

[7] K. Murayama, T. Hori, S. Harada, S. Xiao, M. Tagawa, and T. Ujihara, Journal of Crystal Growth **468**, 874 (2017).

[8] R. A. Stein, P. Lanig, and S. Leibenzeder, Materials Science and Engineering: B **11**, 69 (1992).

[9] R. A. Stein and P. Lanig, Journal of Crystal Growth **131**, 71 (1993).

[10] T. Kimoto, H. Nishino, W. S. Yoo, and H. Matsunami, Journal of Applied Physics **73**, 726 (1993).

[11] S. Harada, Alexander, K. Seki, Y. Yamamoto, C. Zhu, Y. Yamamoto, S. Arai, J. Yamasaki, N. Tanaka, and T. Ujihara, Crystal Growth & Design **12**, 3209 (2012).

[12] C. Zhu, S. Harada, K. Seki, H. Zhang, H. Niinomi, M. Tagawa, and T. Ujihara, Crystal Growth & Design **13**, 3691 (2013).

[13] M. Kasu and N. Kobayashi, Journal of Applied Physics **78**, 3026 (1995).

[14] I. Bryan, Z. Bryan, S. Mita, A. Rice, J. Tweedie, R. Collazo, and Z. Sitar, Journal of Crystal Growth **438**, 81 (2016).

[15] C. Liu, X. Chen, T. Peng, B. Wang, W. Wang, and Gang Wang, Journal of Crystal Growth **394**, 126 (2014).

[16] R. I. Scace and G. A. Slack, The Journal of Chemical Physics **30**, 1551 (1959).

[17] D. H. Hofmann and M. H. Müller, Materials Science and Engineering: B **61**, 29 (1999).

[18] M. Syväjärvi, Journal of The Electrochemical Society **146**, 1565 (1999).

[19] K. Kusunoki, S. Munetoh, K. Kamei, M. Hasebe, T. Ujihara, and K. Nakajima, in *Materials Science Forum*, Vol. 457 (Trans Tech Publ, 2004) pp. 123–126.

[20] T. Yoshikawa, S. Kawanishi, and T. Tanaka, Japanese Journal of Applied Physics **49**, 051302 (2010).

[21] K. Danno, H. Saitoh, A. Seki, H. Daikoku, Y. Fujiwara, T. Ishii, H. Sakamoto, and Y. Kawai, Materials Science Forum **645-648**, 13 (2010).

[22] H. Daikoku, M. Kado, H. Sakamoto, H. Suzuki, T. Bessho, K. Kusunoki, N. Yashiro, N. Okada, K. Moriguchi, and K. Kamei, Materials Science Forum **717-720**, 61 (2012).

[23] M. Kado, H. Daikoku, H. Sakamoto, H. Suzuki, T. Bessho, N. Yashiro, K. Kusunoki, N. Okada, K. Moriguchi, and K. Kamei, Materials Science Forum **740-742**, 73 (2013).

[24] T. Narumi, S. Kawanishi, T. Yoshikawa, K. Kusunoki, K. Kamei, H. Daikoku, and H. Sakamoto, Journal of Crystal Growth **408**, 25 (2014).

[25] T. Mitani, N. Komatsu, T. Takahashi, T. Kato, K. Fujii, T. Ujihara, Y. Matsumoto, K. Kurashige, and H. Okumura, Journal of Crystal Growth **401**, 681 (2014).

[26] N. Komatsu, T. Mitani, Y. Hayashi, T. Kato, S. Harada, T. Ujihara, and H. Okumura, Journal of Crystal Growth **458**, 37 (2017).

[27] S. Kawanishi, Y. Nagamatsu, T. Yoshikawa, and H. Shibata, Journal of Crystal Growth **549**, 125877 (2020).

[28] K. Kusunoki, K. Kamei, N. Yashiro, K. Moriguchi, and N. Okada, in *Materials Science Forum*, Vol. 679 (Trans Tech Publ, 2011) pp. 36–39.

[29] N. Komatsu, T. Mitani, T. Takahashi, M. Okamura, T. Kato, and H. Okumura, Materials Science Forum **740-742**, 23 (2013).

[30] T. Mitani, N. Komatsu, T. Takahashi, T. Kato, S. Harada, T. Ujihara, Y. Matsumoto, K. Kurashige, and H. Okumura, Journal of Crystal Growth **423**, 45 (2015).

[31] N. Komatsu, T. Mitani, Y. Hayashi, T. Kato, and H. Okumura, in *Materials Science Forum*, Vol. 924 (Trans Tech Publ, 2018) pp. 55–59.

[32] A. Onuma, S. Maruyama, N. Komatsu, T. Mitani, T. Kato, H. Okumura, and Y. Matsumoto, Crystal Growth & Design **17**, 2844 (2017).

[33] S. Xiao, N. Hara, S. Harada, K. Murayama, K. Aoyagi, T. Sakai, and T. Ujihara, Materials Science Forum **821-823**, 39 (2015).

[34] H. Daikoku, M. Kado, A. Seki, K. Sato, T. Bessho, K. Kusunoki, H. Kaidou, Y. Kishida, K. Moriguchi, and K. Kamei, Crystal Growth & Design **16**, 1256 (2016).

[35] K. Ariyawong, Y. J. Shin, J.-M. Dedulle, and D. Chaussende, Crystal Growth & Design **16**, 3231 (2016).

[36] T. Kimoto, Japanese Journal of Applied Physics **54**, 040103 (2015).

[37] Y. Yamamoto, S. Harada, K. Seki, A. Horio, T. Mitsuhashi, and T. Ujihara, Applied Physics Express **5** (2012), 10.1143/apex.5.115501.

[38] H. Tsuchida, R. Takanashi, I. Kamata, N. Hoshino, E. Makino, and J. Kojima, Journal of Crystal Growth **402**, 260 (2014).

[39] Y. Yamamoto, S. Harada, K. Seki, A. Horio, T. Mitsuhashi, D. Koike, M. Tagawa, and T. Ujihara, Applied Physics Express **7**, 065501 (2014).

[40] S. Ha, P. Mieszkowski, M. Skowronski, and L. Rowland, Journal of Crystal Growth **244**, 257 (2002).

[41] S. Xiao, S. Harada, K. Murayama, M. Tagawa, and T. Ujihara, Crystal Growth & Design **16**, 6436 (2016).

[42] T. Nishinaga, C. Sasaoka, and K. Pak, Japanese Journal of Applied Physics **28**, 836 (1989).

[43] T. Nishinaga, Crystal Research and Technology **48**, 200 (2013).

[44] E. Bauser and H. Strunk, Journal of Crystal Growth **69**, 561 (1984).

[45] C. Zhu, X. Liu, S. Harada, M. Tagawa, and T. Ujihara, unpublished .

[46] A. A. Chernov, *Modern Crystallography III*, edited by M. Cardona, P. Fulde, and H.-J. Queisser, Springer Series in Solid-State Sciences, Vol. 36 (Springer Berlin Heidelberg, Berlin, Heidelberg, 1984).

[47] T. Kimoto, A. Itoh, H. Matsunami, and T. Okano, J. Appl. Phys. **81**, 8 (1997).

[48] A. Nakajima, H. Yokoya, Y. Furukawa, and H. Yonezu, Journal of Applied Physics **97**, 104919 (2005).

[49] V. Heine, C. Cheng, and R. J. Needs, Journal of the American Ceramic Society **74**, 2630 (1991).

[50] V. Borovikov and A. Zangwill, Physical Review B **79** (2009), 10.1103/PhysRevB.79.245413.

[51] W. Wulfhekel, D. Sander, S. Nitsche, F. Dulot, A. Leycuras, and M. Hanbücken, Surface Science **550**, 8 (2004).

[52] Y. Tabuchi, K. Ashida, M. Sonoda, T. Kaneko, N. Ohtani, M. Katsuno, S. Sato, H. Tsuge, and T. Fujimoto, Journal of Applied Physics **122**, 075702 (2017).

[53] X. Shen and H. Okumura, Journal of Crystal Growth **300**, 75 (2007).

[54] G. Ju, D. Xu, C. Thompson, M. J. Highland, J. A. Eastman, W. Walkosz, P. Zapol, and G. B. Stephenson, Physical Review B **103**, 125402 (2021).

[55] S. Nie, N. C. Bartelt, and K. Thürmer, Physical Review B **84**, 035420 (2011).

[56] M. J. Shearer, L. Samad, Y. Zhang, Y. Zhao, A. Puretzky, K. W. Eliceiri, J. C. Wright, R. J. Hamers, and S. Jin, Journal of the American Chemical Society **139**, 3496 (2017).

[57] I. V. Markov, *Crystal Growth for Beginners: Fundamentals of Nucleation, Crystal Growth and Epitaxy*, 3rd ed. (World Scientific, New Jersey, 2016).

[58] P. Muller, Surface Science Reports **54**, 157 (2004).

[59] J. Tersoff, Y. H. Phang, Z. Zhang, and M. G. Lagally, Physical Review Letters **75**, 2730 (1995).

[60] V. I. Marchenko and A. Y. Parshin, Sov. Phys. JETP **52**, 131 (1980).

[61] M. Inaba and M. Sato, Journal of the Physical Society of Japan **81** (2012), 10.1143/jpsj.81.064601.

[62] N. Ohtani, M. Katsuno, J. Takahashi, H. Yashiro, and M. Kanaya, Physical Review B **59**, 4592 (1999).

[63] T. Mitani, K. Naoyoshi, and K. Tomohisa, Journal of the Japanese Association for Crystal Growth **45** (2018), 10.19009/jjacg.3-45-2-02.

[64] N. Cabrera and D. A. Vermilea, in *Growth and Perfection of Crystals* (Cooperstown, New York, 1958) p. 411.

[65] J. van der Eerden and H. Müller-Krumbhaar, Electrochimica Acta **31**, 1007 (1986).

[66] R. I. Ristic, J. J. DeYoreo, and C. M. Chew, Crystal Growth & Design **8**, 1119 (2008).

[67] J. F. Lutsko, N. González-Segredo, M. A. Durán-Olivencia, D. Maes, A. E. S. Van Driessche, and M. Sleutel, Crystal Growth & Design **14**, 6129 (2014).

[68] J. J. De Yoreo, L. A. Zepeda-Ruiz, R. W. Friddle, S. R. Qiu, L. E. Wasylenki, A. A. Chernov, G. H. Gilmer, and P. M. Dove, Crystal Growth & Design **9**, 5135 (2009).

[69] R. L. Schwoebel and E. J. Shipsey, Journal of Applied Physics **37**, 3682 (1966).

[70] M. Sato and M. Uwaha, Physical Review B **51**, 11172 (1995).

[71] M. Sato, M. Uwaha, and Y. Saito, Physical Review B **62**, 8452 (2000).

[72] M. Sato, M. Uwaha, and Y. Saito, Journal of Crystal Growth **237-239**, 43 (2002).

[73] A. A. Chernov, Journal of Crystal Growth **118**, 333 (1992).

[74] A. A. Chernov, S. R. Coriell, and B. T. Murray, Journal of Crystal Growth **132**, 405 (1993).

[75] S. R. Coriell, B. T. Murray, A. A. Chernov, and G. B. McFadden, Journal of Crystal Growth **169**, 773 (1996).

[76] P. G. Vekilov, H. Lin, and F. Rosenberger, Physical Review E **55**, 3202 (1997).

[77] R. Janssen-van Rosmalen and P. Bennema, Journal of Crystal Growth **42**, 224 (1977).

[78] M. Inaba and M. Sato, Journal of the Physical Society of Japan **80** (2011), 10.1143/jpsj.80.074606.

[79] Y.-I. Kwon, B. Dai, and J. J. Derby, Progress in Crystal Growth and Characterization of Materials **53**, 167 (2007).

[80] K. Seino and A. Oshiyama, Applied Physics Express **13**, 015506 (2020).

[81] K. Seino and A. Oshiyama, Applied Surface Science , 149927 (2021).

[82] M. Camarda, A. L. Magna, and F. La Via, Journal of Computational Physics **227**, 1075 (2007).

[83] G. Gilmer, Journal of Crystal Growth **36**, 15 (1976).

[84] W. Van Enckevort and J. Van Der Eerden, Journal of Crystal Growth **47**, 501 (1979).

[85] T. Cherepanova, J. Van Der Eerden, and P. Bennema, Journal of Crystal Growth **44**, 537 (1978).

[86] Y. Li, X. Chen, and J. Su, Applied Surface Science **371**, 242 (2016).

[87] A. F. Voter, in *Radiation Effects in Solids*, Vol. 235, edited by K. E. Sickafus, E. A. Kotomin, and B. P. Uberuaga (Springer Netherlands, Dordrecht, 2007) pp. 1–23.

[88] M. A. Gibson and J. Bruck, The Journal of Physical Chemistry A **104**, 1876 (2000).

[89] T. P. Schulze, Physical Review E **65**, 036704 (2002).

Chapter 2

Experimental and macroscale CFD investigations on inhomogeneities of step bunching and TSD conversion over a large-sized SiC crystal

2.1 Introduction

In the solution growth of 4H-SiC, the dislocation conversion phenomenon was promising in obtaining dislocation-free single crystals. It has been noted that the interaction of macrosteps and threading dislocations was responsible for the conversion[1]. As is well known, the step structure depends on the polarity (Si face or C face) of the growth surface[2]. On the Si face, TSD conversion frequently occurs because macrosteps easily form[1, 2]. In contrast, due to the absence of macrosteps, TSD conversion is rarely observed on the C face[1]. From the viewpoint of obtaining a smooth surface, the C face is more suitable for long-term growth, and is often used for growth of bulk 4H-SiC crystals[3]. Xiao et al. have reported the formation of macrosteps as well as the conversion of TSDs on the C face during solution growth by the addition of Ti to the solvent[4–6].

The combination of C-face growth and TSD conversion is a possible method for realizing both dislocation-free layers and a smooth surface. In our previous studies using small-size crystals, conversion was always observed over the entire growth surface, which is necessary for obtaining dislocation-free layers. However, it is not certain whether this is also the case for crystals with larger diameters, which

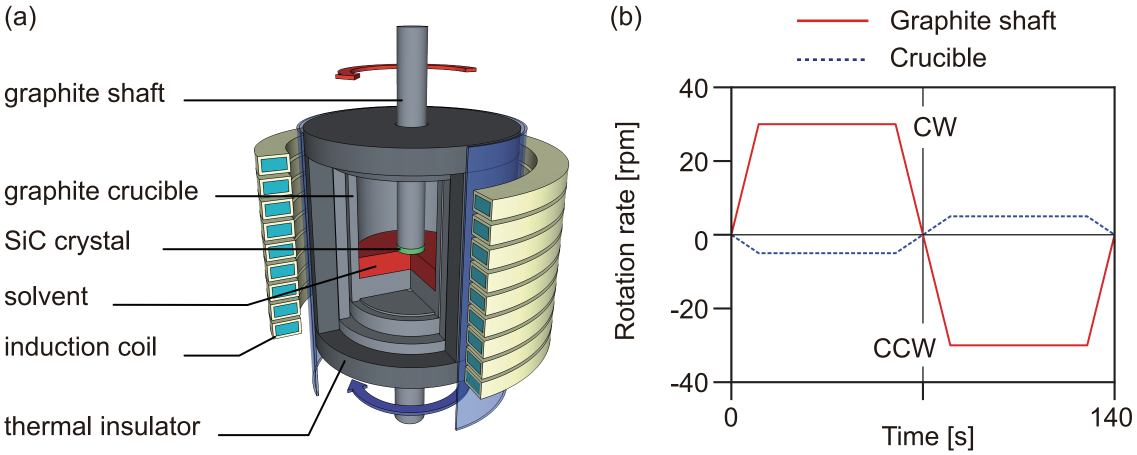

Figure 2.1 Experimental growth conditions: (a) structure of furnace and (b) rotation pattern for seed crystal/crucible. The red line represents the rotation for the seed while the blue line is that for the crucible.

are necessary for commercial SiC wafers. Seki et al have reported the conversion of TSDs during C-face growth from Cr-based solution on a 2-inch wafer. But the occurrence of conversion shows an uncertainty[7]. Therefore, in the present study, a 2-inch 4H-SiC crystal was grown on an off-axis seed crystal by the top-seeded solution growth (TSSG) method. The morphology and the TSD conversion ratio for the grown crystal were experimentally and numerically investigated.

2.2 Experimental and computer simulation

The crystal growth experiment was conducted in an induction-heating furnace (NEV-SC-330, Nisshin-Giken Co., Ltd.). A schematic illustration of the growth setup is shown in figure 2.1(a). High purity silicon (11N) with 5 at% titanium (99.95%) was used as the solvent. A 2-inch C-face 4H-SiC $(000\bar{1})$ substrate with a 1o off-cut towards $[11\bar{2}0]$ was used, which leads to step-flow growth toward the off-cut direction. Crystal growth was carried out at 1940 °C for 3 hours. During growth, accelerated crucible rotation was used to stabilize the carbon supply[8, 9]. The crucible and the seed crystal were counter-rotated in alternating directions. The rotation speeds of the seed crystal and the crucible are shown in figure 2.1(b). After growth, the residual solvent on the crystal was removed using a mixed HF and HNO3 solution (HF: HNO3 = 1:2).

Grazing incidence reflection X-ray topography measurements were carried out at BL8S2 in the Aichi Synchrotron Radiation Center, Japan. The monochromatic

X-ray wavelength was 1.50 Å and the applied g vector was $[11\bar{2}0]$. The incident synchrotron X-ray beam was diffracted by the crystal and recorded using Ilford L4 nuclear emulsion plates. The surface morphology of the grown crystal was observed by differential interference contrast (DIC) microscopy (Olympus, DSX-HRSU). Step heights were measured using 3CCD real colour confocal microscopy (Lasertec, OPTELICS H1200).

A fluid flow analysis with coupled heat and mass transportation was conducted using CGSim (STR Japan Co., Ltd., Version 16.1)[10]. Buoyancy, forced convection, the Marangoni effect and electromagnetic convection were considered. In the simulation, a two-dimensional model with a shape being identical to the cross section of the actual reactor was used. The width of the solution block was 9 cm and the height was 2 cm. A 0.03×0.03 cm rectangular mesh was applied to the solution block. The boundary conditions were chosen to match the experimental situation, with the temperature of the bottom center of the crucible exterior set to 1900 °C. The steady state at the maximum rotation speed was computed, with the rotation rate of the crystal and crucible fixed at 30 and 5 rpm, respectively. The material properties used in the simulation are shown in Table 2.1[11]. Note that the material properties for molten silicon rather than the Si-5at%Ti solvent were used, owing to the lack of exact information on the latter's physical properties. We compared the simulation results obtained using molten silicon with those using the "Si-5at%Ti solvent" setting built into CGSim, but found no significant differences between them. For reproducibility, the simulation results using molten silicon are reported in this study.

2.3 Results and discussion

2.3.1 Inhomogeneity of surface morphology

A 2-inch 4H-SiC crystal was grown to a thickness of 88.4 µm. A DIC micrograph of the grown crystal is shown in figure 2.2(a). A train of steps can be observed over the entire growth surface, with step-flow direction being roughly $[11\bar{2}0]$. The surface can be roughly divided into two regions about the center of the crystal. The upper region is upstream of the step-flow direction, while the lower region is downstream. The surface roughness in the two regions is clearly different. The three areas indicated in figure 2.2(a) were observed by confocal microscopy in order to identify any differences in morphology. Magnified images of the surface morphology in the three areas are shown in figures 2.2(b), 2.2(c) and 2.2(d), together with step profiles. In

Table 2.1 Physical properties used in simulation.

Physical property	Value	Unit
Si melt		
Density	$-0.3701T+3149$	kg m^{-3}
Dynamic viscosity	0.0008	kg m^{-1} s^{-1}
Electric conductivity	1.23	Ω^{-1} m^{-1}
Thermal conductivity	66.5	W m^{-1} K^{-1}
Marangoni coefficient	0.0001	N m^{-1} K^{-1}
Emissivity	0.3	
Heat capacity	372	J kg^{-1} K^{-1}
Graphite		
Electric conductivity	1.22×10^5	Ω^{-1} m^{-1}
Thermal conductivity	40.8	W m^{-1} K^{-1}
Emissivity	0.8	
Graphite felt		
Thermal conductivity	0.48	W m^{-1} K^{-1}
Emissivity	0.8	
Insulation		
Thermal conductivity	0.448	W m^{-1} K^{-1}
Emissivity	0.8	
SiC crystal		
Density	3210	kg m−3
Electric conductivity	5.5991×10^4	Ω^{-1} m^{-1}
Thermal conductivity	410	W m^{-1} K^{-1}
Emissivity	0.8	
Heat capacity	690	J kg^{-1} K^{-1}

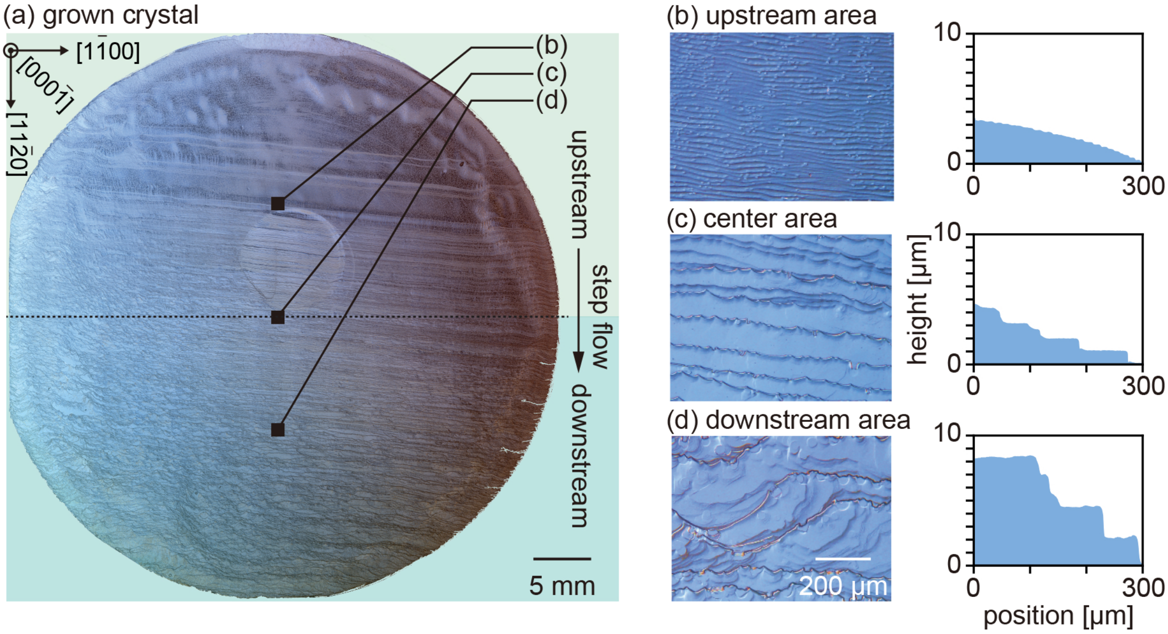

Figure 2.2 (a) DIC image of surface morphology of grown crystal. The black squares indicate the three areas observed in detail. Magnified images of the morphology were taken at the (b) upstream, (c) center and (d) downstream areas. Profiles of step height are shown together with the images.

the upstream area shown in figure 2.2(b), the steps are uniformly distributed and constantly descending, with small terrace widths, indicating a relatively smooth surface. In the center area shown in figure 2.2(c), the number of steps is lower and the terraces are wider. The mean step height is 0.9 μm, indicating the occurrence of step bunching to produce macrosteps. In the downstream area shown in figure 2.2(d), the surface is rough and the height of the macrosteps is 2.0 μm.

2.3.2 Distribution of TSD conversion ratio

To study the distribution of TSD conversion resulting from the non-uniform step height, X-ray topography measurements were carried out. Figure 2.3 shows X-ray topography images of the three areas indicated in figure 2.2. Circular white spots corresponding to TSDs propagating perpendicular to the crystal surface are observed in the upstream area of step flow (indicated by red circles). No TSD conversion is observed in the upstream area. On the other hand, as shown in figures 2.3(b) and 2.3(c), regions of linear contrast are observed in the center and the downstream area (indicated by triangles). Since no morphological irregularities are found at the corresponding positions on the growth surface (figure 2.2), this contrast is associated

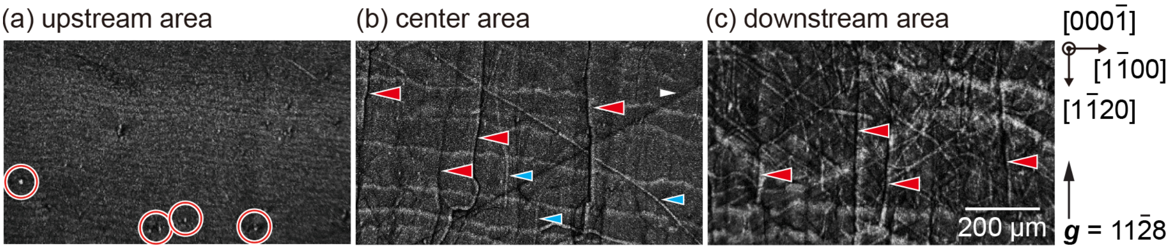
(a) upstream area (b) center area (c) downstream area

Figure 2.3 X-ray topography images taken at (a) upstream area, (b) center and (c) downstream area of grown crystal. (a) and (c) are 10 mm away from the center. The edges of the steps advancing on the growth surface appear as bright horizontal lines. The red circles indicate propagating TSDs and the red arrows indicate converted dislocations. The white triangle indicates a scratch on the nuclear emulsion plate. BPDs are indicated by blue triangles.

with defects on basal planes. Two types of contrast are present. The first type is aligned perpendicular to the step train and extends in the step-flow direction. This consists of dark lines with a bright side (indicated by red triangles). This type of contrast corresponds to defects resulting from the conversion of TSDs and their extension by the steps[6, 12, 13]. The second type represents BPDs (indicated by blue triangles). Since such BPDs are rarely observed in the upstream area, they are considered not to propagate from the seed crystal. Some BPDs are extended towards the step-flow direction, suggesting that they are converted TEDs. Most BPDs have no particular extension direction, indicating that they were not caused by step advance. Also, since the BPD density in the downstream area is much higher than that in the center area, the probable origin of BPDs is surface roughness. In summary, TSD conversion does not take place in the upstream area, but frequently occurs in the center and downstream areas. Therefore, TSD conversion exhibits a spatial distribution on the growth surface.

In order to clarify the change in the conversion behavior along the step-flow direction, step heights and conversion ratios were measured over the entire growth surface. Along the step-flow direction (the $[11\bar{2}0]$ direction), five different regions at an interval of 10 mm were selected for measurement. The third region was the center of the crystal and was assigned a position of 0 mm. The two measurement regions in the upstream area were at -10 and -20 mm, and the two in the downstream area were at 10 and 20 mm. In each measurement region, the step height, number of propagating TSDs and number of converted TSDs were measured at five different points (1 mm^2) at a 5 mm interval. The statistical results are shown in figure 2.4. Figure 2.4(a) shows the average step height while figure 2.4(b) shows the average number of TSDs for each measurement point and the conversion ratio for each region. The conversion ratio is calculated by the following formula,

$$\text{Convertion Ratio} = \frac{\text{Count of converted TSDs}}{\text{Count of converted TSDs} + \text{Count of propagating TSDs}} \quad (2.1)$$

In the upstream area of step flow (20 mm away from the center), the step height was too small to be measured by the confocal microscope and no TSD conversion was evident. The macrostep height and the TSD conversion ratio increase monotonically towards the downstream area of step flow. In the upstream area (-10 mm), the step height is less than 0.2 μmand only a few TSDs are converted. In the center area, the height of the steps increases to 0.9 μmand the conversion ratio increases to almost 80%. The conversion ratio continues to increase with increasing step height, finally reaching 100% in the downstream area (20 mm). It is thought that TSDs are rarely converted in the upstream area due to the absence of macrosteps but are frequently converted in the center and downstream areas due to the existence of macrosteps with sufficient height. It is noteworthy that the conversion ratio rapidly increases between -10 mm and 0 mm, even though the step height increases more slowly. This is considered to be due to earlier conversion in the 0 mm region (and downstream) than in the -10 mm region. Since conversion takes place stochastically during growth,[14] the conversion ratio is proportional to the time from the start of conversion to the end of growth. This is supported by the fact that the apparent length (2.5) of the converted TSDs in the center area is much larger than that in the upstream area. Although this length probably does not correctly reflect the true length of converted defects due to the limited X-ray penetration depth, the increase in relative length still indicates an earlier start for conversion. The positive correlation between the step height and the conversion ratio is again consistent with TSD conversion being strongly related to the macrostep height[15, 1, 14, 16, 2]. Note that the angle between the step facet and the basal plane is another key factor affecting conversion of TSDs[6]. The change in step slope and its influence on the TSD conversion ratio is a subject for future study.

2.3.3 Influence of an outward fluid flow on step bunching inhomogeneity

The distribution of step height can be explained by the relationship between the solution flow and the step-flow direction. Zhu et al. reported the suppression of step

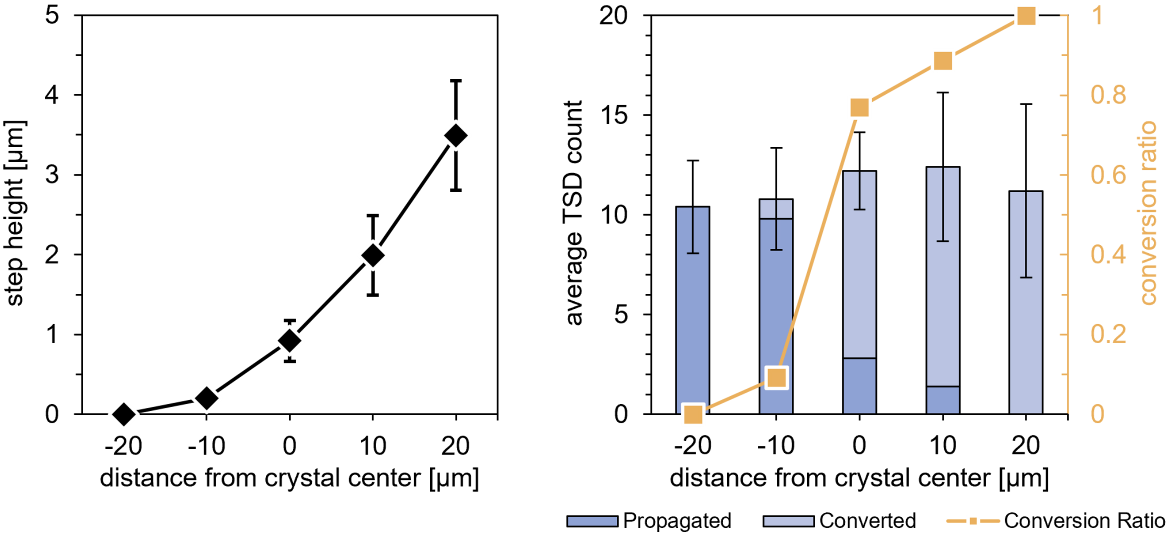

Figure 2.4 Step height and average TSD count measured in five regions. The conversion ratio was calculated from the count of converted and propagated TSDs.

bunching during solution growth on off-axis crystals under anti-parallel solution flow, and the enhancement of step bunching under parallel flow[17]. Figure 2.6(a) shows the calculated temperature and the flow velocity of the solution. Figure 2.6(b) shows a plot of the solution flow velocity in the horizontal direction 0.5 mm below the crystal. The temperature decreases monotonically from the crucible wall to the crystal, guaranteeing growth on the seed crystal. The solution flow appears as an up-flow beneath the crystal. Near the crystal, the solution undergoes an outward flow from the center of the crystal towards the edges. However, the off-axis seed crystal has steps advancing in a single direction. Consequently, in the upstream area of step flow, the solution flow direction is opposite to the step-flow direction (anti-parallel flow). On the other hand, in the downstream area, the solution flow direction is the same as the step-flow direction (parallel flow). As a result, in the upstream area, step bunching is suppressed by the anti-parallel flow, while in the downstream areas step bunching is enhanced by the parallel flow.

2.4 Conclusions

In this study, a 2-inch 4H-SiC crystal was grown on the C face of a 1° off-axis seed crystal by the TSSG method. Step-flow growth in the $[11\bar{2}0]$ direction was observed over the entire growth surface. The step height was found to be non-uniform, resulting in a non-uniform TSD conversion ratio. In the upstream area of step flow,

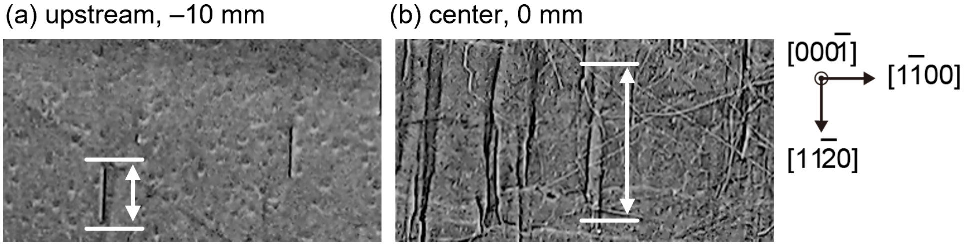
(a) upstream, –10 mm

(b) center, 0 mm

Figure 2.5 Contrast length of converted TSDs. (a) is a contrast at the upstream area (-10 mm) while (b) is one at the center (0 mm).

the step height was small and only a few TSDs were converted. In the center and downstream areas, the macrostep height was large and the TSD conversion ratio was as high as 80%. Both the height and timing of the occurrence of macrosteps leaded to the the great difference in TSD conversion ratio. The results of a fluid simulation revealed that the spatial distribution of step height was caused by the relationship between the solution flow and step-flow directions. Therefore, in order to achieve TSD conversion over the entire growth surface, the fluid flow direction should be considered and controlled.

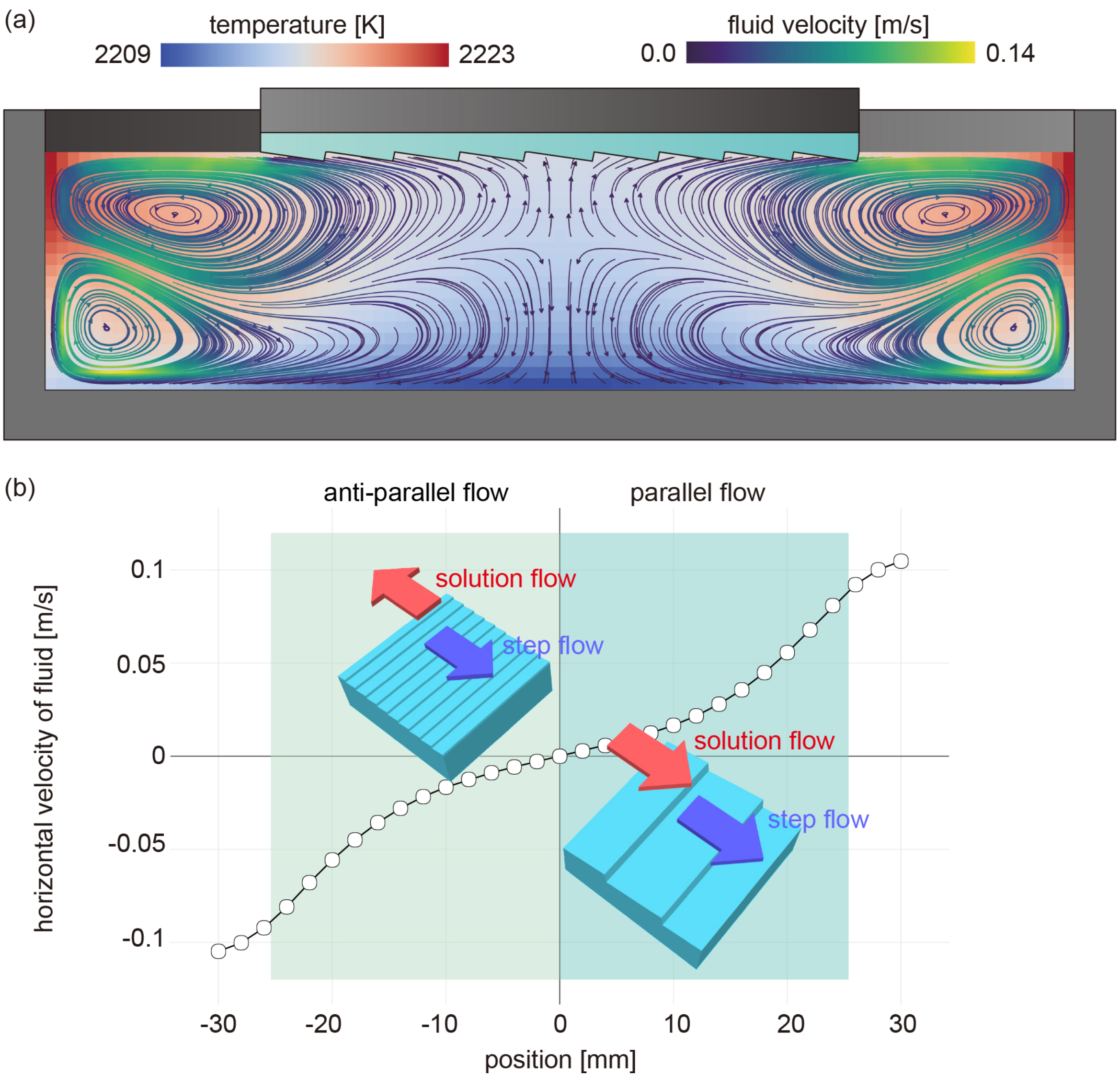

Figure 2.6 (a) Calculated solution flow distribution. The length and direction of the arrows indicate the velocity and direction of flow. (b) Solution velocity in horizontal direction 0.5 mm beneath the crystal.

References

[1] S. Harada, Y. Yamamoto, S. Xiao, M. Tagawa, and T. Ujihara, Materials Science Forum **778-780**, 67 (2014).

[2] Y. Yamamoto, S. Harada, K. Seki, A. Horio, T. Mitsuhashi, and T. Ujihara, Materials Science Forum **740-742**, 15 (2013).

[3] K. Kamei, K. Kusunoki, N. Yashiro, N. Okada, K. Moriguchi, H. Daikoku, M. Kado, H. Suzuki, H. Sakamoto, and T. Bessho, Materials Science Forum **717-720**, 45 (2012).

[4] S. Xiao, N. Hara, S. Harada, K. Murayama, K. Aoyagi, T. Sakai, and T. Ujihara, Materials Science Forum **821-823**, 39 (2015).

[5] Y. Yamamoto, S. Harada, K. Seki, A. Horio, T. Mitsuhashi, D. Koike, M. Tagawa, and T. Ujihara, Applied Physics Express **7**, 065501 (2014).

[6] S. Xiao, S. Harada, K. Murayama, M. Tagawa, and T. Ujihara, Crystal Growth & Design **16**, 6436 (2016).

[7] K. Seki, K. Kusunoki, Y. Kishida, H. Kaido, K. Moriguchi, M. Kado, H. Daikoku, T. Shirai, M. Akita, A. Seki, H. Saito, S. Harada, and T. Ujihara, Materials Science Forum **924**, 39 (2018).

[8] H. J. Scheel, Journal of Crystal Growth **13-14**, 560 (1972).

[9] K. Kusunoki, K. Kamei, N. Okada, N. Yashiro, A. Yauchi, T. Ujihara, and K. Nakajima, Materials Science Forum **527-529**, 119 (2006).

[10] "CGSim package for analysis and optimization of Cz, LEC, VCz, and Bridgman growth of semiconductor and semitransparent crystals," https://www.str-soft.co.jp/product/cgsim.html (2021).

[11] Y. Mukaiyama, M. Iizuka, A. Vorob'ev, and V. Kalaev, Journal of Crystal Growth **475**, 178 (2017).

[12] H. Tsuchida, I. Kamata, and M. Nagano, Journal of Crystal Growth **306**, 254 (2007).

[13] Y. Yamamoto, S. Harada, K. Seki, A. Horio, T. Mitsuhashi, and T. Ujihara, Applied Physics Express **5** (2012), 10.1143/apex.5.115501.

[14] S. Harada, Y. Yamamoto, K. Seki, A. Horio, T. Mitsuhashi, M. Tagawa, and T. Ujihara, APL Materials **1**, 022109 (2013).

[15] S. Harada, Y. Yamamoto, K. Seki, A. Horio, M. Tagawa, and T. Ujihara, Acta Materialia **81**, 284 (2014).

[16] T. Ujihara, S. Kozawa, K. Seki, Alexander, Y. Yamamoto, and S. Harada, Materials Science Forum **717-720**, 351 (2012).

[17] C. Zhu, S. Harada, K. Seki, H. Zhang, H. Niinomi, M. Tagawa, and T. Ujihara, Crystal Growth & Design **13**, 3691 (2013).

Chapter 3

A mesoscale CFD investigation on solution-property-induced step bunching and a criterion for designing solvent aiming at stable growth

3.1 Introduction

A general understanding of the step bunching mechanism is essential for solvent design. However, it remains challenging because the mechanism includes an interplay between mass transport and surface kinetics. This study constructed a computational fluid dynamics (CFD) model coupling the physical phenomena at the growth interface and focused on the role of solute transport and step kinetics in step growth rate and bunching behavior. First, the effect of fluid velocity on step bunching size is quantitatively studied and compared with the experimental results shown in the last chapter. Then the effect of solvent physical properties representing mass transport and step kinetics on step bunching is investigated. We come to a similar conclusion as the Mullins-Sekerka instability but address the kinetic perspective of step bunching.

3.2 Computer simulations

In this study, a fluid dynamics simulation coupling with surface kinetics is carried out to investigate how physical properties affect surface stability. This model is inspired by the similar works done previous researchers.[1–3] Only we combined the features of 1) multiple steps in one grid [1] and 2) calculate step velocities post solute concentration[2, 3] This model allows us to simulate the behavior of plenty of steps without increasing mesh density. Values of the step kinetic coefficient $\mathcal{K}_{\mathrm{st}}$ and diffusion coefficient $\mathcal{D}$ are changed, and step velocities and positions are observed to quantify growth rate and bunching behavior.

The diagrammatic illustration of the model is shown in Figure 3.1. The model contains a solution part and a surface part. The solution part describes the mass transport and absorption of growth units in a laminar boundary layer near the crystal. The upper boundary of the solution part ($y = y_{\mathrm{max}}$) indicates the interface between the laminar boundary layer and the imaginary bulk solution. While the surface part, located at the bottom boundary of the solution part, mimics a vicinal surface where aligned steps train advancing. As shown in figure. 3.1 (b, c), the surface part are divided into grids (the X_is). The step motion is independent of the grids. However, when a step enters one mesh, it will maintain the same velocity as the other steps in this mesh. (figure. 3.1 (d))

Simulations are carried out on a 0.75° tilted vicinal substrate. Thus the surface is intrinsically stepped. Figure 3.2 shows the diagram of the side view of a stepped surface. The line graph indicates the surface with step trains perfectly equidistant arranged, with the n-th step's "perfect position" being $n\delta_0$. The steps advance towards the x-direction in v_{st}. To introduce an instability, we set steps deviating from the perfect positions by $\delta_x \cos(kn\delta_0)$ in the initial simulation configuration, indicated by the filled graph. This initial configuration is the same ones in step bunching analyses utilizing the perturbation theory[4–7]. Since it is difficult to affirm whether an elementary step is bunched, the "local slope" is measured instead in this study. On a smooth surface, each step has the same local slope of $p_0 = \tan\theta_0$, where θ_0 is usually mentioned as the "off-angle" in experimental studies. On an undulated surface, the local slope varies. For a step in a step bunching (indicated as 1 in figure. 3.2) it is $p_1 = \tan\theta_1$ while for a step out of a bunching (indicated as 2) it is $p_2 = \tan\theta_2$, where $\theta_1 > \theta_2$ are the angles between the tangent line of surface profile passing the step and the horizontal line. We can quantitatively tell how dense the step is bunched by measuring the elementary step's local slopes.

Note that we did not explicitly consider the step height in the calculation of mass transport because the step height is minor compared with the length scale of the solution. [1] However, since the top of a bunch protrudes to the solution, a bunch-top step should be less affected than a bunch-bottom step by the solute

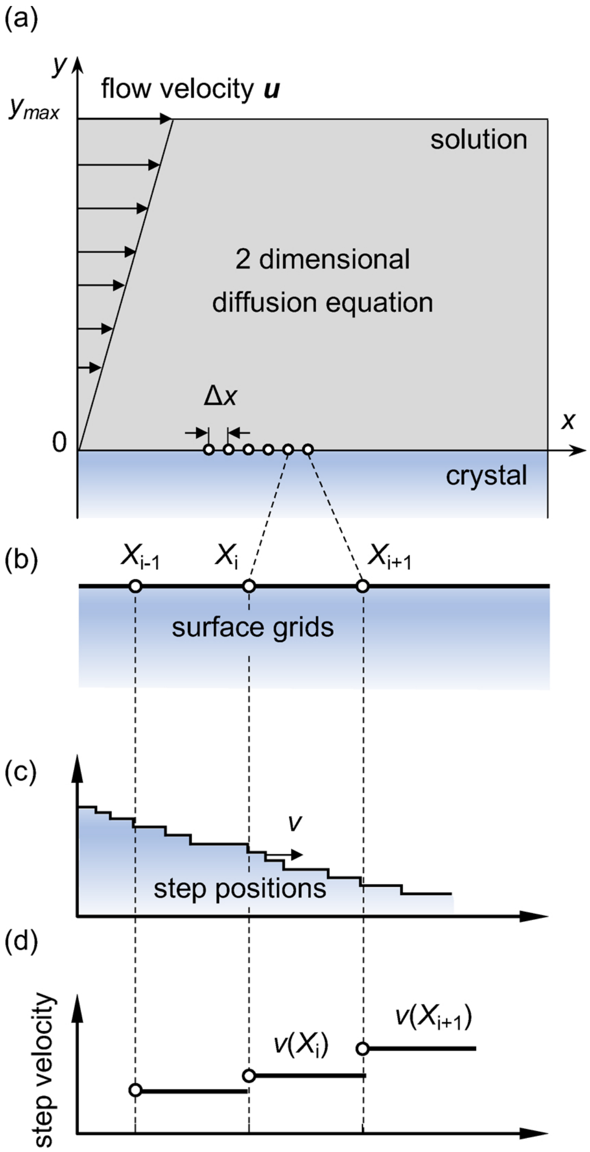

Figure 3.1 The schematic diagram of the model. (a)shows the components of solution and crystal surface. (b)shows the diagram of grids on the surface. (c)is a schematic diagram of the actual stepped vicinal surface corresponding to the configuration of crystal surface in the simulation, and (d)shows the calculated step velocities in each grid.

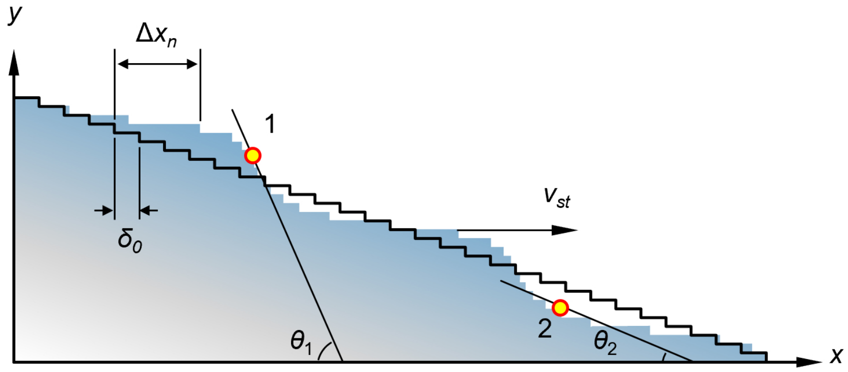

Figure 3.2 The schematic diagram of the vicinal surface. Evenly spaced step trains are represented by a line graph, while step trains deviating from evenly spaced positions by $\delta_x \cos(kn\delta_0)$ are represented as a filled graph. The deviation of step position leads to steps aggregating and separating periodically, forming a periodically step-bunching morphology. The numbers indicate regions with different step densities.

depression caused by the step bunch. Although this difference may be minor, we consider it significant at the initial stage of the instability. One will find that some step bunches are artificially created to introduce instability, and the step bunches have symmetrical profiles. One will also find the step velocity related to the profile. That means step movements in the two sides of a bunch, that is, entering and leaving the bunch, corresponding to bunching and de-bunching, are supposed to be symmetrical, as well. The above-mentioned minor difference between the top and bottom steps broke the symmetry and led to instability. Before de-bunching, a bottom step must move in the mesh containing the bunch at a relatively small velocity due to the depression caused by the bunch. On the other hand, a step moves faster before it enters the mesh, and once it crosses the mesh border, it gets bunched. That leads to faster bunching than de-bunching in the simulation, yet the bunch profile is symmetrical.

3.2.1 Model formulation

The solute transport in the solution volume is described by the convection-diffusion equation of the form

$$\frac{\partial c}{\partial t} + \mathbf{v} \cdot \nabla c = \mathcal{D} \nabla^2 c. \tag{3.1}$$

The boundary condition at top of the fluid domain where $y = \delta_c$, is set as

$$c = c_\infty, \tag{3.2}$$

where c_∞ is the bulk concentration in solution. The horizontal boundaries are set to be periodical. According to the mass conservation, the boundary condition at the solution-solid interface is formulated for each boundary mesh as:

$$N\overline{v_{\mathrm{st}}}\rho^{\mathrm{S}}h = \mathcal{D}\frac{\partial \rho^{\mathrm{L}}}{\partial y}\bigg|_{y=0}\Delta x, \tag{3.3}$$

Where N is the number of steps in a mesh, ρ^{S} and ρ^{L} are the solutal density in the solid and liquid phase, respectively. Δx is the mesh size in x-direction, $\overline{v_{\mathrm{st}}}$ is the mean velocity of the steps in the mesh, and h is the step height. In grids with zero steps in, the boundary condition eq. 3.3 becomes a simple Neumann boundary condition

$$\frac{dc}{dy} \equiv 0. \tag{3.4}$$

A step's velocity can to be calculated with the concentration near the step, c_{st}, with [8]

$$v_{\mathrm{st}} = \mathcal{K}_{\mathrm{st}} v_{\mathrm{c}}(c_{\mathrm{st}} - c_{\mathrm{eq}}), \tag{3.5}$$

where $\mathcal{K}_{\mathrm{st}}$ is the step kinetic coefficient and v_{c} is the volume of growth unit, which is considered to be 1/4 of the 4H-SiC primitive cell. Combine the molar concentration and the volume of growth unit then we get

$$v_{\mathrm{st}} = \mathcal{K}_{\mathrm{st}}(c^*_{\mathrm{st}} - c^*_{\mathrm{eq}}), \tag{3.6}$$

where $c^* = c \times v_{\mathrm{c}}$. And since $\rho^{\mathrm{L}}/\rho^{\mathrm{S}}|_{y=0} = c^*_{\mathrm{st}}$, the boundary condition can be written as

$$Nh\mathcal{K}_{\mathrm{st}}(c^*_{\mathrm{st}} - c^*_{\mathrm{eq}}) = \mathcal{D}\frac{\partial c^*_{\mathrm{st}}}{\partial y}\Delta x. \tag{3.7}$$

3.2.2 Determination of physical parameters

The diffusion coefficient of carbon in pure silicon melt can be calculated in unit $\mu\mathrm{m}^2/\mathrm{s}$ with [9]

$$\mathcal{D} = 7.55 \times 10^8 \exp(\frac{-9150}{1.9856T}). \tag{3.8}$$

Since the solubility of carbon in pure silicon melt is small, consider the density of carbon's silicon solution being the same as pure silicon melt with

$$\rho = 2.54 - 1.59 \times 10^{-4}(T - T_{\mathrm{m}}) - 1.15 \times 10^{-7}(T - T_{\mathrm{m}})^2, \tag{3.9}$$

where T is the temperature and T_{m} is the melting point of silicon. The unit is $\mathrm{g/cm^3}$. The carbon solubility in pure silicon melt can be calculated in mole fraction with [10]

$$a\% = \exp(\frac{-2.97 \times 10^4}{T} + 7.95). \tag{3.10}$$

Converted in weight fraction

$$w\% = \frac{1}{1 + \frac{M_{\mathrm{Si}}}{M_{\mathrm{C}}}(\frac{1}{a\%} - 1)} \tag{3.11}$$

and converted to molar concentration in $\mathrm{mole/\mu m^3}$

$$c = \rho \frac{w\%}{M_{\mathrm{C}}} N_{\mathrm{A}} \times 10^{-12}. \tag{3.12}$$

where M is the molecular weight, N_{A} is the Avogadro number. While the normalized concentration c^* appeared in this study is the number of solutal atoms in every primitive cell

$$c^* = c \times v_{\mathrm{c}}, \tag{3.13}$$

where $v_{\mathrm{c}} = 2.0554 \times 10^{-11}\ \mathrm{\mu m^3}$ is the volume of a primitive cell of 4H-SiC.

The parameters used in simulations presented in each section are listed in table 3.1.

3.3 Results and discussion

3.3.1 Effect of fluid flow velocity on step bunching size

Figure 3.3 shows the surface profiles grown for 150 second, with different fluid flow conditions, as simulation results. The flow velocity is acquired from the numerical simulation result shown in the last chapter. Under an anti-parallel flow, the step bunches become smaller in height (figure 3.3 (b)). Figure 3.3 (d) shows that among the initial bunches, some step bunches become much higher under a parallel flow. When there is no fluid flow, as indicated in figure 3.3 (c), the step bunching was enhanced during growth. However, the step bunching shows no significant difference compared with the initial surface.

To quantitatively determine how much step bunching is changed by fluid flow, we use the surface height's statistic root-mean-square (RMS) to measure the surface

Table 3.1 Parameters used in simulation shown in each section.

Physical property	Symbol	3.3.1	3.3.2	3.3.3	Unit
Boundary condition					
Step height	h	2.51	2.51	2.51	Å
Off-angle	θ	1.0	0.75	-	°
Equilibrium concentration	c^*_{eq}	0.00188	0.00188	1.0	
Bulk concentration	c^*_{∞}	0.00476	0.00476	2.0	
Geometry					
x-direction length	L_x	40	50	50	μm
y-direction length	L_y	300	300	50	μm
Initial Configuration					
Pertubation wave number	k_x	π	π	-	μm^{-1}
Pertubation amptitude	δ_x	0.1	0.1	-	μm
Dynamics					
Temperature	T	2073	2073	2073	K
Diffusion coefficient	$\mathcal{D}$	8180	8180	10^4 & 10^8	$\mu\text{m}^2/\text{s}$
Step kinetic coefficient	$\mathcal{K}_{\text{st}}$	10^4	$2 \times 10^{0-7}$	10^4 & 10^8	μm/s

roughness. It can be written as

$$\Delta h_{\text{RMS}} = \sqrt{\frac{1}{n}(\Delta h_1)^2 + (\Delta h_2)^2 + \ldots + (\Delta h_n)^2}, \tag{3.14}$$

where Δh_i is the difference between the i-th interpolated value on the surface height profile and the mean surface height. Figure. 3.6(b) diagramticly shows the measurement of Δh_i and the mean surface height. Figure 3.4 shows the relative RMS under different flow conditions. Under an anti-parallel flow and a parallel flow, the surface roughness shows obvious change from the initial state, consistent with the experimental results. However, when there is no flow, the surface roughness shows little difference from the initial state. The status of step bunching without flow influence can be viewed as the “intrinsic” step bunching. The following sections intend to investigate what is affecting this intrinsic step bunching.

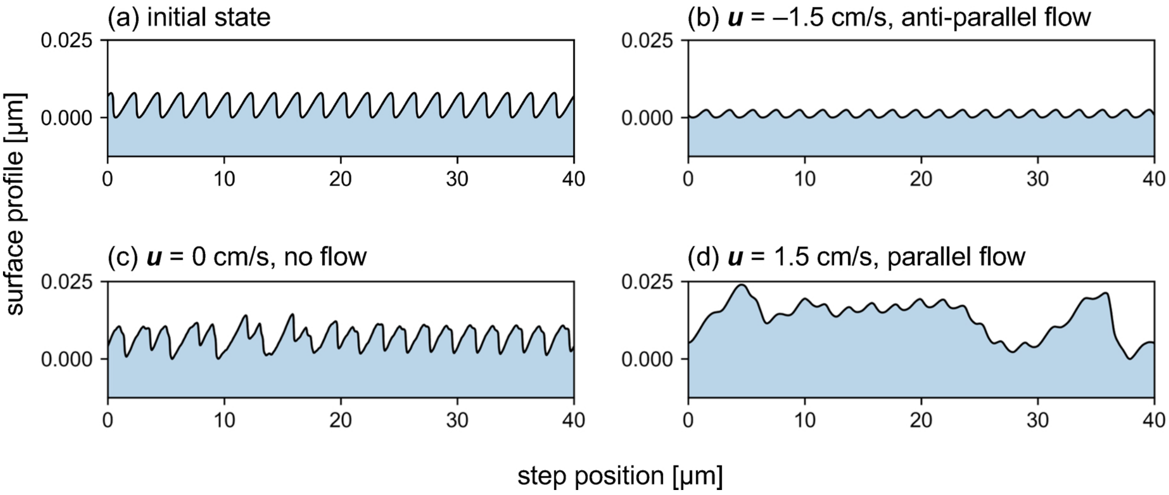

Figure 3.3 Surface profiles of (a) a crystal before growth and grown crystals with (b) a 1.5 cm/s anti-parallel fluid flow, (c) no fluid flow and (d) a 1.5 cm/s parallel fluid flow. When plotting the profiles, surfaces are tilted counterclockwise by the off-angle. The undulating is bunches of steps.

3.3.2 Effect of $\mathcal{K}_{\mathrm{st}}$

Primarily, the step velocity is directly determined by the step kinetics, which is characterized by the step kinetic coefficient. It is defined as

$$\mathcal{K}_{\mathrm{st}} = \nu a_{\mathrm{st}}(\frac{a_{\mathrm{k}}}{\delta_{\mathrm{k}}})\exp(-\frac{\Delta U}{k_{\mathrm{B}}T}), \tag{3.15}$$

where ν is the attempt frequency, a_{st} is the unit advancing distance of a step, a_{k} and δ_{k} are the length of a single kink site and the average distance between two neighbouring kink sites, respectively. ΔU is the solvation barrier, k_{B} is the Boltzmann constant and T is the temperature. In the pre-exponential factor, δ_{k}, the average distance between kinks, can be written as $\delta_{\mathrm{k}} = a[1 + 1/2\exp(\omega/k_{\mathrm{B}}T)]$, where ω is the energy necessary for creation of a kink,[11] which is actually the interface energy of the crystal-solution interface in our case. Thus we consider the step kinetic coefficient reflecting an important aspect of the solution properties.

One of the major obstacles to fully linking experimentally observed step bunching behaviors to additive elements is our lack of knowledge about step kinetics. Onuma *et al*. indicated that the transition from step bunching to stable growth by adding aluminum is due to surface kinetics rather than other solution properties like diffusivity or carbon solubility. Although the direct evidence for step kinetics being modified by aluminum is not able to be obtained, they convincingly conducted

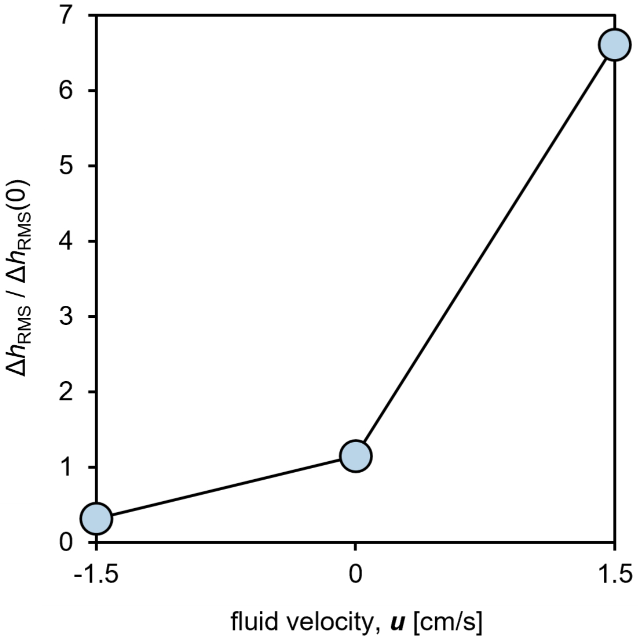

Figure 3.4 Dependence of surface roughness on fluid flow velocity.

the conclusion through two facts, with the addition of 5% aluminum, the thermal calculation showing that solvent properties change minorly and the step velocities showing a transition from a step height dependant mode to a step height independent mode. [12] However, a direct and quantitative study is still necessary to reveal the influence of kinetics on step bunching. Experimentally determining the step kinetic coefficient (as the fraction of step velocity and supersaturation) requires an *in-situ* measurement to elementary steps, which is very difficult, if not impossible, in the case of solution growth of SiC for the high growth temperature. Therefore, in this study, we carried out a series of simulations with varied $\mathcal{K}_{\mathrm{st}}$ values to reveal its influence on step bunching behavior.

The dependence of $\mathcal{K}_{\mathrm{st}}$ on the kink-creation work, the solvation energy and the temperature is shown in figure 3.5, according to equation 3.15, by assuming $\nu_0 = 10^{12}\ \mathrm{s}^{-1}$ and $a_{\mathrm{st}} = 3.0370\text{Å}$. One can find that with these parameters varying, the value of $\mathcal{K}_{\mathrm{st}}$ can vary broadly. At the same time, these parameters can easily vary in the range. Furthermore, the maximum of $\mathcal{K}_{\mathrm{st}}$ can be estimated by assuming that the kink density on the step is a unit and the solvation barrier is zero. That leads to a maximum value $\mathcal{K}_{\mathrm{st}} = 3 \times 10^{8} \mu\mathrm{m/s}$.

Figure 3.6 shows (a) the initial and (b) the as-grown surface morphology. Note that this is an enlarged portion of the whole surface with a total length of 40 µm.

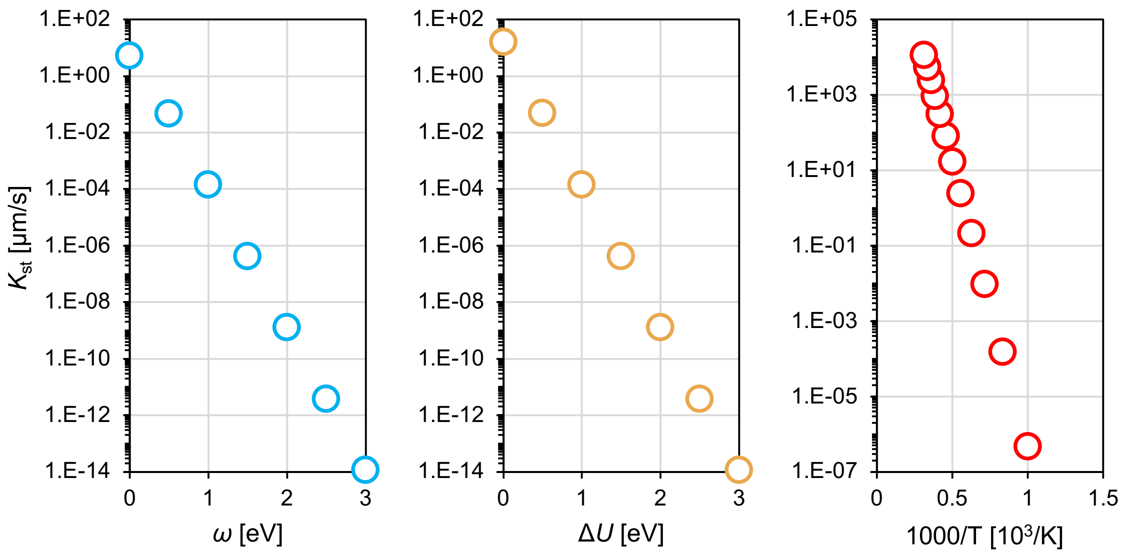

Figure 3.5 Dependence of $\mathcal{K}_{\rm st}$ on (a) the kink creation work, (b) the solvation energy and (c) the temperature.

Compared with the initial morphology, the step bunchings on the as-grown surface are higher and steeper.

The changes of surface roughnesses over time are measured for two crystals with step kinetic coefficients varying from 2 µm/s to 2×10^7 µm/s. We chose such a wide range because the $\mathcal{K}_{\rm st}$ can vary broadly when the temperature, kink creation work, or the solvation barrier are changed. The results $\mathcal{K}_{\rm st} = 2{\times}10^7$ µm/s, $\mathcal{K}_{\rm st} = 10^6$µm/s, and 2×10^3 µm/s are shown in Figure 3.7. The rest results show no significant difference from the results obtained with $\mathcal{K}_{\rm st} = 10^3$µm/s. Also, the results of $\mathcal{K}_{\rm st} = 10^6$µm/s can be viewed as a transition state between the other two results. For the clarity of our discussion, only the two critical results are displayed. The growth time at maximum is 500 seconds. Because no artificial solid-on-solid (SOS) restriction is applied in this model and the steps in the case of $\mathcal{K}_{\rm st} = 2 \times 10^7$ µm/s starts to overlap after growing for over 500s. (Although an SOS restriction is usually preferred for the advantage of preventing steps from overlapping, we did not include the restriction due to a consideration of the law of mass conservation.) The surface roughness remains constant for the crystal with a small value of $\mathcal{K}_{\rm st} = 2 \times 10^3$ µm/s, indicating little further step bunching. While for the crystal with a large value of $\mathcal{K}_{\rm st} = 2 \times 10^7$ µm/s, the surface roughness increases exponentially with a short-period oscillation. The reason for the exponential growth will be discussed in the next section. The oscillation and increase of surface roughness imply how steps bunch. Once step

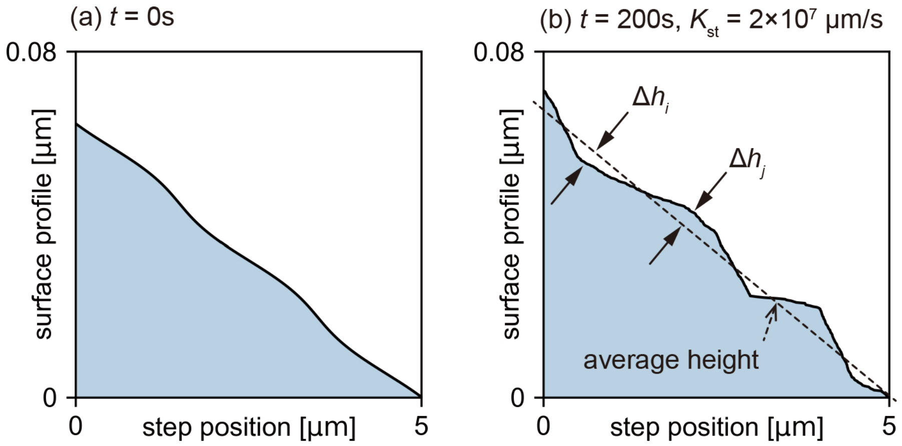

Figure 3.6 The enlarged height profile of the crystal surface (a)before and (b)after growth. The growth period is 500 seconds.

bunches are formed, the elementary steps are not constantly fixed in the current bunches. Instead, the elementary steps keep leaving their current bunches from the front and entering the next bunches from behind. This results in two kinds of temporary states, 1) there are more elementary steps leaving than entering, and the step bunches dissipate, 2) there are more entering than leaving, and the step bunches grow. The alternating of the two temporary states leads to the oscillation in surface roughness. If the entering of elementary steps to bunches is faster than leaving, the probability of temporary state 1) thus is higher than 2). Therefore, the step bunches are enhanced, and the surface roughness increase. That is the exact reason why would a large value of kinetic coefficient results in step bunching.

To verify the mechanism of $\mathcal{K}_{st}$ affecting step bunching behavior, the step velocities v_{st} against the local slopes p are plotted in Figure 3.8. Note that the local slope p is replaced with step the local density

$$p_{i} = \frac{N_{i}}{\Delta x}, \tag{3.16}$$

where the subscript i refers to the i-th surface grid and N is the number of steps in the surface grid. According to the mechanism of step bunching, a step bunch increases its height because the steps in it have different velocities from the other steps. As shown in figure 3.8(a), despite the variance among local slopes, step velocities are the same and remain constant over the whole growth duration. Bear in mind that the step's local slope indicates how dense the step is bunched. The constant and slope-independent velocities reveal that the velocity should be the same with small $\mathcal{K}_{st}$, no matter whether a step is in a bunch or on the terrace. On the other hand,

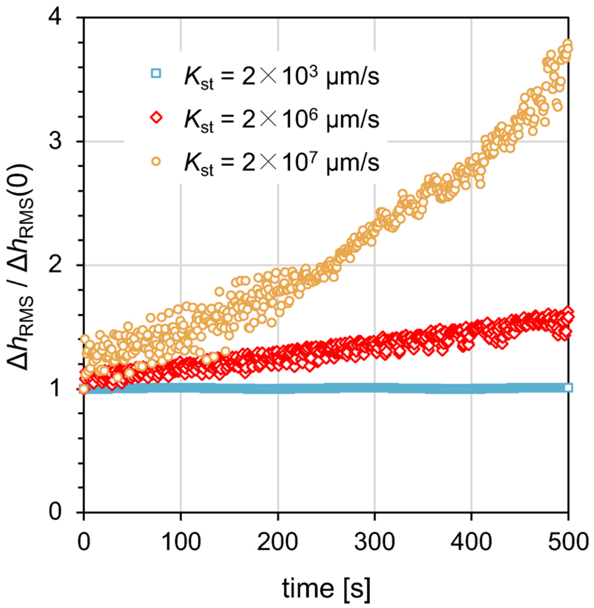

Figure 3.7 Change of surface roughnesses over growth time. Note that the root mean square of height profile is normalized by its initial value for clear.

as shown in figure 3.8(b), step velocity shows an apparent inverse proportional relationship with the local slope, indicating that a step in a bunch slows down itself and will be caught by other steps coming from behind. Thus, the bunch grows larger. It is also noteworthy that the distribution of scatters changes over time in figure 3.8(b). At the beginning stage, the variances of the step velocities and the local slopes are minor. But during growth, both the two variances increase. The synchronous increases in variances indicate the mechanism of a surface losing its stability: Since the step velocities reversely depend on the local slopes, elementary steps collide ahead into bunches, resulting in higher step densities in bunches and lower on terraces. That results in step movements even slower in bunches and faster on terraces. Furthermore, again the slower moving bunches catch more steps from terraces. Step bunches intensify step bunching. That is why the surface roughness increases exponentially (shown in figure. 3.7).

3.3.3 Effect of $\mathcal{D}$

An enormous value for step kinetic coefficient, $\mathcal{K}_{st}$, enhances step bunching behavior. On the other hand, the diffusion coefficients are revealed to affect step bunching behavior in a reversed manner, as shown in Figure 3.9. Figure. 3.9 shows the solutal concentration as a result of simulations using a pair of large and small values of both

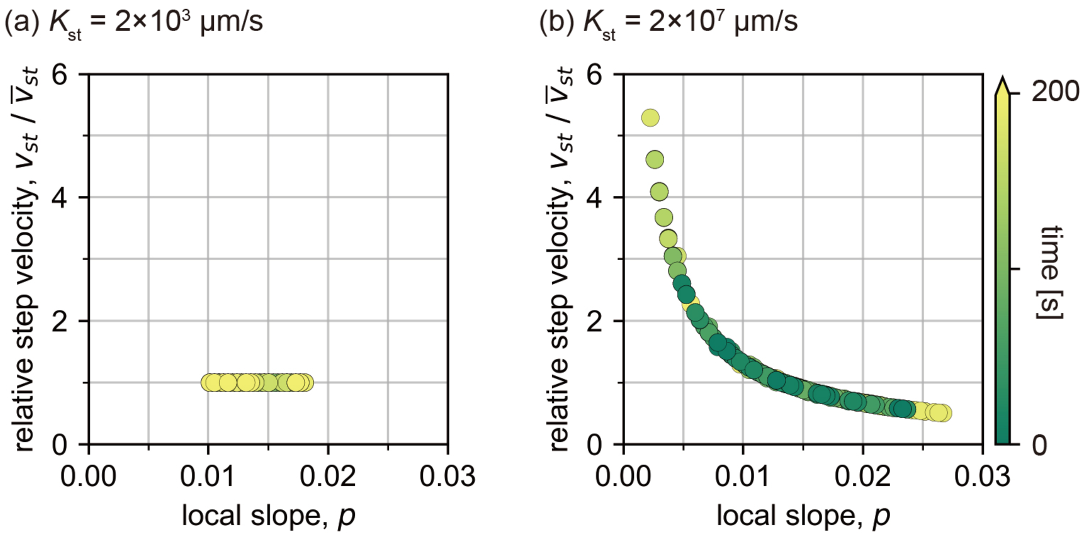

Figure 3.8 Scatter plots of step velocities against the local slopes over the growth time of crystal whose step kinetic coefficient is (a)2×10^3 μm/s (b)2×10^7 μm/s. The scatters colors indicate the time passed since the growth started.

diffusion coefficient and step kinetic coefficient. The boundary condition is the same as the simulations carried out in the last section, but the crystal-solution boundary now has only one macrostep aggregated at the center of the surface (where the darkest part is located in the colormap in figure. 3.9) instead of steps distributed on the whole surface with different densities. We also calculated the relative step velocities with the solutal concentration on the crystal-solution boundary c^*_{st} with $v_{\mathrm{st}} = \mathcal{K}_{\mathrm{st}}(c^*_{\mathrm{st}} - c^*_{\mathrm{eq}})$. In the case of figure 3.9(a) small $\mathcal{D}$ but large $\mathcal{K}_{\mathrm{st}}$, as analyzed in the last section, the solute is consumed by steps rapidly and can not be supplied in time by diffusion. Therefore, a low-concentration regime appeared around the macrostep, resulting in steps in the macrostep decelerated to a shallow level compared with the velocity of independent elementary step v^{∞}_{st} (eq. 3.17). In the two cases (b) large $\mathcal{D}$ and large $\mathcal{K}_{\mathrm{st}}$ (c) small $\mathcal{D}$ and small $\mathcal{K}_{\mathrm{st}}$, the solute consumption can be partially supplied by diffusion. Thus the solute is less depleted around the macrostep. We also found that the relative velocity is the same in the two cases. In contrast, in the last case (d) large $\mathcal{D}$ but small $\mathcal{K}_{\mathrm{st}}$, the solute consumption is entirely supplied by diffusion, and the solutal concentration difference is almost smoothed out, and the steps in macrosteps are no longer decelerated, which corresponds to the situation in Figure 3.8 (b).

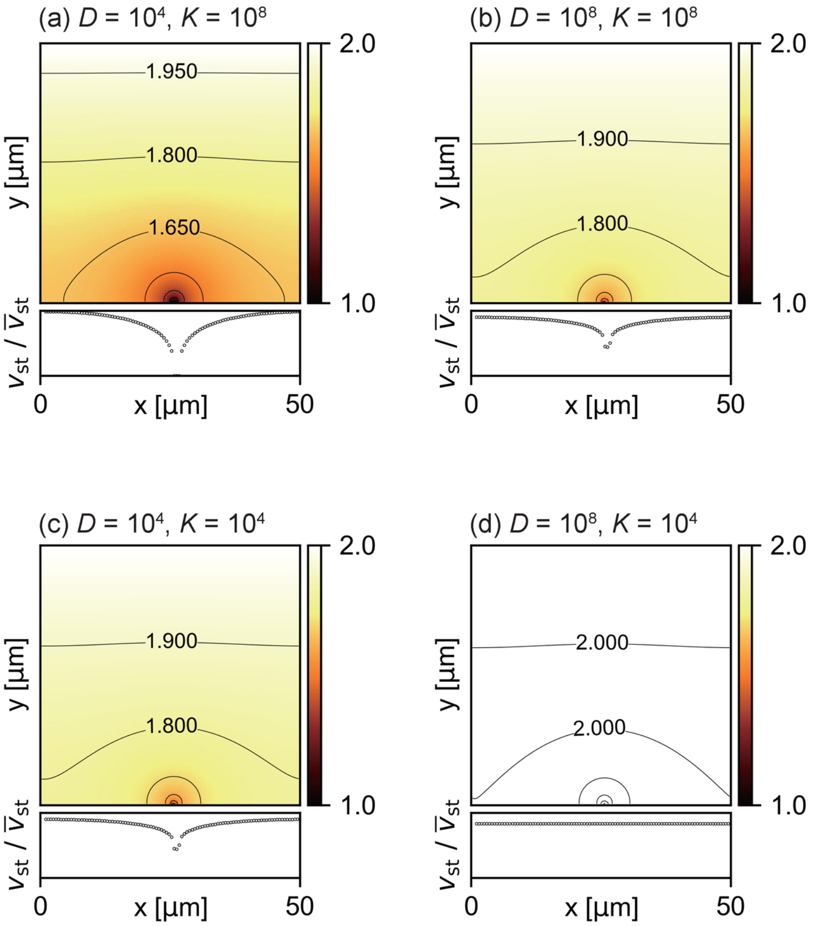

Figure 3.9 Solutal concentration and the relative step velocities simulated by CFD model with a macrostep at the center of the lower boundary. Only the diffusion coefficient and the step kinetic coefficient varied. The units for $\mathcal{D}$ is $\mu m^2/s$ and for $\mathcal{K}_{st}$ is $\mu m/s$.

3.3.4 Nondimensional Analysis of Growth Phase Map

According to Chernov,[13] in solution growth, step velocity of equally spaced steps on a vicinal surface can be written as

$$v_{st}^{\infty} = \frac{\mathcal{K}_{st} c_{eq} v_c \sigma}{1 + \frac{a\mathcal{K}_{st}}{\pi \mathcal{D}} \ln(\frac{x_0}{a} \sinh(\frac{\pi \delta}{x_0}))}, \tag{3.17}$$

where σ is the supersaturation degree at the maximum of boundary layer, a is the height of a elementary step, x_0 is the distance between two neighboring steps, δ is the thickness of boundary layer.

In most cases of solution growth, the boundary layer thickness is much larger than the step distance,

$$\pi\delta \gg x_0.$$

Therefore, the step velocity can be approximated as

$$v_{\mathrm{st}} \approx \frac{\mathcal{K}_{\mathrm{st}} c_{\mathrm{eq}} v_{\mathrm{c}} \sigma}{1 + \dfrac{p\mathcal{K}_{\mathrm{st}}\delta}{\mathcal{D}}}, \tag{3.18}$$

where $p = a/x_0$.

While the reversed influences of step kinetics and diffusion have been elucidated in the last sections, according to equation 3.18, analysis of the balance between step kinetics and solute diffusion needs to be developed to provide a holistic picture. In this regard, we define a non-dimensional Damköhler number (D_{a}) for step-flow growth from solution as the ratio of reaction rate to diffusion rate and classify the observed regimes as a function of this number

$$D_{\mathrm{a}} = \frac{p\mathcal{K}_{\mathrm{st}}\delta}{\mathcal{D}}, \tag{3.19}$$

where $p\mathcal{K}_{\mathrm{st}}$ is the "surface kinetic coefficient" reperesenting the incorporation rate of solute on the growth surface, δ is the characteristic length thus $\mathcal{D}/\delta$ is the characteristic diffusion velocity. Similar nondimensional numbers are defined and used as criteria of transition between stable growth and dendritic growth[14] or as an explanation of the growth rate profile in epitaxy of GaAs by MOCVD method[15]. $D_{\mathrm{a}} \gg 1$ implies that the incorporation of growth units occurs mush faster than diffusion in solution. This leads to the diffusion limited growth regime since the solute consumed will not be supplemented in time. The step velocity can be approximated to

$$v_{\mathrm{st}} \approx \frac{\mathcal{D} c_{\mathrm{eq}} v_{\mathrm{c}} \sigma}{p\delta}. \tag{3.20}$$

It makes sense since the steps will have to slow down to compensate for the decrease in solute concentration, which is more drastic near step bunching. For $D_{\mathrm{a}} \ll 1$, the growth enters a kinetic limited regime, in which any consumption of solute will be supplemented immediately. Thus all steps will maintain the same velocity no matter where it is. The step velocity is then

$$v_{\mathrm{st}} \approx \mathcal{K}_{\mathrm{st}} c_{\mathrm{eq}} v_{\mathrm{c}} \sigma. \tag{3.21}$$

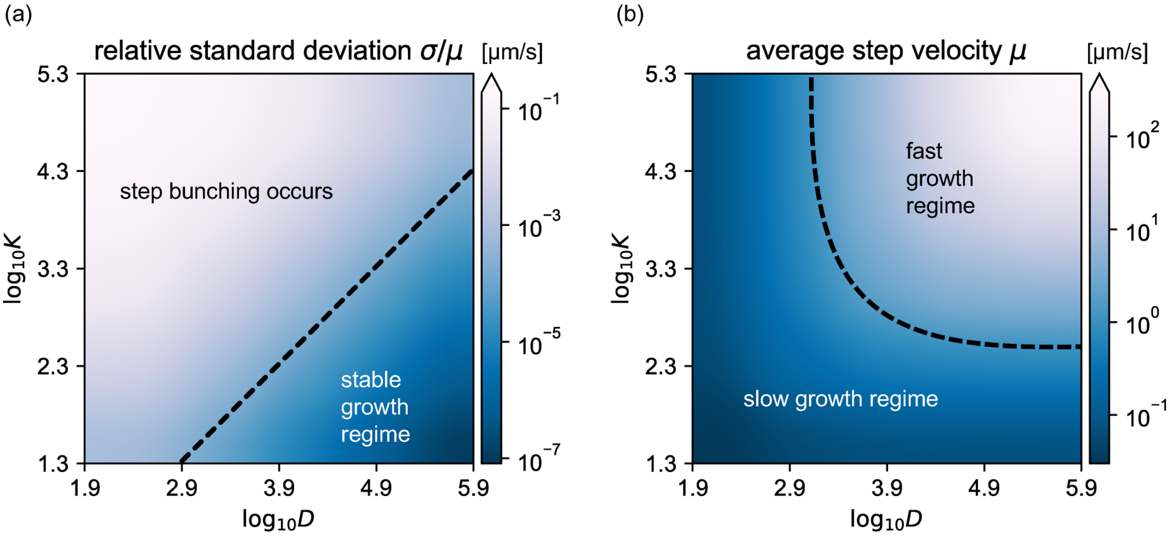

Figure 3.10 (a) Relative standard deviation of step velocity phase map and (b) average step velocity phase map as functions of Damköhler number. High Damköhler number leads to step bunching.

Figure 3.10(a) shows the two regimes mentioned above of step-flow growth as a function of the step kinetic coefficient and diffusion coefficient. Different values of the Damköhler number (D_a) are represented by the contour colors. As mentioned above, the transition from high to low Damköhler number results in the variation of growth mode from bunching to stable. It implies that a stable crystal growth process requests a large diffusion coefficient but a small step kinetic coefficient. On the other hand, figure. 3.10(b) shows the average step velocity as a function of the step kinetic coefficient and diffusion coefficient. Two regimes are divided by the contour line on which the step velocity reaches 1.59 μm/s, and the macroscopic crystal growth rate reaches 100 μm/h. With one of the independent variables, say, the diffusion coefficient fixed, the increase in step velocity by raising the step kinetic coefficient will meet a limitation, vice versa. Thus, to increase the growth rate, the large diffusion coefficient is still necessary, and the step kinetic coefficient must also be raised.

The above discussion implies that the growth rate and surface morphology are partially a trade-off when designing solvent for crystal growth. Fortunately, there is an intersection between the fast growth regime and the stable growth regime, as shown in Figure 3.11. One can then refer to the intersection as the "ideal regime", where both the growth rate and the morphology are acceptable.

3.3.5 Solvent design based on Damköhler number

By locating solvent on the phase map shown in Figure 3.11, we can find the "best" solvent for solution growth of SiC. To locate the solvent, one needs both the diffusion coefficient and the step kinetic coefficient values. The data of diffusion coefficient of substances is available from databases. While for the mixtures, the data of diffusion coefficient is obtained using the Stokes-Einstein equation[16]. The viscosity data is estimated with the unified equation developed by Kaptay *et al*. [17]. However, the step kinetic coefficient remains unknown due to a lack of knowledge of the interface and solvation energy. Therefore, instead of using the step kinetic coefficient, we first locate the solvent by the reported growth rates as a contour line. The intersection point between this contour line and a vertical line indicating the value of diffusion coefficient then is asserted as the location of solvent. Bearing in mind the arbitrariness of all the estimations, we located several reported solvents on the phase map, as shown in figure 3.11. Since the reported cases have varied supersaturations, the step velocities are "normalized" by the supersaturations. The values of Si, $Si_{0.95}Ti_{0.05}$, $Si_{0.6}Cr_{0.4}$ and $Si_{0.56}Cr_{0.4}Al_{0.04}$ are typical values obtained in our previous experimental researches. While the values of $Si_{0.67}Al_{0.33}$ and $Si_{0.65}Ni_{0.31}Al_{0.04}$ are obtained from the report in which Onuma *et al*. precisely measured the step velocities through an *in-situ* observation to the step movement[12].

The coordinate of the solvents indicates that the solvent composition has a more negligible effect on the diffusion coefficient than on the step kinetic coefficient, and the elements reduce the diffusion coefficient without exception. Nickel and chromium improve the growth rate by increasing the step kinetic coefficients by almost an order of magnitude. People usually attribute growth rate increasing to the increase in carbon solubility. However, this study implies that these additive elements' modification of surface kinetics also contributes to the growth rate rise. On the other hand, adding aluminum decreases the step kinetic coefficient, stabilizing step bunching and decreasing step velocities.

3.4 Conclusion

Solvent design involving reaction rate and transport phenomena rate approaches rapid and stable crystal growth. In this study, simulations are carried out about the influence of kinetic coefficient and diffusion rate on the step flow growth of the crystal.

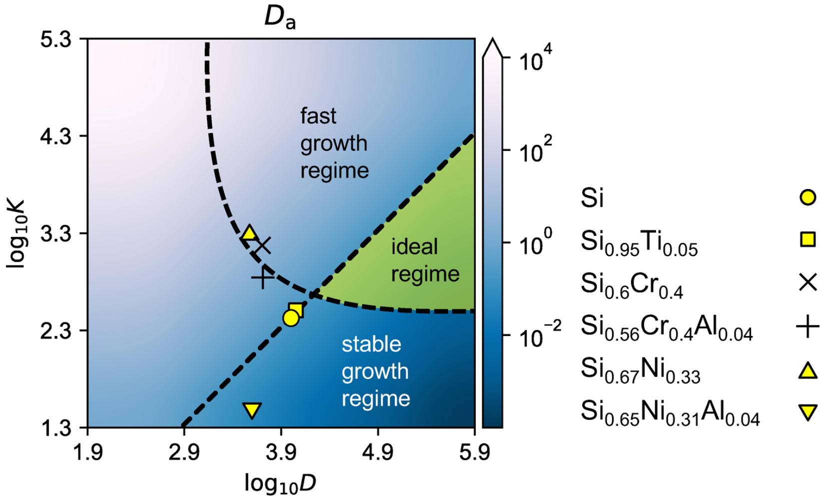

Figure 3.11 Phase map for solvent designing based on Damköhler number, several reported solvents are located on the phase map.

1. The evolution behavior of surface roughness depends on the value of $\mathcal{K}_{\mathrm{st}}$ because the dependence of step velocity on the local slope will be changed by $\mathcal{K}_{\mathrm{st}}$, switching surface stability.e
2. The dimensionless Damköhler number $D_{\mathrm{a}} = p\mathcal{K}_{\mathrm{st}}\delta/\mathcal{D}$ which determines the growth mode can be used as a criterion of intrinsic stability.
3. An ideal solvent for rapid-and-stable growth requires large $\mathcal{D}$ and moderate $\mathcal{K}_{\mathrm{st}}$ values.

Besides all the discussion above about the effect on step bunching behavior of the balance between step kinetics and mass transport, this study also reveals why supersaturation does not influence such step morphologies. As indicated by Mitani *et al.* [18]—changing supersaturation can only raise or lower step velocities in an aggregative manner, which does not affect the step velocity variance, thus no effect on step bunching behavior.

References

[1] P. G. Vekilov, H. Lin, and F. Rosenberger, Physical Review E **55**, 3202 (1997).

[2] Y.-I. Kwon, B. Dai, and J. J. Derby, Progress in Crystal Growth and Characterization of Materials **53**, 167 (2007).

[3] M. Inaba and M. Sato, Journal of the Physical Society of Japan **80** (2011), 10.1143/jpsj.80.074606.

[4] A. A. Chernov, Journal of Crystal Growth **118**, 333 (1992).

[5] A. A. Chernov, S. R. Coriell, and B. T. Murray, Journal of Crystal Growth **132**, 405 (1993).

[6] S. R. Coriell, B. T. Murray, A. A. Chernov, and G. B. McFadden, Journal of Crystal Growth **169**, 773 (1996).

[7] M. Uwaha, Progress in Crystal Growth and Characterization of Materials **62**, 58 (2016).

[8] I. V. Markov, *Crystal Growth for Beginners: Fundamentals of Nucleation, Crystal Growth and Epitaxy*, 3rd ed. (World Scientific, New Jersey, 2016).

[9] G. G. Gnesin and A. I. Raichenko, Soviet Powder Metallurgy and Metal Ceramics **12**, 383 (1973).

[10] R. I. Scace and G. A. Slack, The Journal of Chemical Physics **30**, 1551 (1959).

[11] W.-K. Burton, N. Cabrera, and F. Frank, Philosophical Transactions of the Royal Society of London. Series A, Mathematical and Physical Sciences **243**, 299 (1951).

[12] A. Onuma, S. Maruyama, N. Komatsu, T. Mitani, T. Kato, H. Okumura, and Y. Matsumoto, Crystal Growth & Design **17**, 2844 (2017).

[13] A. Chernov, Physics-Uspekhi **4**, 116 (1961).

[14] X. Li, J. Glimm, X. Jiao, C. Peyser, and Y. Zhao, Acta Mathematica Scientia **30**, 377 (2010).

[15] H. Oh, M. Sugiyama, Y. Nakano, and Y. Shimogaki, Japanese journal of applied physics **42**, 6284 (2003).

[16] A. Einstein, Annalen der physik **17**, 208 (1905).

[17] G. Kaptay, Zeitschrift für Metallkunde **96**, 24 (2005).

[18] T. Mitani, N. Komatsu, T. Takahashi, T. Kato, K. Fujii, T. Ujihara, Y. Matsumoto, K. Kurashige, and H. Okumura, Journal of Crystal Growth **401**, 681 (2014).

Chapter 4

A KMC investigation on 4H-SiC step kinetic coefficient and impurity-induced step bunching

4.1 Introduction

In the discussion in the previous contents of this thesis, the details of surface kinetics, *e.g.*, the values of the step kinetic coefficient and how they are affected by impurities, remain unknown. To further the discussion, say, to gain insight into the essence of these surface kinetics and their dependence on growth conditions, study on an atomistic scale is helpful. In this chapter, a kinetic Monte Carlo (KMC) model is introduced for solution growth of 4H-SiC to study the shape and behavior of equilibrated or growing steps, with or without the interference of impurities.

There have been some works on SiC and its growth kinetics with KMC methods in recent years. Borovikov *et al.* simulated the evaporation behavior of 6H-SiC. They succeeded in reproducing the experimentally observed tendency for single bilayer height steps to bunch into half unit-cell height steps by taking account of the different rates of surface diffusion on three inequivalent terraces, and in reproducing the experimentally observed tendency for adjacent pairs of half unit-cell height steps to bunch into full unit-cell height steps, by taking account of the different mobilities of steps with different structures[1]. His conclusion is in great consistency with Kimoto's work[2].

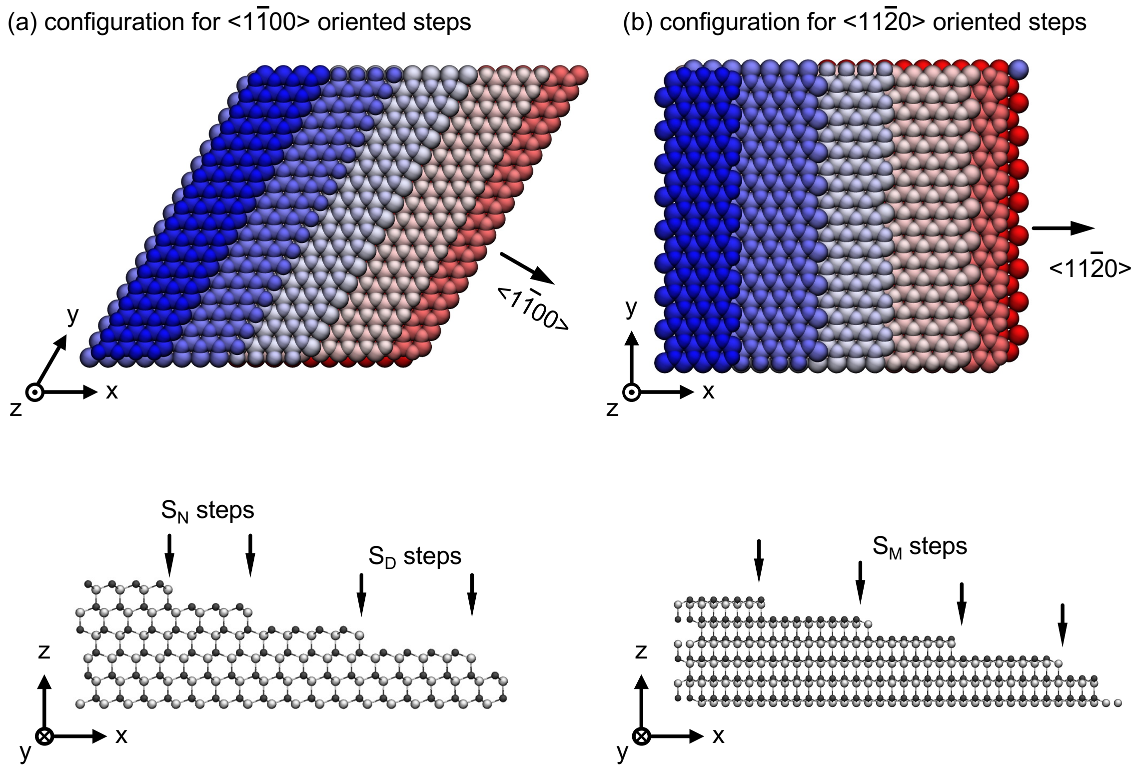

Figure 4.1 The initial configuration for simulation. The showing configuration is the C face. The color scale corresponds to the height in z direction. The four steps are classified as two types, see the discussion below. For the Si face, simply swap Si and C atoms. (Simulations visualized using VMD[3])

4.2 Computer simulation

A kinetic Monte Carlo simulation model is implmeneted utilizing the programming language C++. The model is similar to Borovikov's model[1]. A three-dimensional simulation model based on the crystal structure of 4H-SiC is constructed. Schematics of initial configurations (of the C face) are shown in figure 4.1. The color scale in the top-view indicates different bilayers. The x direction is the down-step direction, while the y direction is the direction in which steps extend. The sub-figures (a) and (b) indicate the initial configurations with steps oriented in <1$\bar{1}$00> and <11$\bar{2}$0> steps, respectively. The directions in which the steps orient to are also the directions they advance during growth. This study refers to the steps with their advancing directions instead of extending directions. The <1$\bar{1}$00> steps have two different types depending on the termination of the step edges. On the C face, the <1$\bar{1}$00> steps with the terminating Si atoms having one or two dangling unsaturated bonds are labeled as S_N and S_D steps, while the <11$\bar{2}$0> steps are labeled as S_M steps for it being a mixture of the two types.

A periodical boundary condition (PBC) is applied in the y direction while a helicoidal boundary condition (HBC) in the x direction, to eliminate the effect of boundaries on the steps[4]. The top and the top of the simulation box are closed.

The standard KMC method identifies a set of elementary events and catalogs their relative rates. In this study, we consider the attachment and removal of Si, C and other atoms. The rates of removal are determined according to the Arrhenius's law as

$$R^- = \nu_0 \exp(-E/k_B T) \tag{4.1}$$

where ν_0 is the attempt frequency set to be $10^{12}\mathrm{s}^{-1}$, k_B is the boltzmann constant and T is the temperature. The activation E for the p-atom is specified with the bond-counting rule

$$E_p = \sum_{\mathrm{NN.}} \sum_q \phi_{pq}. \tag{4.2}$$

The ϕ_{pq} representing the interaction strength between p and q species. The subscript NN. is short for the "nearest neighbors". Atom attachment is allowed on the empty sites of each species. *i.e.*, when a Si-site is empty, a Si atom can be added to it, while the attachment of a C atom is not allowed. The rates of attachment are constant.

$$R^+ = \nu_0 \exp(\frac{-2\phi_{\mathrm{SiC}} + \Delta\mu}{k_B T}), \tag{4.3}$$

$\Delta\mu$ is the driving force, corresponding to the supersaturation σ of the species by $\exp(\Delta\mu/k_B T) = 1 + \sigma$. To mimic the situation in solution growth, we only set the driving force of C to be positive, while for Si there is always $\Delta\mu = 0$.

Specially, there is

$$\begin{aligned} R^+ &= 0 \; (N = 0, 4), \\ R^- &= 0 \; (N = 4), \\ R^- &= \infty \; (N = 0), \end{aligned} \tag{4.4}$$

for an solid-on-soild (SOS) model and to keep the detailed balance, where N is the number of bonds.

This chapter focuses on step kinetics only and excludes the influence of mass transport on the steps, which has been discussed in the last chapter. Based on this consideration, mass transport, including fluid convection, diffusion in solution and surface diffusion, is excluded from this model.

4.2.1 Implementation of impurity

The attachment of impurity atoms is limited on the Si-sites. Since impurities is always added in solvent by replacing a part of the raw material silicon, the rate of impurity attachment is

$$R^{+}_{\mathrm{imp}} = fR^{+}_{\mathrm{Si},f=0}, \tag{4.5}$$

where f is the fraction the impurity takes from silicon. The attachment rate of Si then becomes

$$R^{+}_{\mathrm{Si}} = (1-f)R^{+}_{\mathrm{Si},f=0}. \tag{4.6}$$

The attached impurity atom can form at most N_{v} bonds with the neighboring C atoms in the binding strength ϕ_{imp}, where N_{v} is the number of valence electrons the impurity owns. For example, for Aluminum, $N_{\mathrm{v}} = 3$. The removal rate of an impurity atom depends on the number of bonds formed, N, by

$$R^{-}_{\mathrm{imp}} = \nu_0 \exp(-N\phi_{\mathrm{imp}}/k_{\mathrm{B}}T). \tag{4.7}$$

When the N_{v} is smaller than four, which is the coordination number of Si in the SiC crystal, the following rules are implemented together with impurity species.

1. When an impurity atom attaches to an empty Si site, it creates in most N_{v} new bonds with the neighboring C atoms. If there is less than N_{v} C atoms, the impurity atom remains unsaturated. While if there are more neighboring C atoms than N_{v}, the impurity will randomly form N_{v} bonds among the neighboring C atoms.

2. When the impurity atom is removed, all the relevant bonds will be broken(deleted).

3. Attachment of a C atom involves checking the neighboring impurity-occupying sites. Once the impurity is unsaturated, a new bond will be created between the newly attached C atom and the unsaturated impurity atom.

4. When a C atom is removed, the neighboring impurity-occupying sites are checked. The bonds between the removed C atom and the impurity atom, if

they exist, will be broken. Then the unsaturated impurity atom will look for and bind with unlinked neighboring C atoms.

4.2.2 Bond energies and temperature

A detailed discussion will show that the choice of schemes when determining the bond energies can cause a significant difference in the appendix. However, in the main body of this study, an effective bond strength between Si and C atoms, invented by Borovikov, of 0.75 eV, is used[1].

The value of 0.75 eV is inherited in some recent studies[5, 6], though their consideration about the "next nearest neighbors" seems to be a misunderstanding to Borovikov's report.

In this study, we applied this value of bond strength, although this value has been mentioned as invalid when the first time it is reported[1]. Also, the system Borovikov *et al.* studied was chemical vapor deposition (CVD). The temperature in his simulation was 1000 K, much lower than the growth temperature in the solution methods. Firstly the temperature dependence of step kinetic coefficient on temperature is watched. The result is that the thermal roughening occurred on the crystal surface at a temperature lower than 2000 K, which is invalid according to experimental results. However, all the matters are the $\phi/k_{\mathrm{B}}T$. Setting bond strength to be 0.75 eV then temperature to be 1000 K has no difference from setting the two parameters to be 1.5 eV and 2000 K. We still believe the simulation results at least give the correct tendency.

The bond strength of the Al-C bond is not reported except the dissociation energy of AlC molecular[7]. However, we can estimate its relative strength to the Si-C bond. Al is known to substitute for Si sites, and the bond length for the Al-C bond is 0.09 Å longer than the Si-C bond with a length of 1.89 Å is SiC[8]. Therefore We roughly estimate the Al-C bond being 0.715 eV.

In most results, the temperature is set to be 1000 K.

4.3 Results and discussion

As Borovikov's report mentioned, simulation results on the Si and C face show no significant difference in most cases. We lately concluded that it is due to the Si and C atoms being not distinguished under the bond energy determining scheme, which will be discussed in the appendix. Here we only present the simulation results carried out on the Si face, except when there is a significant difference in the results on the C face.

Figure 4.2 shows the equilibrated steps oriented in (a) <1$\bar{1}$00> and (b) <11$\bar{2}$0>. The simulation is carried out with four steps be separated by 54*a* to avoid any entropy repulsive interaction due to step meandering, where *a* is the lattice constant of 4H-SiC. The triangular insets on each terrace indicate the atom stacking sequence of the terrace. The steps at the right-side limit are squeezed out at the left-side limit due to the helicoidal boundary condition (HBC). The S_D and S_N steps show significant differences in the step shape. The S_N steps are generally straight with a few kinks on them. While the S_D steps are rough by breaking into segments of S_N steps, as indicated by the yellow lines. The yellow arrays indicate the advancing direction the S_N segments take. On the other hand, the S_M steps break into S_N and S_D segments and show a "zig-zag" shape. Each step has a different zig-zag orientation because it prefers S_N segments rather than the S_N segments.

(a) equilibrated <1$\bar{1}$00> oriented steps

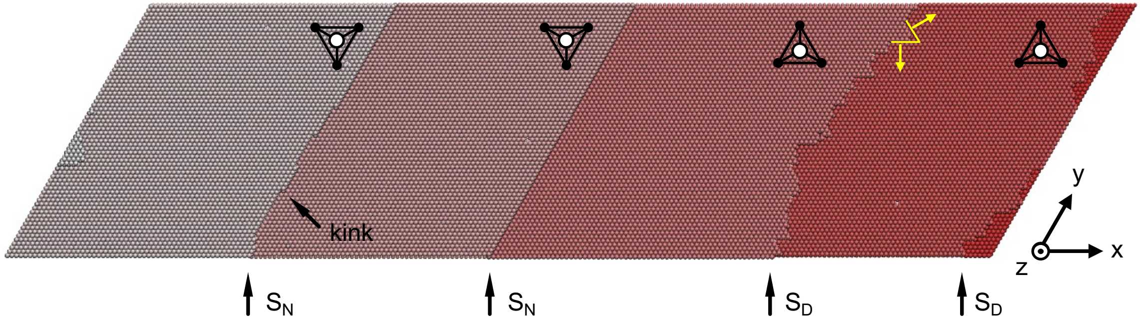

(b) equilibrated <11$\bar{2}$0> oriented steps

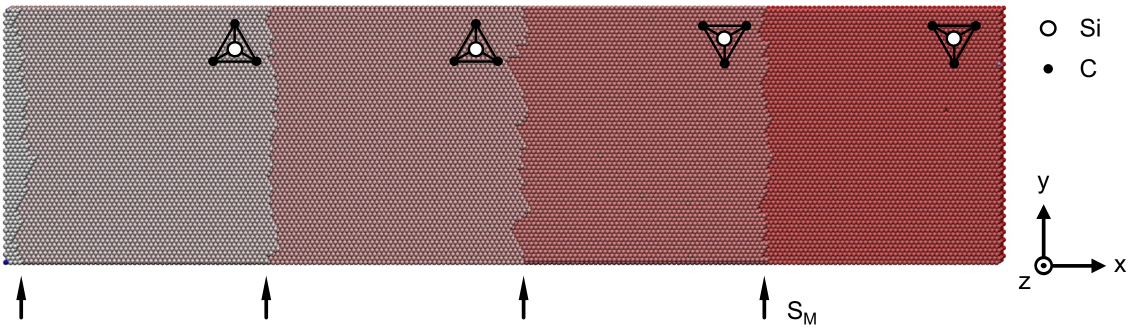

Figure 4.2 Configurations of equilibrated steps oriented in the (a) <1$\bar{1}$00> and (b) <11$\bar{2}$0> directions. The color scale represents height in the *z* direction.

4.3.1 Temperature dependence of kink density

Figure 4.3 shows the temperature dependence of kink density a/δ of (a, c) S_N and S_D step and (b, d) S_M steps, where a is the lattice constant and δ is the average distance between kinks. At temperatures above 2000 K, the kink densities show a rapid increase due to the thermal roughening, which is over the scope of this study. Therefore the discussion is limited in the low-temperature region.

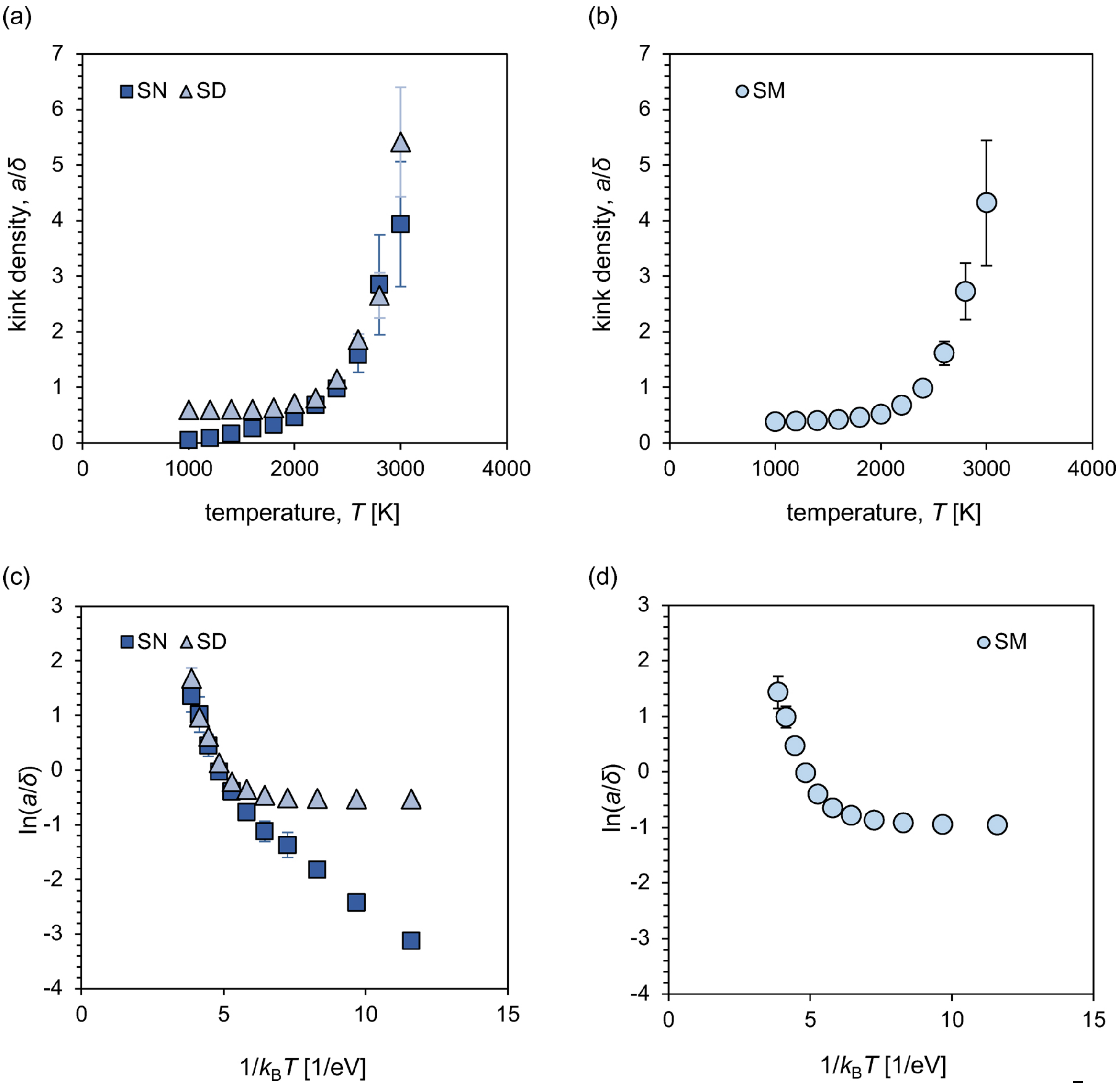

Figure 4.3 Temperature dependence of kink density on temperature of (a, c) <11$\bar{2}$0> steps and (b, d) <1$\bar{1}$00> steps.

Among the three types of steps, only the S_N step shows a clear exponential dependence on the temperature, which is indicated by figure 4.3 (c). The slope of the fitting line indicates the work cost for creating a kink on a S_N step being about

0.404 eV, about a half of the step edge energy of S_N step, 0.75 eV$/a$. The kink density on the S_D steps, in contrast, remains constant until the thermal roughening occurs, indicating a zero kink creation work on the S_D steps. The S_M steps have an almost constant non-zero kink density at low temperatures. The slight increase tendency can be attributed to the S_N segments in the zig-zag step edges.

With the kink density data, the step kinetic coefficient can be calculated according to equation 3.15. Note that kinks of both Si and C types empty sites are counted, while when considering step advancing, only filling a pair of Si and C empty sites counts. Therefore the "effective kink density", which is half of the plotted kink density, must be used. In this study, the energy barrier Δ is not explicitly specified and actually is was assumed to be zero. With this assumption, and noting that $a_{\mathrm{st}} = \sqrt{3}a/2$ for <1$\bar{1}$00> steps and $a_{\mathrm{st}} = a$ for <11$\bar{2}$0> steps, we have step kinetic coefficient estimated and listed in table 4.1 In a real liquid phase growth system, the energy barrier is of course not zero, however, the value is difficult, if not impossible, to measure. By arbitarialy assuming $\Delta/k_{\mathrm{B}}T \cong 1$, the values of step kinetic coefficients are scaled by 0.37 and are noted in the brackets in table 4.1.

Table 4.1 Estimated step kinetic coefficient, $\mathcal{K}_{\mathrm{st}}$ [10^7µm/s].

	1000 K	2000 K
S_N	0.038(0.014)	4.7(1.7)
S_D	5.9(2.2)	6.6(2.4)
S_M	4.6(1.7)	5.9(2.2)

4.3.2 Supersaturation dependence of step kinetic coefficient

Figure 4.4 shows the change in velocities of the three types of steps over supersaturation, σ. Both S_D and S_M steps show a linear dependence on the supersaturation, indicating a constant step kinetic coefficient that does not change with supersaturation. The step velocity can be written as $v_{\mathrm{st}} = \mathcal{K}_{\mathrm{st}}\sigma c_{\mathrm{eq}}v_{\mathrm{c}}$. In this study, $c_{\mathrm{eq}}v_{\mathrm{c}} = \exp(-2\phi/k_{\mathrm{B}}T) = 2.66 \times 10^{-8}$, therefore, by reading the slope of the fitting lines the $\mathcal{K}_{\mathrm{st}}$ can be figured out to be 3.12×10^7µm/s for the S_D step and 2.22×10^7µm/s for the S_M step. The inset shows the velocity of the S_N steps. The S_N steps do not move at low supersaturations, while when the supersaturation increases, in some data, the velocity can rise up to 0.1 µm/s. $\mathcal{K}_{\mathrm{st}}$ is then 4.14×10^6 µm/s in average, which is almost one order larger than the value obtained at σ=0. This rapid switching from still to a fast-advancing is because the S_N steps advance involves nucleation and spreading of "one-dimensional islands" on the step edges.

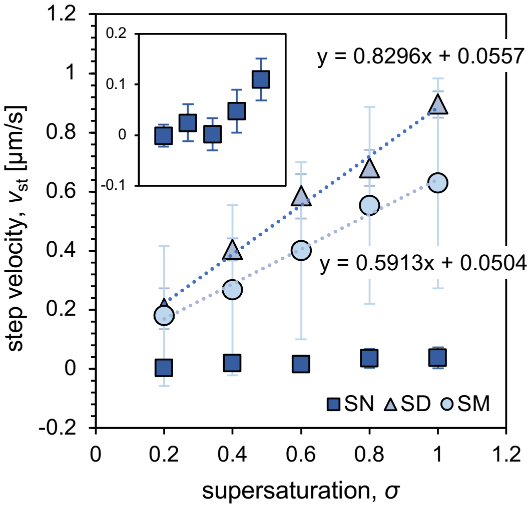

Figure 4.4 Step velocity changes with supersaturation.

4.3.3 Formation of four-bilayers bunching

The formation of four-bilayer step bunches is observed in simulation results. Figure 4.5 shows the processes of the four-bilayers step bunching. The simulation was carried out with 16 steps oriented to <1$\bar{1}$00> on a 216*a* × 40*a* surface (figure 4.5 (a)) under $\sigma = 1$. At low supersaturation conditions ($\sigma \leqslant 1$), S_D steps move much faster than the S_N steps and naturally result in the S_D steps catching up the front S_N steps. According to Kimoto's and Borovikov's reports, there is a difference in the energy barrier for depositing an atom on each terrace of 4H-SiC. The different deposition energy barrier first leads to step pairs of S_D steps and S_N steps, respectively. Then the difference in the step velocities leads to the bunching of S_D pairs into S_N pairs, forming step bunches of full-unit-cell height (four-bilayers height in 4H-SiC). In this study, however, this energy scaling effect on different terraces is intentionally neglected to better focus on the different types of steps. Therefore as indicated by figure 4.5 the formation of step pairs does not occur. Instead, the processes are (b) first a S_D step collides into the front S_N step, then (c) the other S_D step collides into the front S_D -S_N pair, and (d) the three-bilayer step pair collides into the front S_N step. Since the following sections discuss the behavior after forming the four-bilayer step bunches, though these processes are not exactly consistent with the processes

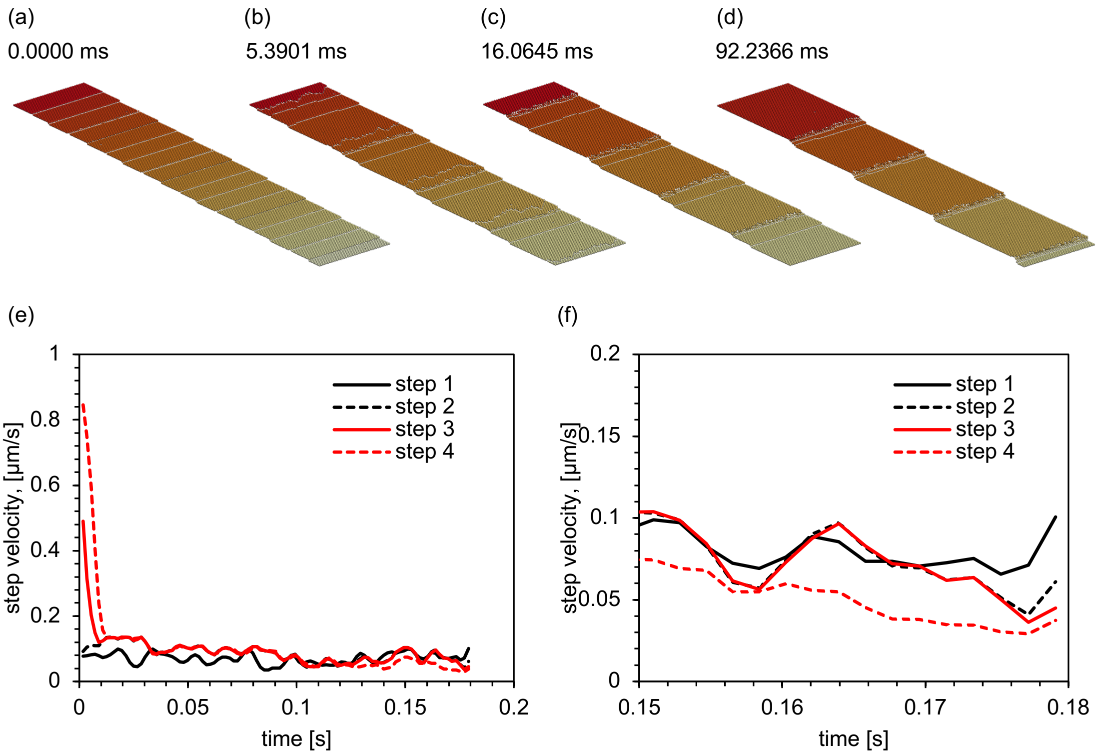

Figure 4.5 (a-d) Processes of formation of four-bilayers step bunches. (e, f) the change of step velocities during the processes of step bunching.

reported by Kimoto and Borovikov, it makes no significant difference. Also, the change in step velocities is shown in figure 4.5 (e). Steps are labeled as 1 ∼ four corresponding to the order in a four-bilayers bunch. After the collision into a front step, the step velocity immediately drops to the same level as the front step. Figure 4.5 (f) shows an enlargment of the step velocities after formation of four-bilayers step bunches. The whole bunch now advances in the same velocity of the “rate-limiting step”, the S_N step laying under the bunch.

4.3.4 Influence of Al-like impurity on step velocity

Aluminum (Al) is a typical impurity found in SiC crystals grown with the solution methods. The addition of Al usually has a significant influence on growth morphology. In this section, we included an Al-like impurity species during simulation. The simulations start from a clean $216a \times 64a$ surface with four steps. Both the Si and C faces are studied. During simulation, atoms of the Al-like impurity attach to the surface and gradually reach saturation. The attached impurity atoms can influence step velocity and step bunching behavior. This section first describes the interaction between impurity and steps and then discusses the influence of impurity on step velocities. In the next chapter, the step bunching behaviors will be briefly discussed.

Figure 4.6 shows surfaces with incorporated impurities. Although the attachment of impurity is spatially uniform, due to the variance in detachment rate, the resulted incorporations of impurity show spatial distributions, and the distributions are different on the Si and C faces. Since an Al-like impurity is only allowed to occupy a Si empty site, on the Si face, the impurities can incorporate by attaching to C atoms exposure at step edges or by taking vacancies left by the removal of surface Si atoms (in figure 4.6 (b) the white circle indicates a vacancy). Removing a surface Si atom requires breaking three Si-C bonds, making the latter process much unlikely than the former one. Thus, the adsorption of impurity at the step edges is much larger than on the terraces, as shown in figure 4.6 (a) and (b), there is a "step-incorporation" region behind the steps where the adsorption density of impurity atoms is much higher than the rest "terrace-incorporation" regions. While on the C face, although the impurities can directly attach to the terraces, between the attachment impurities and the surface C atoms, there is only one Al-C bond, the attachment is not solid, and these impurity atoms will be immediately removed. Furthermore, exchanging with the Si atoms is forbidden because the Si atoms are buried beneath the C atoms. As a result, all the impurities are incorporated at step edges on the C face. The white circle in figure 4.6 (d) shows the incorporated impurity leaving a pit on the terrace due to the fewer bonds and weaker binding caused by the impurity.

Since an Al-like impurity atom can form in most only three bonds, the incorporated impurity atoms generally hinder the steps from advancing, though the details may vary when interacting with different steps on different faces. For the straight S_N steps, a "kink blocking" mechanism works[9] While for the rough S_M steps, a Cabrera and Vermilyea (CV) pinning mechanism works[10]. As mentioned in the previous sections, the S_N steps advancing through nucleation and spreading of the 1D islands. When an edge of a 1D island comes to meet an embedded impurity atom, the spreading will be blocked because the Al-like impurity has already run out of its three bonds. In both the figure 4.6 (a) and (c) one can find impurity atoms blocking the spreading of 1D-island edges. Since the edges of the 1D islands are kinks, this mechanism is named kink-blocking. However, the blocked S_N steps continue advancing by forming new 1D islands. The white arrays in figure 4.6 (a) indicates the two edges of a newly formed 1D island.

While the S_M steps can be pinned by an impurity atom, although the reason for the S_M step cannot advance when meeting an impurity atom is the same as those for

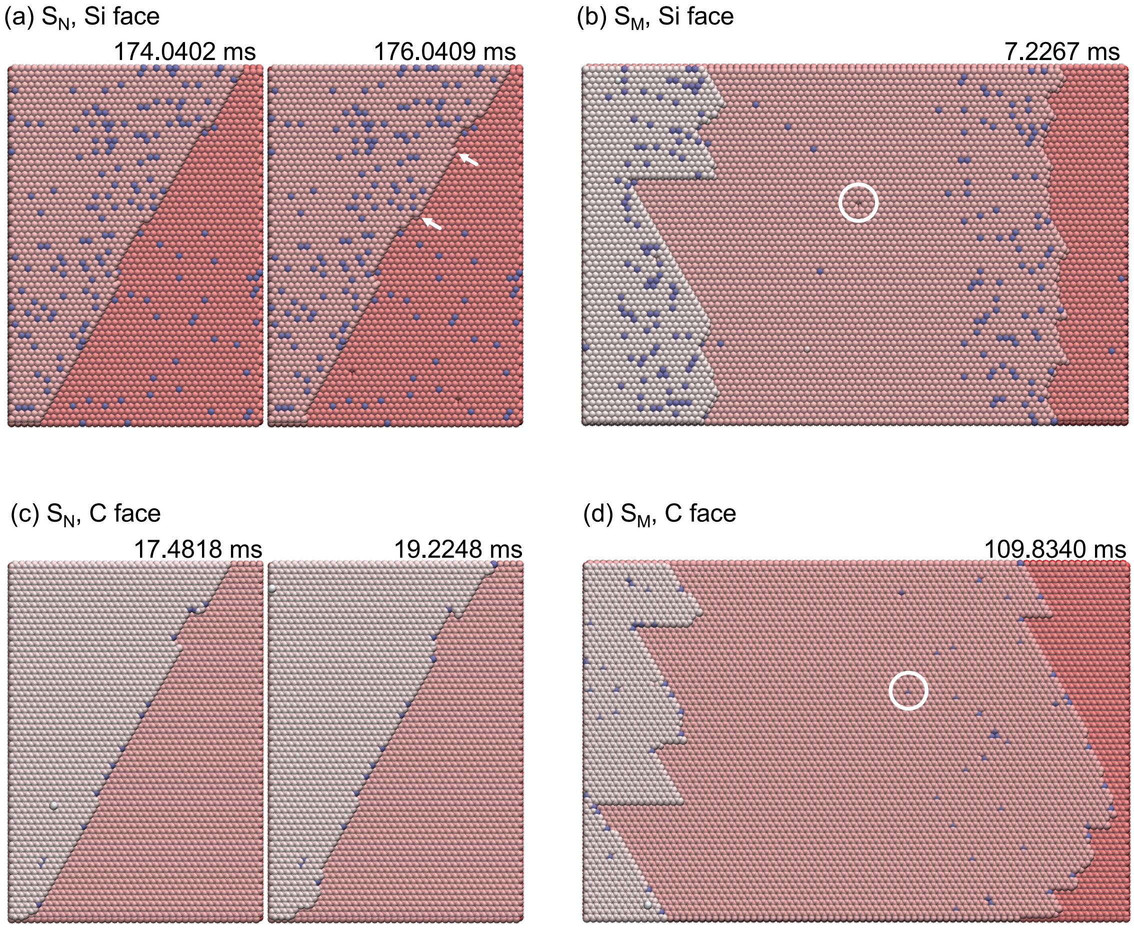

Figure 4.6 Steps influenced by impurities. S_N and S_M steps on both Si and C faces are displayed. The color level represents height in z direction. Impurities are displayed in a blue color.

the S_N steps, when an S_M step is pinned at some points, the rest part of the step can keep moving and leave the pinned sites behind, as shown in figure 4.6 (b) and (d), the valleys of zig-zag steps are the pinned sites.

The different mechanisms of impurity interacting with steps influence step velocities in different manners. Figure 4.7 shows velocity change over time when the Al-like impurity is present. When the steps advance in the <1$\bar{1}$00> direction, the S_N steps are focused as the rate-limiting steps. Figure 4.7 (a) and (b) show the results of the S_N and S_M steps on the Si face. Both steps show drops in the velocities. Figure 4.7 (a) shows change of S_N step velocities. Under small f conditions ($f = 0.02$), or when the growth time is short under large f conditions, the step velocities are hardly affected due to the low surface impurity density. While with the impurity fraction is large and after growth for a while ($t > 0.75s$), the step velocities drop to a lower level. If one looks carefully, there are as well three stages of the change of step velocities in the S_M steps shown in figure 4.7 (b). In the beginning, the adsorption starts attaching to the terraces and the step edges, while those attached to step edges have no influence, temporarily. With time increasing, the adsorption density on the terraces increases. Therefore, the step velocities decrease due to a step pinning effect. The drop stops after a certain period, and a plateau period comes. That is due to the adsorption reaching its saturation. However, later the velocities start dropping again to a lower level due to arriving into the “step-incorporation” region.

For the steps on the C face (figure 4.7 (c) and (d)), the situation is different from on the Si face. The decrease in step velocities only sustains for a much shorter period than the Si face. That is because impurities are only from the step edges, where impurity adsorption soon reaches saturation.

The step kinetic coefficients when impurity being present are calculated with step velocities and shown in figure 4.8 against the impurity fraction, f, and $a/\Delta = f^{1/2}$, where a is the lattice constant and Δ is the average distance between impurities embeded on the surface. For the S_M steps, the dependence is linearly fitted with equation

$$\mathcal{K}_{\mathrm{st}} = \mathcal{K}_{\mathrm{st}}{}^{0}(1 - 2R_{\mathrm{c}}/\Delta), \tag{4.8}$$

where R_c is the critical radius of 2D nucleation. The results of linearly regression is listed in table 4.2. The linear dependence of S_M steps on the Si face is well consistent with the observed step-pinning mechanism. On the other hand, impurity influence the S_M steps on the C face more than on the Si face. One can also see the influence of impurity gradually reaching a saturation with f increasing. On the C face, impurities only attach at step edges, thus, comparing with the steps on the Si face, the steps on the C face see a higher impurity density.

Table 4.2 Dependence on a/Δ of S_M step' kinetic coefficient (in unit [10^7µm/s]).

	dependence	correlation
Si face	$2.18(1 - 2.44x)$	-0.99
C face	$1.90(1 - 3.32x)$	-0.94

4.3.5 Further impurity-induced step bunching

Since in most cases, the S_N steps have a step kinetic coefficient of two orders more minor than the S_M steps, which implies that growth on a substrate with an off-axis

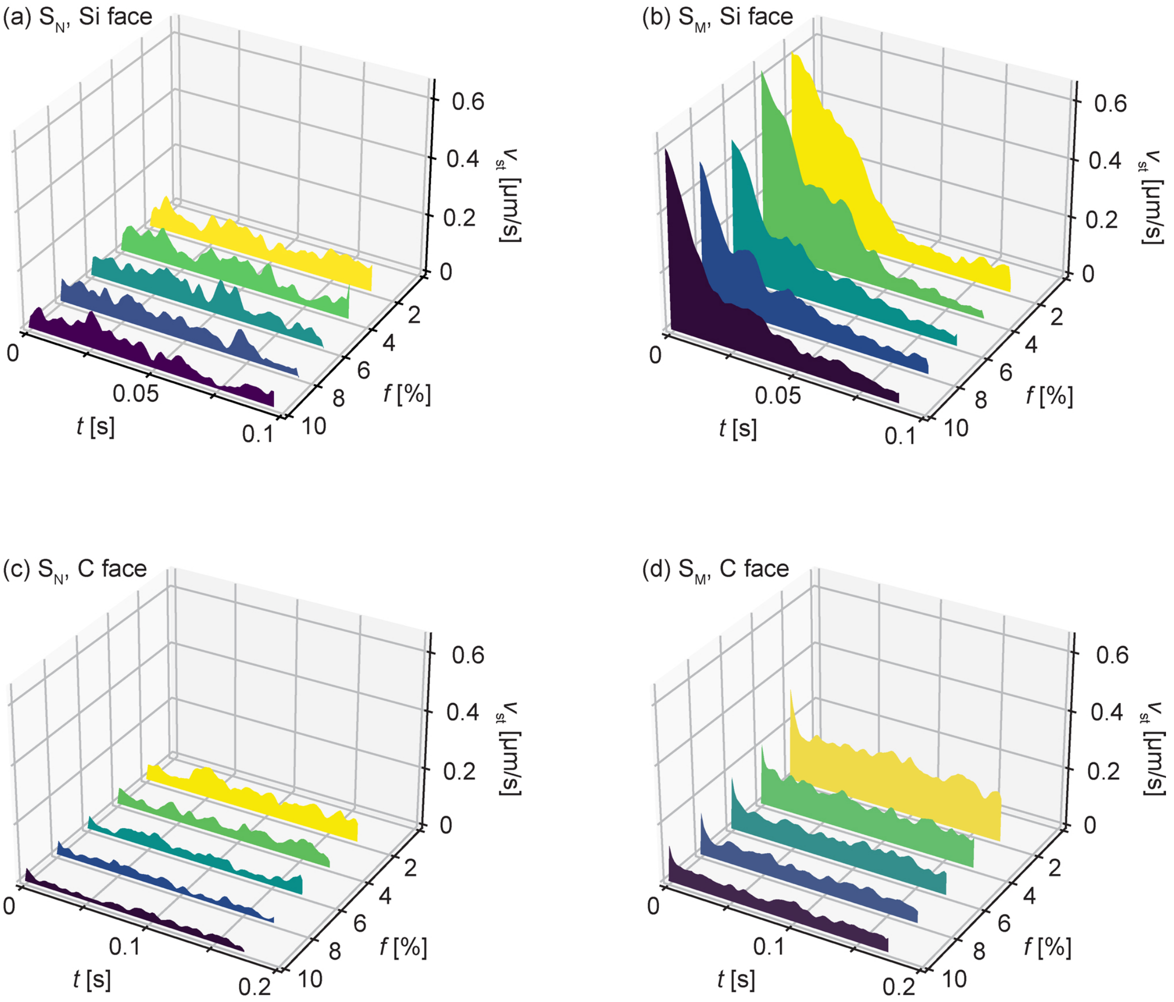

Figure 4.7 Change in step velocities, v_{st}, over time, t, with Al-like impurity present. f is the impurity fraction.

oriented to <1$\bar{1}$00> is more stable than growth on a <11$\bar{2}$0> oriented substrate. Also, the straight step line can eliminate fluctuation on step edges, which is considered to be the origin of the Bales-Zangwill instability (step meandering)[11]. The latter is considered to be relevant with the formation of inclusion in the grown crystals[12]. However, another consequence of growing with <1$\bar{1}$00> steps is that the growth will be much slower. So it is a trade-off problem.

In the solution methods, when one changes the polarity face to grow on, the addition of Al has opposite effects on growth morphologies. The mechanism is still unclear, but the above results about the effects of the Al-like impurity on step velocities may give some hints. There may be two different mechanisms affecting step bunching: the change in step kinetic coefficient and the impurity-induced step

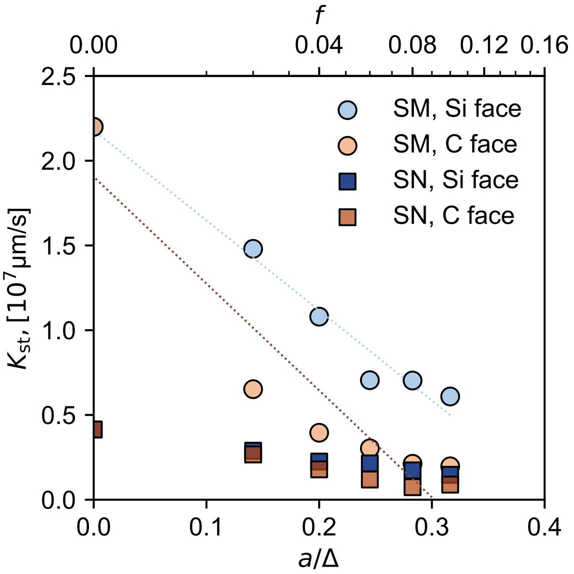

Figure 4.8 Step kinetic coefficients calculated from step velocities with impurity present.

bunching. Comparing the step velocities affected by impurity on the Si and C faces, shown in figure 4.7, even with the same impurity fraction, the finally resulted velocity can be different, especially when $f = 0.02$ and $f = 0.04$. This difference may have an influence on step bunching behavior through the mechanism discussed in chapter 3. However, as this model does not consider mass transport explicitly, step bunching through this mechanism will never be observed. On the other hand, the impurity-induced step bunching may become dominant.

The fundamental consideration of impurity-induced step bunching has been introduced in section 1.4.3 As one can read from figure 4.7, there is a period, τ, for the impurity to reach the saturation on the Si face during this period much shorter on the C face. If the key assumptions of the Cabrera-Vermilyea model is validated, the characteristic adsorption time of the impurity, impurity-induced step bunching will occur when

$$\frac{w}{v_{st}\tau} \leqslant 1, \tag{4.9}$$

where w is the terrace width, v_{st} is the step velocity and τ is the so-called characteristic adsorption time of impurity[13]. The S_M steps on the Si face have a larger v_{st} while a longer τ, compared with the S_M steps on the C face, leading to a higher risk of impurity-induced step bunching on the Si face.

Simulations with a larger surface and longer growth time are carried out to see the impurity-induced step bunching. Figure 4.9 shows the results. The simulations are carried out on a $640a \times 64a$ clean surface with 32 equally aligned steps, under a low impurity fraction, $f = 0.02$. The growth face is the Si face. Both the <1$\bar{1}$00> steps (figure 4.9 (a) and (b)) and <11$\bar{2}$0> steps (figure 4.9 (c) and (d)) are simulated. Except the cases with the supersaturation $\sigma = 1$ and the binding strength $\phi_{\mathrm{imp}} = 0.715$ eV, simulations with $\sigma = 4$ (faster steps) and $\phi_{\mathrm{imp}} = 0.84$ eV (longer characteristic adsorption time) are also carried out. According to Van der Eerden *et al.*, the characteristic adsorption time can be written as $\tau = \tilde{n}/\nu$, where $\tilde{n}$ is the equilibrated adsorption density and ν is the adsorption flux[14]. By increasing the ϕ_{imp} the equilibrated adsorption density thereby, the characteristic adsorption time can be modified.

From the results, no obvious step bunching behavior can be observerd with the former conditions, neither in the <11$\bar{2}$0> and <1$\bar{1}$00> steps, (figure 4.9(a, c)). On the other hand, with faster steps and a longer adsorption time, the steps show gathering and separation with each other (figure 4.9(b, d)). One may consider this a step bunching on a larger scale. However, by looking carefully into the change of the distance between the two bunch of steps, one may find that separated steps can gather again(figure 4.9(b)), which leads to the changes among step distances more likely some random fluctuation rather than instability. This result violates the experimental results, in which the addition of Al leads to step bunching when growing on the Si face.

The primary reason for failing to reproduce the experimental tendency may be attributed to the incorporation of impurity by prioritizing the steps rather than terraces on the Si face. Unlike the terrace incorporation, the attachment to step edges of impurity immediately reaches saturation. This difference makes the adsorption density in the "step-incorporation" region is all the same and irrelevant with the terrace width. In other words, it is like the τ is too small for $w/v_{\mathrm{st}}\tau$ to fall within the step bunching range, $w/v_{\mathrm{st}}\tau \leqslant 1$.

4.4 Conclusion

In this chapter, a kinetic Monte Carlo model is constructed on the 4H-SiC lattice. The kinetic coefficient of <1$\bar{1}$00> and <11$\bar{2}$0> step are investigated, on both the Si and C faces, over different temperatures, supersaturation, and condition of impurity adsorption. The <1$\bar{1}$00> steps consist fast $\mathrm{S_D}$ steps and slow $\mathrm{S_N}$ steps. At equilibrium, in a temperature range being lower than thermal roughening temperature. Step kinetic coefficients are obtained by counting the kink densities. An $\mathrm{S_D}$ step is

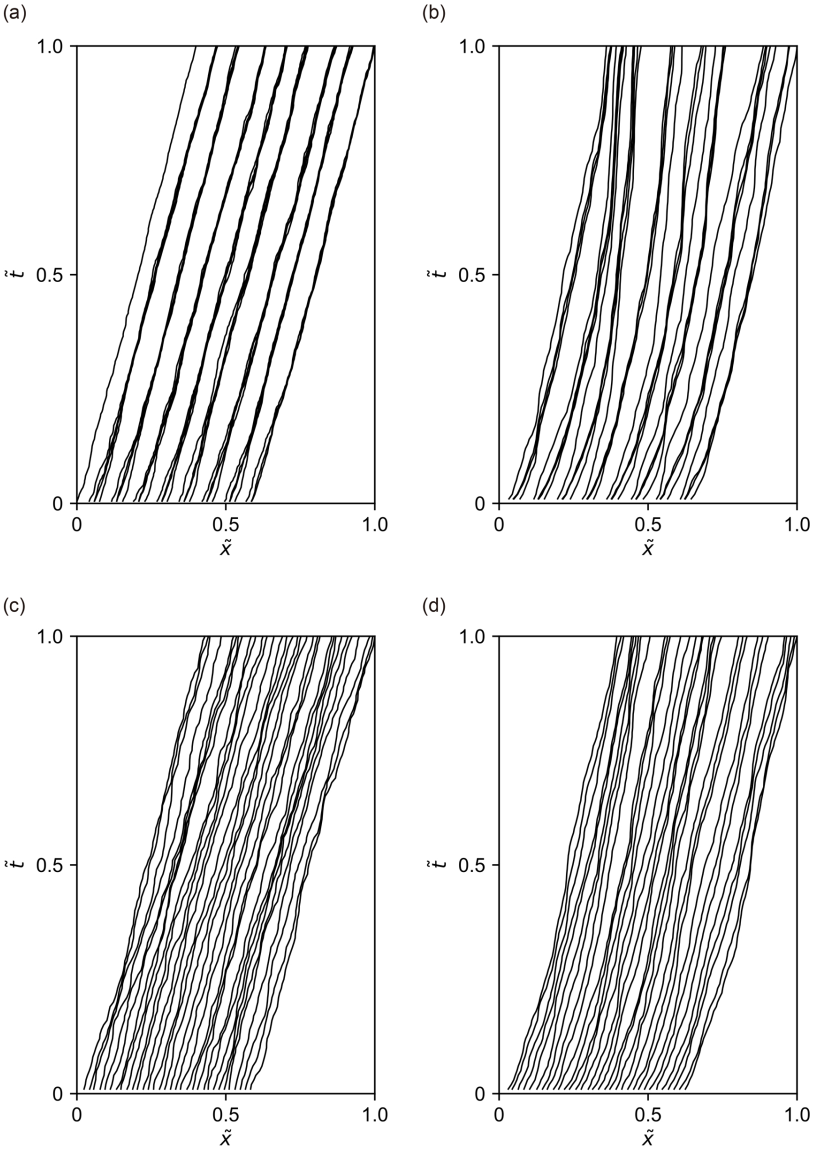

Figure 4.9 Step positions change over time. The time and position are normalized. (a) <1$\bar{1}$00> steps, $\sigma = 1$. $\phi = 0.715$ eV, (b) <1$\bar{1}$00> steps, $\sigma = 4$. $\phi = 0.84$ eV, (c) <11$\bar{2}$0> steps, $\sigma = 1$. $\phi = 0.715$eV, (d) <11$\bar{2}$0> steps, $\sigma = 4$. $\phi = 0.84$ eV.

constantly rough and has a sizeable kinetic coefficient. The kinetic coefficient of an S_N step is two orders smaller but increases exponentially with temperature. An S_M step has similar roughness with the S_D steps. When the supersaturation is non-zero, the step kinetic coefficient is calculated as a ratio between the step velocity and the supersaturation. The calculated kinetic coefficients are generally consistent with the ones obtained at equilibrium. Due to the difference in step velocities, step bunching occurs intrinsically among the <1$\bar{1}$00> steps to form four-bilayers step bunches, and the S_N steps located at the bottom of each bunch act as the rate-limiting step. Finally, an Al-like impurity was introduced. The step pinning mechanism works on the S_M steps, while a kink-blocking mechanism works instead for the S_N steps. Both mechanisms hinder the steps from advancing. However, the two mechanisms and the different adsorption behaviors observed on the Si and C faces lead to different effects on the step velocities. On the Si face, the impurity adsorbs to both the terrace and the step edges, while the former appears a time dependence of the adsorption density, which is considered the origin of the impurity induced step bunching. On the C face, such a time dependence is minor, which eliminates the probability of the impurity-induced step bunching. Simulations were carried out to verify the impurity-induced step bunching. However, due to the overwhelming amount of impurity adsorption at the step edges, the effect of terrace adsorbed impurity was covered up so that no solid evidence of impurity-induced step bunching was observed. In order to fully reveal the mechanism in which aluminum affects the step bunching behaviors, we look forward to furthering studies, especially experimental studies on the adsorption sites of the aluminum during crystal growth.

References

[1] V. Borovikov and A. Zangwill, Physical Review B **79** (2009), 10.1103/PhysRevB.79.245413.

[2] T. Kimoto, A. Itoh, H. Matsunami, and T. Okano, J. Appl. Phys. **81**, 8 (1997).

[3] W. Humphrey, A. Dalke, and K. Schulten, Journal of Molecular Graphics **14**, 33 (1996).

[4] M. Camarda, A. L. Magna, and F. La Via, Journal of Computational Physics **227**, 1075 (2007).

[5] F. Krzyżewski and M. A. Załuska–Kotur, Journal of Applied Physics **115**, 213517 (2014).

[6] Y. Li, X. Chen, and J. Su, Applied Surface Science **371**, 242 (2016).

[7] Y.-R. Luo and J. A. Kerr, CRC handbook of chemistry and physics **89**, 89 (2012).

[8] M. Stockmeier, R. Müller, S. A. Sakwe, P. J. Wellmann, and A. Magerl, Journal of Applied Physics **105**, 033511 (2009).

[9] J. J. De Yoreo, L. A. Zepeda-Ruiz, R. W. Friddle, S. R. Qiu, L. E. Wasylenki, A. A. Chernov, G. H. Gilmer, and P. M. Dove, Crystal Growth & Design **9**, 5135 (2009).

[10] N. Cabrera and D. A. Vermilea, in *Growth and Perfection of Crystals* (Cooperstown, New York, 1958) p. 411.

[11] N.-b. Ming and F.-g. Zhou, in *Morphology and Growth Unit of Crystals*, edited by I. Sunagawa (Terra Scientific Publishing Company, Tokyo, 1989) pp. 349–364.

[12] A. A. Chernov, *Modern Crystallography III*, edited by M. Cardona, P. Fulde, and H.-J. Queisser, Springer Series in Solid-State Sciences, Vol. 36 (Springer Berlin Heidelberg, Berlin, Heidelberg, 1984).

[13] R. I. Ristic, J. J. DeYoreo, and C. M. Chew, Crystal Growth & Design **8**, 1119 (2008).

[14] J. van der Eerden and H. Müller-Krumbhaar, Electrochimica Acta **31**, 1007 (1986).

Chapter 5

Real-world data circulation in crystallization research

5.1 Data circulation in model-driven studies of crystal growth

This chapter discusses the contributions of the thesis in the context of real-world data circulation (RWDC). Contributions to data circulation in computational studies of materials, particularly model-driven crystal growth studies, are discussed.

The data circulations in the study of crystal growth are illustrated in figure 5.1. Conventionally, optimization of crystallization craft involves complicated and long-term experimental research. The processes and data circulation is illustrated in figure 5.1 by thick lines. Firstly, crystal growth experiments are carried out as a pilot study. In this stage, experiment conditions will be set according to the researchers' intuition and experience. The obtained crystals then will be characterized in different scales. In our research, on the macroscale, usually, the growth rate and surface morphology will be observed. Step bunching is in concern on the mesoscale, while the impurity distribution will be measured on the microscale. The characterization results are acquired through this stage as dependent variables, with the experimental conditions as the independent variables. The acquired data set then will be analyzed. Knowledge, theories, and principles of crystal growth and general physics were inducted through this stage. Finally, the concluded knowledge is used to design experiment conditions for the subsequent experiments or guide industrial mass production.

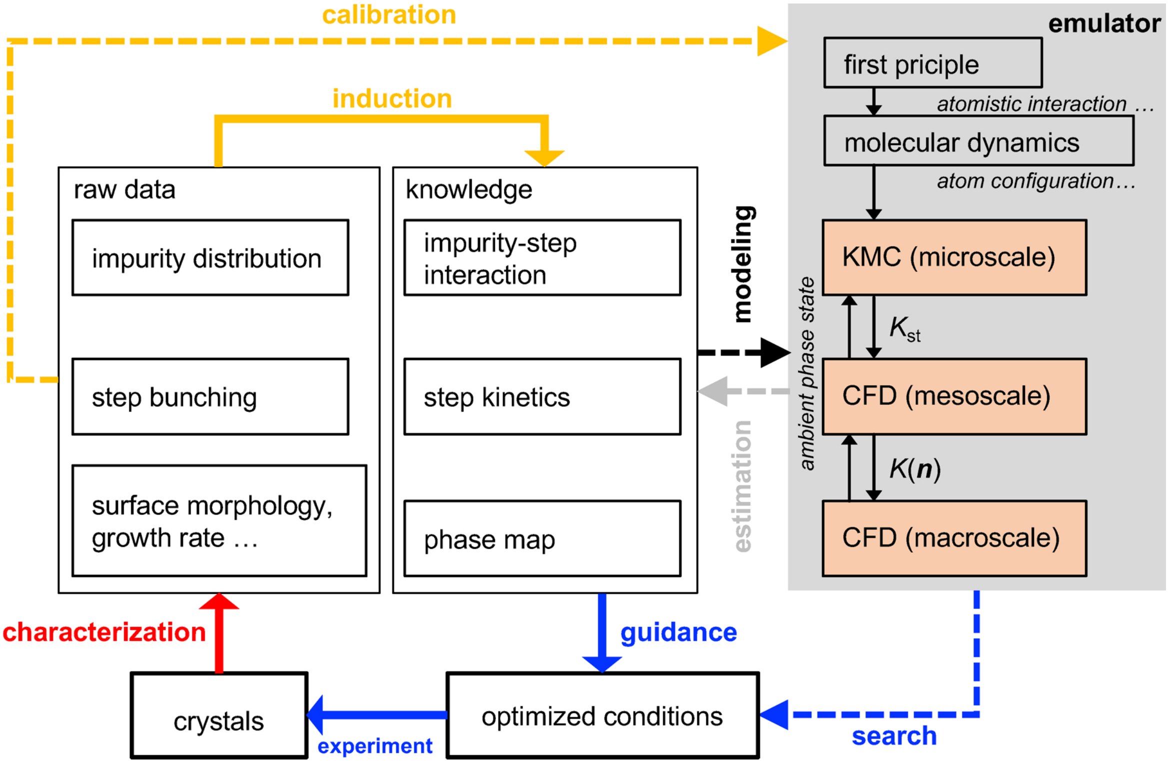

Figure 5.1 Data circulation in experimental (thick lines) and emulator driven (dashed lines) studies in crystal growth. Multiscale modeling of the crystal growth process (shaded in gray), the focus of this thesis, is fundamental to constructing the emulator and data circulation. Arrays representing the acquisition, the analysis, and the implementation of data are colored with red, yellow, and blue, respectively.

However, several rate-limiting processes in the conventional data circulation are also issues hindering the exploration of the optimized experiment condition for crystallization. In the stage of data acquisition, when multiscale characterization is needed, this process usually becomes slow and expensive. Moreover, to optimize the craft for crystallization, usually, tens of parameters must be modified. It means that to effectively analyze the crystallization processes, numerous raw data is necessary. That is why in some cases, developing a new material takes decades. The third difficulty happens in the data analysis stage. Even though with enough raw data set obtained, the relation between the experimental conditions and the characteristic of the crystal may not be easily found even by an experienced researcher. Because the formation of a material is a highly complicated process involving different mechanisms that work in different length scales. Although a knowledgeable researcher is supposed to use the knowledge to explain the phenomena observed in each scale, combining all the information and predicting the behavior of such a complex system is usually difficult for human beings.

With the development of modeling technologies and increased computational resources, an innovative approach to optimizing crystallization craft has been proposed. The data circulation in this new approach is illustrated in figure 5.1, by dashed lines. The new approach is driven by an "emulator". An emulator is a computer model of a real system that can reproduce the system's behaviors. In the case of crystal growth, an emulator is considered a computer model of the system in which crystal growth experiments are carried out. It is expected to fully reproduce the whole crystallization process, including the transport of mass and heat and the surface kinetics. With such an emulator, researchers can explore all parameters affecting the crystallization, implying that optimized experimental conditions can be obtained in a short period with extremly low cost. In this approach, only a few batches of experiments are necessary to acquire data for the calibration of the emulator. With an emulator, the data acquisition and analysis processes are automated and hidden in the emulator, which is expected to significantly accelerate the period for optimization of the crystallization craft.

An emulator requires modeling using human knowledge. Models on different length scales are necessary for the emulator used in crystallization research, corresponding to the real-world data. As shown on the right side of figure 5.1, several typical modeling methods are listed. Models on different scales require data and knowledge towards the corresponding scale. The result of this thesis, which is multi-scale modeling to step behaviors, satisfies the emulator's need, and the contribution will be discussed in the following sections.

Between each scale, there is data circulation as well. Take the research thesis as an example. The microscale model, KMC, produces values of step kinetic coefficient, $\mathcal{K}_{\mathrm{st}}$, to the mesoscale-CFD model as inputs. The surface morphologies outputted by the mesoscale-CFD simulation can also be inputted to the macroscale-CFD simulation, as finer boundary conditions. On the other hand, the outputs of macroscale-CFD simulation providing information about the ambient phase are also necessary for the models on smaller scales.

It is worth note there is not a certain order when using these models. For example, with the mesoscale-CFD model, morphology can be obtained. By comparing with the experimentally acquired data, determining the value of $\mathcal{K}_{\mathrm{st}}$ then becomes the so-called inverse problem. Moreover, the $\mathcal{K}_{\mathrm{st}}$ obtained by solving the inverse problem can be compared with that obtained in KMC for model calibration.

5.2 Contribution of this thesis to model-driven studies of crystal growth

To fully reproduce the whole process in crystallization, the emulator must know "what is going to happen" with a group of experiment conditions as input. Although the knowledge an emulator has will not override humans, the advantage of an emulator is that it can deductively reproduce the system's behavior with the knowledge it has. For example, as part of the emulator, the CFD simulation allows us to calculate the distribution of temperature, pressure, fluid flow velocity, and much other information, with only a few equations and limited assumptions.

Naturally, an emulator for crystallization shall at least reproduce the mass transport process and growth kinetics during crystallization. However, in the case of solution growth of SiC crystals, the currently widely used models (macroscale-CFD models) are far from enough. As indicated in chapter 3, besides the controlling parameters, *e.g.*, the temperature, the solvent composition also impacts the quality of crystals. The macroscale-CFD models do not consider the growth kinetics and fail to predict crystal quality.

Therefore, an emulator requires multiscale modeling to the crystallization process, including mass transport and surface kinetics. Particularly, for the study of step bunching, models describing mass transport and step kinetics on multiscale are necessary. The contribution of this thesis to model-driven studies of crystal growth and the related data circulation can be concluded as follows

1. Multiscale models describing mass transport and step kinetics in crystallization are constructed.

2. with the result of chapter 3, step bunching can now be reproduced in a mesoscale-CFD model. The solvent composition can be included when predicting the quality of the grown crystal.

3. with the result of chapter 4, an atomistic model was constructed to reveal the possible microscopic mechanism for impurities affecting step bunching. The model is promising in enriching the possibilities and improving the accuracy when considering the effect of solvent composition on the emulator.

The extended contribution of this thesis to other fields will be briefly discussed in the next section.

5.3 Contribution of the thesis to related fields

Parameter optimization

In crystal growth, the solvent composition, along with other parameters such as temperature, determines the quality of the crystals. Conventional hydrodynamic models are only good at predicting the macroscopic effects caused by the parameters. By coupling my model with the conventional models, it is possible to predict the quality of the grown crystals based on the solvent composition and other parameters. By developing exhaustive simulations in the variable space of solvent composition and other growth parameters and building a prediction model with solvent composition and other parameters as input and crystal growth rate and quality as output, Parameter optimization on the conditions for crystal growth can be conducted.

Application in materials informatics

However, in real industrial production, even if the other conditions are the same, the crystals obtained can be quite different due to the differences in the delicacy of the experimental equipment, and the proposed optimal conditions often deviate. In addition, the model is losing its accuracy as the growth apparatus, and components deteriorate with time. To solve this problem, a transfer learning approach can be proposed based on the conclusion of this thesis.

1. Collect the above input and output data as routine growth experiments are developed in each growth apparatus.
2. Based on the collected data, one can use a transfer learning method to periodically update the trained model and propose optimal conditions that take into account the individuality and condition of each growth apparatus before each experiment.

Application in other related fields

In industrial production, simulation results of the mesoscale model (Chapter 3), which is the surface morphology, can be applied to predict and visualize the surface morphology.

The microscale KMC model can be extended for studies of crystallization of other materials. Also, the ion implantation process is significant in the fabrication of semiconductor devices. The distribution of injected ions, which greatly impacts device performance, can be studied using the KMC model.

Chapter 6

Conclusion

This study aimed to establish a solution method for creating high-quality 4H-SiC crystals. We focused on the controlling step bunching in this study. Experimental and multiscale numerical investigations towards the growth processes is utilized to reveal the mechanism of the mass transport and step kinetics affecting step bunching. Here, the knowledge obtained in each chapter is summarized below.

Chapter 1 provided the background of this study. From chapter 2 to chapter 5, the study contents are described. In chapter 2, we conducted growth on a SiC substrate of 2-inch size. In order to obtain dislocation conversion, we utilized Ti 5 at.% composited solvent. We obtained a high-quality crystal with dislocation conversion. For the first time, we observed the spatial distribution of step height and thus conversion ratio in the step flow direction. We figured out the origin of the step height distribution by modeling the fluid flow in the growth system. The central-symmetrical out-ward flow beneath the growth front resulted in an antiparallel and parallel flow in step flow's upstream and downstream areas, which leads to the opposite step bunching behaviors in the two areas. This discovery provides a pointer to the designing of growth craft in order to obtain crystals of uniform quality.

In chapter 3, the influence of flow velocitiy on step bunching size was reproduced in a mesoscale numerical model. Furthermore, to reveal the mechanism for solvent composition influencing step bunching behavior and provide a pointer to the solvent design, we constructed a model coupling the mass transport and the step kinetic and conducted a numerical simulation. We revealed that step bunching originates from the minor, random fluctuation of step distances while is determined by the ratio between step kinetics rate and mass transport rate, which are represented by the step kinetic coefficient and diffusion coefficient. Based on this insight, we constructed a dimensionless number as a measurement for solvents of the tendency to cause step bunching. We also revealed that to obtain a crystal with an acceptable growth rate and maintain surface smoothness, fast diffusion and moderate step kinetics are ideal.

In chapter 4, to quantitatively obtain the step kinetic coefficient of 4H-SiC and study its dependence on growth conditions, a kinetic Monte Carlo model was constructed. The step kinetic coefficient was calculated over all types of steps on the {0001} faces. The dependence of the step kinetic coefficient on temperature, supersaturation, and the existence of impurity species was investigated. The steps advancing in the $<1\bar{1}00>$ direction were divided into the S_N type and the S_D type. The S_N steps keep straight at even high temperatures and move slowly, while the S_D steps are constantly rough and fast. The S_N steps usually have a kinetic coefficient of ($3.8 \times 10^5 \mu m/s$, 1000 K) two orders smaller than the S_D steps have ($5.9 \times 10^7 \mu m/s$, 1000K). The steps advancing in the $<11\bar{2}0>$ direction (S_M steps) have a similar roughness, thereby a close kinetic coefficient ($4.6 \times 10^7 \mu m/s$, 1000 K), as the S_D steps. Due to the difference in step velocities, step bunching occurs intrinsically among the $<1\bar{1}00>$ steps to form four-bilayers step bunches, and the S_N steps located at the bottom of each bunch act as the rate-limiting step. With the existence of an aluminum-like impurity species, S_M steps were pinned by the impurities, while the S_N steps show a kink-blocking mechanism instead. Both the two mechanisms in which impurity interacts with steps hinder the steps from advancing. The impurities adsorb to both terrace and step edges on the Si face. The former adsorption's Langmuir style behavior was considered an origin of the impurity-induced steps bunching on the Si face. While on the C face, the adsorption to the step edges is the only way the impurity is incorporated, which does not lead to an impurity-induced step bunching. The distinct behaviors were considered to be able to explain the opposite surface morphologies when growing SiC on the Si and C faces with Al present, and simulations were carried out to verify this theory. However, due to a high adsorption density at the step edges, on the Si face, the effect of the Langmuir style adsorption is eliminated, and no solid evidence supporting the impurity-induced step bunching was observed.

In chapter 5, the relationship between this study with Real-world data circulation is discussed.

Appendix A

A KMC rate-determining scheme to reflect polarity of SiC crystal {0001} faces

In chapter 4, a kinetic Monte Carlo (kMC) simulation model for 4H-SiC is constructed, and the temperature dependence of step kink density is studied. The model is found not to be able to reveal the difference between the Si and C faces, except when including impurity species, which is the same as being mentioned in the reference [1]. However, this is invalid. According to extensive experimental results and calculations, the SiC crystal shows a polarity in the *c*-axis. That is, the Si and C faces have different properties. For example, [2] calculated that the surface energies being 300 erg/cm^2 for the C face and 2200 erg/cm^2 for the Si face. To fully reproduce the properties and growth behaviors of SiC crystal, this polarity should be considered. In this appendix, a different scheme in determining event rates is utilized in the kMC model constructed in chapter 4 as a try to represent the polarity in the SiC crystal.

A.1 Rate determination

This model is based on the idea of a binary ion-like crystal growth model by Cherepanova *et al.*. A general rate-determining principle for the growth of binary crystals (AB crystals) is derived and applied in the research of NaCl-like ionic crystal[3, 4]. Since we are not going to discuss the intrinsic disorder in the crystal, in this chapter, the scheme is simplified by forbidding atoms from occupying sites that do not correspond to the atom types. The attachment rate of an a particle from fluid phase to crystal is

$$R_{\mathrm{a}}^{+} = \nu_0 \exp(\Delta\mu_{\mathrm{a}}/k_{\mathrm{B}}T), \tag{A.1}$$

and the detachment rate is given by

$$R_{\mathrm{a}}^{-} = \nu_0 \exp(\Delta E/k_{\mathrm{B}}T). \tag{A.2}$$

Here ν_0 is the attempt frequency, $\Delta\mu$ is the driving force, and

$$\Delta E = (N-2)\varphi_{\mathrm{ab}} + (4-N)\varphi_{\mathrm{af}} - N\varphi_{\mathrm{bf}} \tag{A.3}$$

is the energy change after the detachment scaled by the change in bonds. The bond energy between an pair of particles, i and j can be written as

$$\varphi_{\mathrm{ij}} = \phi_{\mathrm{ij}} - \frac{1}{2}(\phi_{\mathrm{ii}} + \phi_{\mathrm{jj}}). \tag{A.4}$$

This is the generalized bond energy, representing the energy of formation of an $i-j$ bond in reference to half an $i-i$ bond and half a $j-j$ bond. The bond energies ϕ are supposed to be negative. N is the number of nearest atoms depending on the geometric environment of the atom.

The subscript "f" in equation A.3 indicates a fluid particle. When the "fluid" is a vapor phase, or does not exist, the bond between the a particle and a "fluid" particle, ϕ_{af}, is equal to zero. In this case, the $\varphi_{\mathrm{af}} = -\phi_{\mathrm{aa}}/2$ represents the excess energy of a dangling $a-a$ bond, with which the energy of a crystal surface composed with a atoms can be calculated.

With this rate-determining scheme, the A and B particles in an AB crystal, in this study, the Si and C atoms in the SiC crystal, behave differently because the difference in surface energies can be correctly reflected. This distinguishability is valid when considering a crystal in contact with a liquid phase ambiance and a vapor phase ambiance.

The bond energies ϕ_{ij} of solids are acquired from reported values and listed in table A.1, together with the source. However, the fluid-fluid bond energy and the solid-fluid bond energy remain unknown. Thus, we arbitrarily but reasonably decide the values of the fluid-fluid and the solid-fluid bond energies to mimic the effect of solvation. Thereby the effective bond energies are listed in table A.2.

Note that the values of bond energies are mainly divided into two groups, yet the relative orders are the same. Therefore we use average values in each group. The data

Table A.1 Bond energies in unit [eV].

Source	$\phi_{\mathrm{C-C}}$	$\phi_{\mathrm{Si-C}}$	$\phi_{\mathrm{Si-Si}}$
[5–7]	3.59	3.30	2.30
[8]	3.68	3.17	2.32
average	3.63	3.23	2.31
[9]	6.41	4.63	3.21
[10]	6.29	4.68	3.39
[11]	6.29	4.51	3.39
average	6.33	4.61	3.33

Table A.2 Effective bond energies in unit [eV].

Source	φ_{Cf}	φ_{SiC}	ϕ_{Sif}
Cohesive energy	1.850	-0.200	1.180
Dissociation energy	3.205	0.180	1.605

in references [5–8] are actually the cohesive energies per bond of the crystals while the rest[9–11] are the bond dissociation energy (D_0) of a A-B molecular. Moreover, as shown in the following portions of this study, the bond energy of aluminum (Al-Al) and Al-C shows a drastic difference in these two criteria. Considering the definition of the generalized bond energy, however, the data acquired from the cohesive energy should be used, yet we present the consequence of applying the two different bond energy choices briefly.

A.2 Results and discussion

A.2.1 Step terminations and shapes

Step edges can have different configurations due to different atoms attached to the edges, as shown in figure A.1. For example, on the C face, as shown in figure A.1 (a), the $\mathrm{S_D}$ and $\mathrm{S_N}$ steps can either terminate with a Si atom or a C atom. When a step terminates with a C atom, the C atom is overhung. Usually, people believe step edges are the ones terminating with no overhanging structure because such a structure generally represents lower energy.

The last section indicates that the Si and C atoms have distinct behaviors. Thus the steps terminated with different atoms will have different stabilities. Understanding the terminations at equilibrium helps us gain insight into the step behaviors. For

(a) steps on the C face

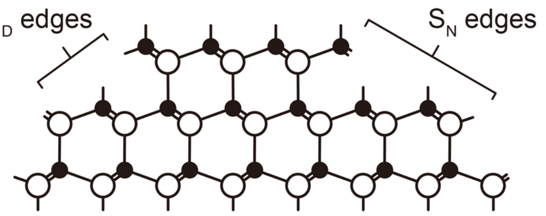

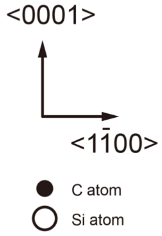

(b) steps on the Si face

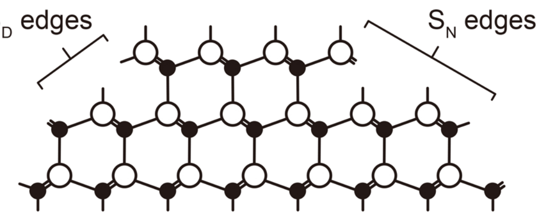

Figure A.1 Side view of S_N and S_D steps with different terminations, on the (a) C face and (b) Si face.

the C and Si atoms, with N nearest neighbors, their possible existing state, as well as the stability of steps terminated with them, are listed in table A.3. At equilibrium, the probability for an atom to be found is $P = R^+/R^-$ (not normalized). $P \leqslant 1$ stands for the atom can not stably exist. Moreover, we can define specific edge energy as $\varkappa = k_B T \ln(R^-/R^+)$ for the energy cost to create a segment of step terminating with the atom (with a length of the lattice constant). The C ($N = 1, 2$) and Si ($N = 1$) are such kinds of unstable atoms. They are the adatoms on the surface or step adatoms, as shown in 1.11. This instability initially excludes the configurations of the S_N step on the C face terminating with a C atom (figure A.1), and any step on the Si face terminating with a Si atom (figure A.1 (b)). The rest configurations are energetically allowed, yet we examinated this with the kMC simulation and found out the steps show a significant difference in their configurations on different polarity faces.

Figure A.2 shows equilibrated configurations of S_N and S_D steps, on the C face (figure A.2 (a, b)) and the Si face (figure A.2 (c, d)), respectively, at 3203 K, after $N_x N_y \times 10^5$ MC steps (1.89×10^{-7} sec.). The S_N steps, both on the C and Si faces, keep straight and terminate with the non-overhanging structure. That is because the S_N steps on the C face terminate with Si atoms ($N = 3$), while the S_N steps on the Si face terminate with C atoms ($N = 3$), both are the most stable configurations listed in table A.3. In contrast, the S_D steps on the C face become significantly rough by

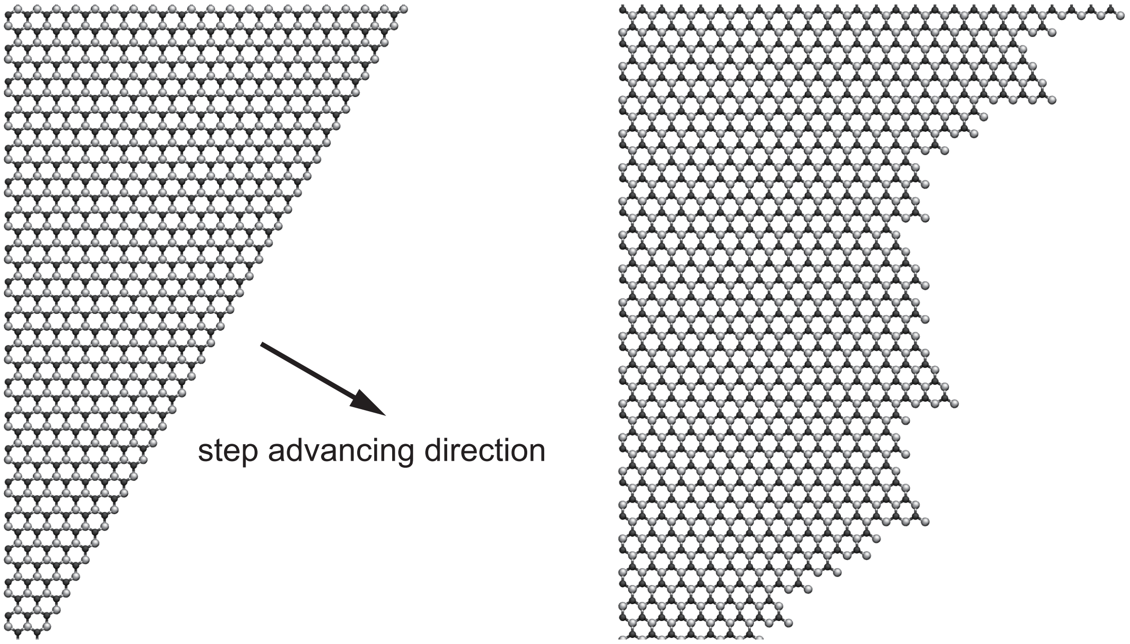

(a) C face, S_N step

(b) C face, S_D step

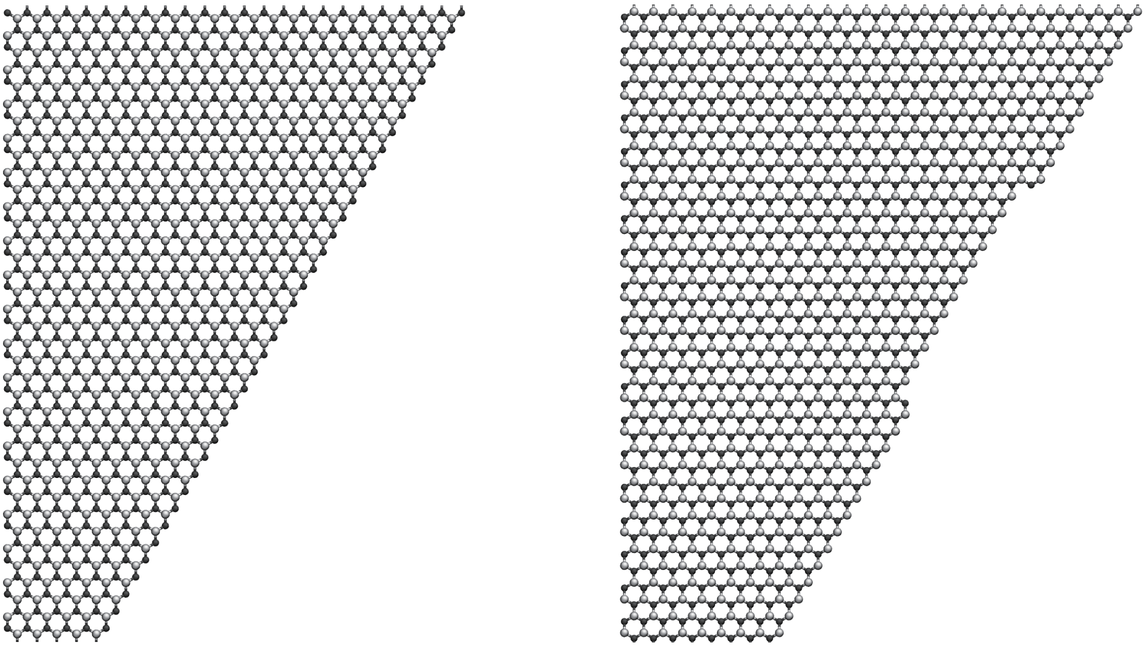

(c) Si face, S_N step

(d) Si face, S_D step

Figure A.2 Equilibrated configurations of the (a) S_N step and (b) S_D step on the C face, and (c) S_N step and (d) S_D step on the Si face. Si and C atoms are represented with white and black circles, respectively.

Table A.3 Possible existing states of atoms with different number of nearest neighbors, and the stability of steps terminating with the atoms.

	N	$\varkappa$ [eV]	existing state C face	 Si face	step stability C face	 Si face
C	1	4.57	adatom		unstable	
Si	1	1.89	adatom		unstable	
C	2	1.34	adatom		unstable	
Si	2	-1.34	S_D zig-zag protruding	S_D termination	stable	stable
C	3	-1.89	surface atom	S_N termination	–	stabler
Si	3	-4.57	S_N termination	surface atom	stablest	–

breaking into smooth atomic S_N segments, terminating with Si (N = 3). On the other hand, the S_D steps on the Si face are almost as straight as the S_N steps, yet with a few corners, known as kinks. The primary step segments terminate with Si (N = 2), while at the corners segments, the step-terminating atoms become C (N = 3).

The specific edge energy $\varkappa$ of the S_N step (-4.57 eV) is smaller than that of the S_D step (-1.34 eV), somewhat explaining the nature of a S_D to break into stabler S_N segments. On the other hand, the S_D step could also lower its specific edge energy by forming the S_N segments on the Si face. However, the ratio of such S_N segments is much smaller on the Si face compared with the C face. From the viewpoint of energy change, that can be explained by the close energy between the S_D step (-1.34 eV) and the S_N step (-1.89 eV), because forming alternating segments requires the creation of the “corners”, or kinks, and the density of kinks is decided by the work needed to create a kink, ω, which is determined by the specific edge energy. In the following section, we count the density of kinks on each step to study the step structures quantitatively.

A.2.2 Temperature dependence of kink density

The kink density of each step, both of the C face and the Si face are plotted against temperature in figure A.3. The kink density obtained with this Cherepanova’s scheme is quite different from the results obtained with Borovikov’s scheme, shown in figure 4.3. The S_N steps show little kink on both faces, even at a very high temperature like 3028 K. That implies a much larger kink creation work using Cherepanova’s scheme. Another significant difference is that the S_D steps on the C and Si faces behave differently now. When using Borovikov’s scheme, there is no difference between the two faces mentioned by the author and examined in

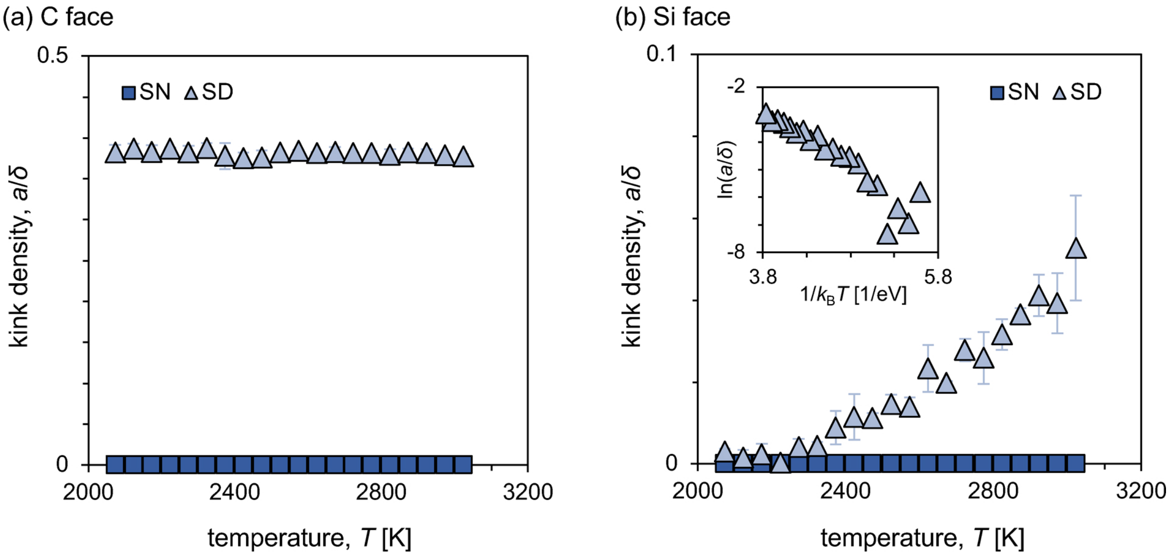

Figure A.3 Temperature dependence kink density of different steps on (a) the C face and (b) the Si face.

this work. While using the Cherepanova's scheme, as shown in figure A.3 (a), the S_D steps on the C face have a constant kink density of about 0.4, but on the Si face, kinks on the S_D steps are thermally activated (figure A.3 (b)).

According to [12], the average distance between two kinks for a step is

$$\delta = a[1 + \exp(\omega/k_B T)/2], \tag{A.5}$$

where a is the lattice constant and ω is the work cost when creating a kink on the step. From the inset in figure A.3 (b) one can figure out the kink creation work of S_D steps on the Si face, $\omega^{Si}_{S_D}$, being about 1.66 eV. The relatively large variance at low temperatures is because the surface used in the simulation is not large enough to eliminate the boundary effect. While for S_D steps on the C face one can reasonably conclude that $\omega^{C}_{S_D} = 0$ eV.

The difference between $\omega^{C}_{S_D}$ and $\omega^{Si}_{S_D}$ implies a different mechanism when creating a kink on the two steps. Figure A.4 shows schematics of kink creation processes. For comparison, the initial configurations without kink are also presented on the left side of each sub-figure. On the right side, configurations with two pairs of positive/negative kinks are illustrated, according to the results shown in figure A.2. The broken and newly created bonds to create kinks are colored red and blue, respectively, so the kink-creation works can be figured out by summing up the bond changes. When creating a kink on an S_D step on the C face, there is no change in the system energy. The steps spontaneously start wandering and become rough due to an entropic effect. While on the Si face, the kink creation energy is $\omega_{\mathrm{S_D}}^{\mathrm{Si}} = \varphi_{\mathrm{Cf}} + 1/2\varphi_{\mathrm{SiC}} - 1/2\varphi_{\mathrm{Sif}}$, which is supposed to be 1.16 eV according to the values list in table A.2.

(a) C face

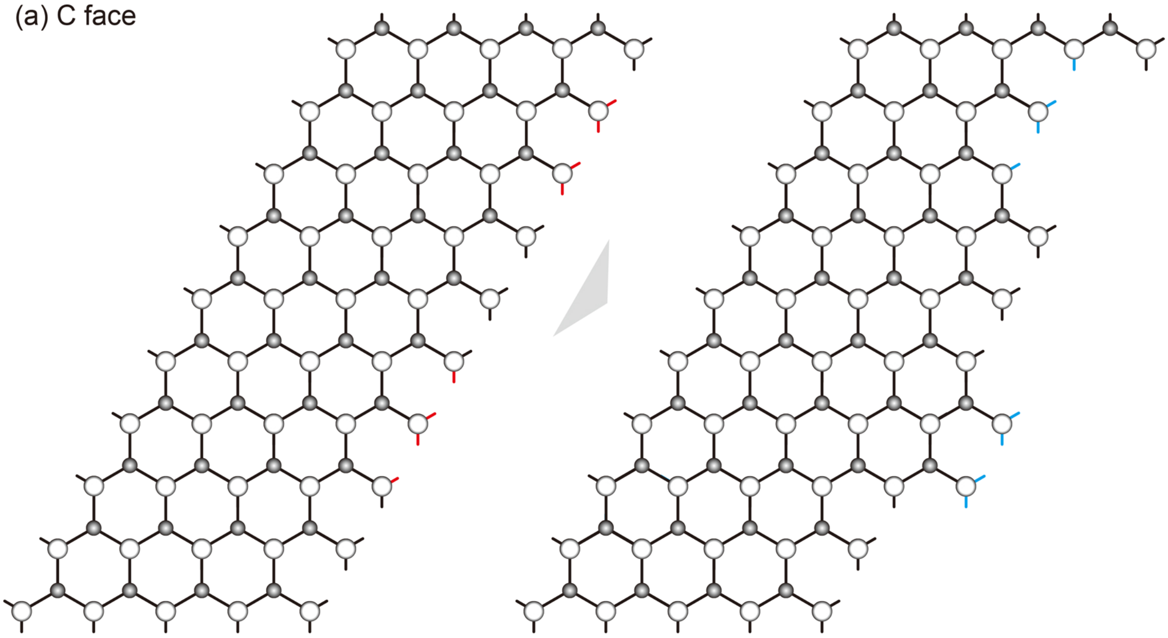

(b) Si face

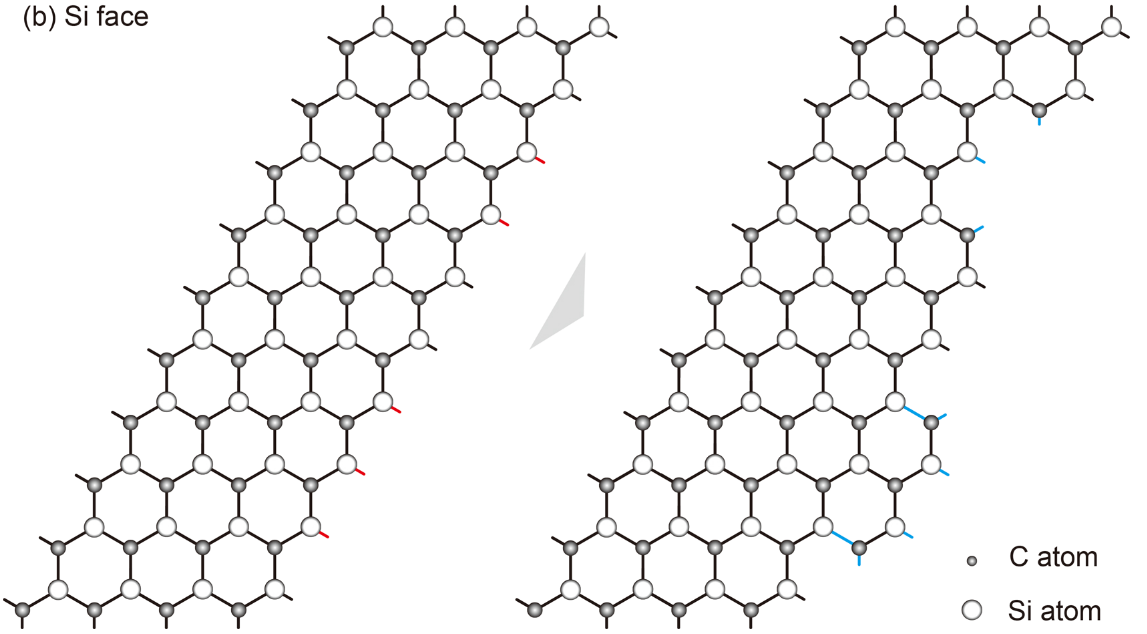

Figure A.4 Schematics of kink creation processes of an $\mathrm{S_D}$ step on the (a) C face and (b) Si face.

A.3 Conclusion

In this appendix, a rate-determining scheme involving effective bond strength is applied in the kinetic Monte Carlo model to reproduce the polarity of the SiC crystal. The step structures at the equilibrium of <1$\bar{1}$00> steps, both on the Si and C faces, are studied. The stability and the kink creation energy of different steps is discussed. Although the S_N steps on both faces appear smooth at even high temperatures on both polarity faces, the S_D steps on the two faces behaved differently. On the Si face, the S_D steps are relatively smooth with countable kinks on them, while on the C face, the S_D steps are extremely rough at any non-zero temperature due to a zero kink creation energy. The distinct stability of the steps is considered to lead to very different growth behaviors on the two polarity faces. When considering a system in contact with ambient phases like a solvent, the idea of effective bond strength would also help reflect the growth polarity. Further studies are looked forward to completely unravel the mystery around the diversity shown in the growth of SiC crystal.

References

[1] V. Borovikov and A. Zangwill, Physical Review B **79** (2009), 10.1103/PhysRevB.79.245413.

[2] E. Pearson, T. Takai, T. Halicioglu, and W. A. Tiller, Journal of Crystal Growth **70**, 33 (1984).

[3] T. Cherepanova, J. Van Der Eerden, and P. Bennema, Journal of Crystal Growth **44**, 537 (1978).

[4] J. Van der Eerden, P. Bennema, and T. Cherepanova, Progress in Crystal Growth and Characterization **1**, 219 (1978).

[5] T. L. Cottrell, *The Strengths of Chemical Bonds* (Butterworths Scientific Publications, 1958).

[6] B. d. Darwent, "Bond dissociation energies in simple molecules," Tech. Rep. NBS NSRDS 31 (National Bureau of Standards, Gaithersburg, MD, 1970).

[7] S. W. Benson, Journal of Chemical Education **42**, 502 (1965).

[8] O. Auciello, J. Birrell, J. A. Carlisle, J. E. Gerbi, X. Xiao, B. Peng, and H. D. Espinosa, Journal of Physics: Condensed Matter **16**, R539 (2004).

[9] Y.-R. Luo and J. A. Kerr, CRC handbook of chemistry and physics **89**, 89 (2012).

[10] R. David, *CRC Handbook of Chemistry and Physics 81st Edition: A Ready-Reference Book of Chemical and Physical Data* (CRC press, 2000).

[11] J. A. Dean, Material and manufacturing process **5**, 687 (1990).

[12] I. V. Markov, *Crystal Growth for Beginners: Fundamentals of Nucleation, Crystal Growth and Epitaxy*, 3rd ed. (World Scientific, New Jersey, 2016).

List of Publications

Journal Paper

1. Liu, X.; Dang, Y.; Suzuki, K.; Zhu, C.; Yu, W.; Harada, S.; Tagawa, M.; Ujihara, T. *Solvent Design Aiming at Solution Property Induced Surface Stability: A Case Study Using SiC Solution Growth*. Journal of Crystal Growth 2021, 126425.
2. Dang, Y.; Zhu, C.; Liu, X.; Yu, W.; Liu, X.; Huang, W.; Suzuki, K.; Harada, S.; Tagawa, M.; Ujihara, T. *Solution Growth of SiC Crystal with Enhanced Long-Term Composition Stability*. Journal of Crystal Growth 2021.
3. Dang, Y.; Zhu, C.; Ikumi, M.; Takaishi, M.; Yu, W.; Huang, W.; Liu, X.; Kutsukake, K.; Harada, S.; Tagawa, M.; Ujihara, T. *Adaptive Process Control for Crystal Growth Using Machine Learning for High-Speed Prediction: Application to SiC Solution Growth*. CrystEngComm 2021, 23 (9), 1982–1990.
4. Liu, X.; Zhu, C.; Harada, S.; Tagawa, M.; Ujihara, T. *Application of C-Face Dislocation Conversion to 2 Inch SiC Crystal Growth on an off-Axis Seed Crystal*. CrystEngComm 2019, 10.1039.C9CE01338E.
5. Murayama, K.; Harada, S.; Fujie, F.; Liu, X.; Murai, R.; Zhu, C.; Hanada, K.; Tagawa, M.; Ujihara, T. *Suppression of Polytype Transformation with Extremely Low-Dislocation-Density 4H-SiC Crystal in Two-Step Solution Method*. Materials Science Forum 2018, 924, 60–63.

Conference

1. Liu, X.; Dang, Y.; Harada, S.; Ujihara, T. *A Solvent Design Method for SiC Solution Growth Based on Solution Property Induced Surface Stability*; Vinci International Convention Centre, Tours, France, 2021.

2. Liu, X.; Dang, Y.; Harada, S.; Tagawa, M.; Ujihara, T. *CFD Simulation for Step Bunching Behavior*; Online, 2020.
3. Liu, X.; Zhu, C.; Harada, S.; Tagawa, M.; Ujihara, T. *Application of C Face Dislocation Conversion Technique to 2-Inch SiC Crystal Growth*; International Convention Centre, Birmingham, UK, 2018.
4. Liu, X.; Harada, S.; Murayama, K.; Murai, R.; Xiao, S.; Tagawa, M.; Ujihara, T. *Reduction of Threading Screw Dislocation during 4H-SiC Solution Growth on C Face*; Fukuoka Convention Center, 2017.